SIMULATION OF PROPPANT TRANSPORT IN HYDRAULIC AND NATURAL FRACTURES USING A COUPLED CFD-DEM METHOD

A Dissertation

by

RUI KOU

Submitted to the Office of Graduate and Professional Studies of
Texas A&M University
in partial fulfillment of the requirements for the degree of

DOCTOR OF PHILOSOPHY

Chair of Committee,	George Moridis
Co-Chair of Committee,	Thomas A. Blasingame
Committee Members,	Eduardo Gildin
	Vivek Sarin
Head of Department,	Jeff Spath

August 2020

Major Subject: Petroleum Engineering

ABSTRACT

Understanding proppant transport is critically important in designing effective stimulation systems for low-permeability reservoirs, as it leads to better estimates of the propped fracture dimensions and stimulated reservoir volume. Existing models mostly represent proppant as a continuous fluid phase. This assumption is valid for the conventional fracturing designs, where high viscosity fluid (*e.g.*, cross-linking gels) are used as the carrier fluid. Current fracturing designs mostly use low viscosity fluids (*e.g.*, slick water). As a result, proppants behave more like discrete particles and less like a continuous fluid phase.

Existing proppant transport models assume a single planar fracture as the main representation of the geometry of fractures, but the geometry of the subsurface fracture networks is much more complex. In this study I couple computational fluid dynamics with the discrete element method (CFD-DEM) to simulate proppant transport in a complex fracture network. The coupled simulator enables the explicit modeling of the motion of individual particles and offers a more accurate representation of the complex interactions between proppant particles, fracturing fluids, and fracture walls.

To calibrate the numerical model, I first conducted validation simulations that imitated a particle settling test, a particle collision test and a laboratory proppant transport experiment. Through scoping calculations, I determined the correct drag force model and matched the model predictions with existing analytical solutions and experimental data

for a wide range of flow regimes, including three different sizes of proppants (20-30 mesh, 30-40mesh and 50-70 mesh) in two types of fluids (water and oil).

In the main component of my study, I built multiple 3-dimentional fracture network models, which include one baseline vertical fracture model, three dipping fracture models, two hydraulic fracture-natural fracture (HF-NF) intersection models (T-shaped and Z-shaped) and, finally, a multi-cluster horizontal wellbore model. In the baseline vertical fracture model, the simulation results show that the flow regime of proppant (suspension or bedload transport) plays a critical role in determining the proppant advance and distribution in the fracture. Higher fluid velocities lead to a larger suspension transport region and a higher proppant placement efficiency in the hydraulic fractures.

In the dipping fracture models, my results show that decreasing the dipping angle increases the proppant placement efficiency. In the T-shaped HF-NF intersection model, I observed significantly better proppant placement in the NF when proppants are in the suspension transport regime. In the Z-shaped HF-NF intersection model, my study identified two parameters that are critical for estimating the occurrence of proppant bridging: the proppant concentration (C_p) and the ratio between the secondary fracture aperture and the proppant diameter (R_{fp}). At a fixed value of R_{fp}, continuous transport of proppant is possible when C_p is lower than a threshold value. Based on this determination, I use R_{fp} and C_p to propose a blocking criterion correlation.

Lastly, in my multi-cluster wellbore model, I experimented with various pumping strategies and computed the proppant and fluid distribution at each cluster. By comparing

the influence of injection rate, I discussed potential strategies to achieve a better (more even) proppant distribution at the different clusters.

ACKNOWLEDGEMENTS

I would like to thank my committee chair Dr. Moridis, co-chair Dr. Blasingame, and my committee members, Dr. Gildin and Dr. Sarin for their guidance and support throughout the course of this research.

I also thank my friends and colleagues and the department faculty and staff for making my time at Texas A&M University a great experience.

Finally, thanks to my mother and father for their encouragement and to my wife Bing and my daughter Emily for their patience and love.

CONTRIBUTORS AND FUNDING SOURCES

Contributors

This work was supervised by a dissertation committee consisting of Professor George Moridis (advisor), Thomas A. Blasingame (co-advisor), Eduardo Gildin of the Department of Petroleum Engineering, and Vivek Sarin of the Department of Computer Science and Engineering.

The dipping fracture models in Chapter 4 and the sharp-angled fracture model in Chapter 5 were suggested by Professor George Moridis. The analysis and plot of terminal velocity in Chapter 3 and the visualization of flow regime in Chapter 4 were suggested by Professor Thomas A. Blasingame.

The CFD-DEM code was compiled in part by Ping Luo of the Texas A&M High Performance Research Computing (HPRC) group. All of the numerical simulation was performed on the Ada cluster of HPRC at Texas A&M University

All other work conducted for the thesis (or) dissertation was completed by the student independently.

Funding Sources

This graduate study was supported by the Crisman Institute for Petroleum Research (CIPR) at Texas A&M University

NOMENCLATURE

C_d	dimensionless drag coefficient
C_p	Particle concentration, lbs. per gallon
d_p	particle diameter, m
e	coefficient of restitution
f_{ij}	contact force from particle j to particle i, N
G	shear modulus, Pa
k_n, k_t	elastic constant on normal, tangential direction, N/m
m_i	mass of particle i, kg
p	pressure, Pa
Re_i	particle Reynolds number for particle i, dimensionless
R_{fp}	ratio of fracture aperture to particle diameter, dimensionless
u_∞	terminal velocity, m/s
u_f	fluid velocity, m/s
u_i	velocity of particle i, m/s
V_{cell}	volume of CFD cell
w_{hf}	hydraulic fracture aperture, inch
w_{nf}	natural fracture aperture, inch
x_i	location of particle i, m

x_{hf}	hydraulic fracture half length, m
x_{nf}	natural fracture half length, m
Y	Young's modulus, Pa
δ_n, δ_t	overlap distance on normal, tangential direction, m
ε_f	volume fraction of fluid phase, dimensionless
ρ_p	particle density, kg/m^3
ρ_f	fluid density, kg/m^3
υ	Poisson ratio, dimensionless
ν_f	kinematic viscosity of fluid, m^2/s

TABLE OF CONTENTS

Page

LIST OF FIGURES

Page

LIST OF TABLES

Page

1. INTRODUCTION

In this section, I provide an overview of the research topic. This section is divided into three subsections. In the first subsection, I briefly introduce the hydraulic fracturing process and the challenges that researchers face in their effort to model the transport of proppants in hydraulic fractures. Then, I introduce the objective and focus of this research. Finally, I present a thorough literature review on the subject, covering a range of relevant issues, including the range of the associated flow regimes that have been defined in the course of studies on sediment transport and several recently-proposed proppant transport models that have been proposed in the petroleum engineering literature.

1.1. Statement of the Problem

Hydraulic fracturing with low viscosity fluids (*e.g.*, slick water) is one of the most common techniques used in the stimulation of unconventional (low- and ultra-low-permeability) reservoirs. Compared to stimulation methods using high viscosity fluids (such as cross-linked gels, the use of which is impractical in ultra-low permeability formations), slick water has the advantage of reducing the formation damage, promoting the connection of preexisting fractures (Beugelsdijk et al., 2000) and creating large stimulated reservoir volumes (Warpinski et al., 2005).

Although slick water fracturing has been proven as an effective stimulation method, the development of proppant transport models associated with slick water has been slow. This is because proppants are particles that have a tendency to settle and form immobile beds

in the thin (low viscosity) fracturing fluid. Additionally, proppant transport involves two distinctively different transport mechanisms: suspension transport (which, under certain conditions, approximates fluid transport) and bed load transport, a vastly different mechanism than that of the fluid transport. During the bed load transport regime, the majority of the particles settle into an immobile bed. Only a thin layer of particles on top of the bed can be transported by the fluid. This being the case, the assumption that proppants and the carrier fluid can be considered as one continuous phase becomes unsustainable and often leads to erroneous predictions.

Currently, while developing fracturing designs, completions engineers still lack a reliable tool to accurately predict the transport of proppants. Thus, the entire multi-billion-dollar stimulation industry is based on rather shaky scientific and engineering foundations, and is probably the main reason why the majority of hydraulic fractures are ineffective and unproductive (Wu and Olsen, 2016). This significant knowledge gap has substantial scientific, engineering and economic implications, and provided the motivation for this research that used a discrete model to realistically represent the proppant particles during the transport process.

1.2. Research Objectives

The main objectives of this work are:

- To develop a 3D model of fluid flow and proppant transport in a complex hydraulic fracture – natural fracture (HF-NF) network using a formulation based on coupling Computational Flow Dynamics (CFD) with the Discrete Element Method (DEM),

yielding an approach and a simulator that are free of the shortcomings and simplifications of the conventional approach of approximating proppants as a continuous phase.

- To investigate the combined effects and interactions of the dominant factors affecting the transport of a proppant slurry (*i.e.*, the proppant concentration, the fluid velocity and the flow regime) and the characteristics of the hydraulic fracture (fracture orientation and geometry) on the proppant placement efficiency.
- To develop scientific and engineering principles and criteria that will allow the optimization of the key parameters in the design of efficient proppant transport systems that have the potential to significantly enhance proppant placement and, consequently, maximize hydrocarbon production. The parameters I considered in this study are the number of clusters per stage, the surface pumping rate and the proppant concentration.

1.3. Review of Flow Regimes and Proppant Transport Models

The two main proppant transport mechanisms (suspension and bed load transport) have been the subject of many earlier studies investigating the transport of river sediments (Wasp et al., 1977; Pye, 1994). Suspension transport may occur in two possible scenarios: when a rapid influx of sediment enters a large body of fluid (Wasp et al., 1977), or when the fluid velocity reaches the minimum velocity required to re-suspend the settled bed (Brannon et al., 2006, Medlin et al., 1985). **Fig. 1.1 (a)** illustrates the suspension transport process and shows that particles and fluid form a mobile slurry. The fluid drag force and

the gravitational force dominate the motion of particles (Chanson, 2004), thus energy dissipation due to inter-particle collision is minimal.

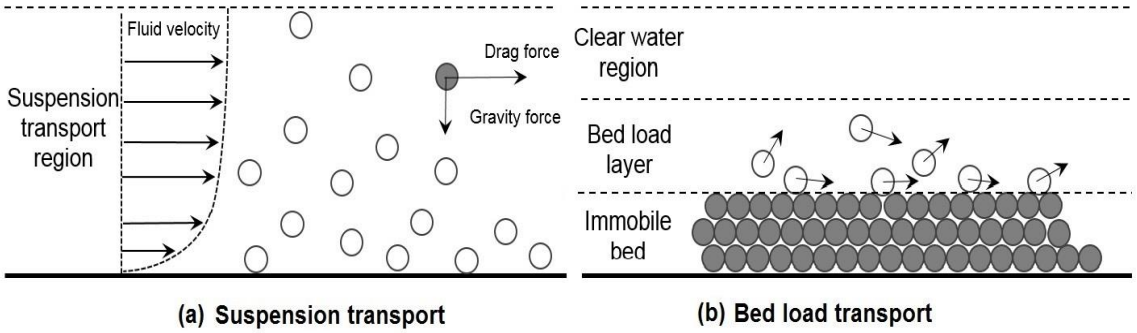

Figure 1.1 Illustration of possible proppant transport mechanisms in low viscosity fluid (slick water)

Bed load transport occurs when the fluid velocity is lower than the minimum velocity required for suspension transport (McClure. 2018). In this case, drag and lift forces exerted by the fluid mobilize only the top layers of the settled bed. This results in particle rolling and saltation along the surface of the underlying proppant bed (Schmeeckle et al., 2003). **Fig. 1.1 (b)** illustrates the bed load transport process. Here the kinetic energy of the top boundary layer of the fluid (*i.e.*, the one in contact with the upper part of the bed) is dissipated by inter-particle friction and contact forces. Thus, bed load transport is limited in both efficiency and capacity (in terms of the amount of the transported material) compared to suspension transport.

Recent developments in proppant transport models have attempted to incorporate at least one of these two mechanisms. Weng et al. (2011) implemented a three-layer bed load

transport model. It consists of a proppant bank layer, a slurry layer and a clear fluid layer. Shiozawa et al. (2016) proposed a two-region model, combining a slurry (suspension) region and an immobile bed region. Both implementations have been formulated in the Eulerian-Eulerian two-fluid method (TFM), which treats both the solid particles and the fluid as continua. The main advantage of the TFM is that it can be easily implemented into a field-scale simulator. However, it suffers from the inability to fully capture the discrete character of the proppant particles. Velikanov et al. (2018) improved the TFM by adding a blocking (bridging) function suggested by Dontsov et al. (2014). The blocking function disables the proppant motion (by setting particle phase velocity to zero) when the particle concentration exceeds the maximum allowable concentration. Compared to the earlier TFMs, Velikanov's model corrected the motion of the particle pseudo-phase, thus providing better representation of the motion of solid particles in the thin fluids of slick water.

In this study, I combine the principles of Computational Fluid Dynamics (CFD) with the Discrete Element Method (DEM, a numerical technique formulated in the Lagrangian frame) to model the fluid-particle system. In the coupled CFD-DEM simulator, the fluid phase is modeled as a continuous phase using a classical CFD approach. The incompressible Navier-Stokes equation is first discretized using a finite volume method to solve for the locally averaged pressure and velocity at each computational cell. Particles in the system are modeled/represented as a discrete phase using the DEM, which predicts the behavior of the solid phase by modeling and tracking the behavior and motion of individual particles. DEM takes into account the particle-particle and the particle-

boundary interactions. Compared to the standard Eulerian methods (*e.g.*, TFM), DEM does not require the solid phase to be continuous, an attribute that makes it a powerful tool in modeling slick water-based proppant transport. The fluid phase and the solid phase are coupled by the drag force.

To fully represent the physics of particle transport, I further coupled the CFD-DEM model with the Unresolved Surface Model (USM) that computes the fluid-particle forces for all particles within the same CFD cell. This method allows the size of the CFD cell to be much larger than the size of the simulated particles. Of the several available (but still unresolved) drag force correlations that have been proposed (Schiller et al., 1935; Di Felice, 1994; Kafui et al., 2002), I used the Di Felice (1994) model because it is valid for both dense and dilute particle flow (Norouzi, et al., 2016).

My earlier work (Kou et al. 2018a, 2018b, 2019) showed that the coupled CFD-DEM simulation is capable of capturing various behaviors of proppant in slick water-- including dunning (proppant settling into immobile dunes), bridging (proppant blocking at the narrow spots of fracture), and wash out (settled proppant re-mobilized by fluid)-- without the need to resort to any empirical approximations. Despite its theoretical and conceptual advantages, the Lagrangian underpinnings of the DEM make it inherently more computationally demanding than Eulerian methods (Sun et al., 2016, 2017). A DEM simulation of a laboratory-scale experiment often requires tracking millions of Lagrangian particles (Mao et al., 2019, Sun et al., 2018a, 2018b), and a field-scale problem (*i.e.* proppant transport in fracture networks) may require billions of particles. To tackle the large-scale problems, coarse graining (CG) techniques have been gaining the attention of

DEM researchers (Lu et al., 2017, Weinhart et al., 2016). This technique involves using enlarged (or upscaled) particles to represent a group of original particles. As a result, the number of particles required for large-scale problems can be reduced significantly. By using correct scale factors, forces acting on the CG particles are proportional to the forces acting on the original particle. Thus, the velocity and trajectory of CG particles are assured to be the same as in the original problem. In this study, I follow the analysis suggested by Chu et al., (2016) to determine these scale factors.

2. CFD-DEM MODEL FORMULATION

In this section, I describe the formulation of the coupled CFD-DEM method. This section is divided into two subsections. The first subsection introduces the momentum conservation equation of the solid particles and provides a detailed description of the contact forces in the normal and tangential directions. The second subsection introduces the mass and momentum conservation equations for the fluid phase and describes the Di Felice model — quantifying the drag force — that couples the solid and the fluid phase. Lastly, the Di Felice drag force model is compared to experimental data and the Stokes analytical solution.

2.1. Governing Equations of the Solid Particles

I use the Discrete Element Method (DEM) to model the motion of proppant particles. The approach in DEM involves tracking proppant particles in a Lagrangian frame and, consequently, the mass conservation equation of the proppant phase need not be solved. **Eq. 2.1** describes the momentum conservation equation for the Lagrangian particles as

$$\boldsymbol{m_i}\frac{d\vec{v}_i}{dt} = \boldsymbol{m_i}\vec{g} + \sum_{j\in CL_i}\vec{f}^{c}_{ji} + \vec{f}^{f-p}_{i} \quad \text{.....(2.1)}$$

where $\boldsymbol{m_i}$ is the mass of particle **i** (kg); $\vec{v}_i$ is the velocity of particle **i** (m/s); $\vec{f}^{c}_{ji}$ is the force from particle **j** to particle **i** (N/m); $\vec{g}$ is the gravitational constant (m/s^2); and $\vec{f}^{f-p}_{i}$ is the fluid particle force (N). $\boldsymbol{CL_i}$ is the list of particles that surrounds particle **i**.

Three types of forces are considered in order to calculate the motion of a proppant particle. These are (a) the body force ($\boldsymbol{m_i\vec{g}}$), (b) the particle-particle contact force ($\vec{\boldsymbol{f}}_{\boldsymbol{ji}}^{\boldsymbol{c}}$), and (c) the fluid-particle force ($\vec{\boldsymbol{f}}_{\boldsymbol{i}}^{\boldsymbol{f-p}}$). I use the Hertz-Mindlin-Deresiewicz (H-MD) model to describe the particle-particle contact force model (Hertz, 1882; Mindlin and Deresiewicz, 1953). This is represented by the following equation:

$$\vec{\boldsymbol{f}}_{\boldsymbol{ji}}^{\boldsymbol{c}} = \vec{\boldsymbol{f}}_{\boldsymbol{ji}}^{\boldsymbol{n}} + \vec{\boldsymbol{f}}_{\boldsymbol{ji}}^{\boldsymbol{t}} = \left(\boldsymbol{k_n\delta_n\vec{n}_{ij} - \gamma_n v_{rn}\vec{n}_{ij}}\right) + \left(\boldsymbol{k_t\delta_t\vec{t}_{ij} - \gamma_t v_{rt}\vec{t}_{ij}}\right) \quad \text{..... (2.2)}$$

where $\vec{\boldsymbol{f}}_{\boldsymbol{ji}}^{\boldsymbol{c}}$ is the total contact force (N); $\vec{\boldsymbol{f}}_{\boldsymbol{ji}}^{\boldsymbol{n}}$ is the contact force applied in the normal direction (N); $\vec{\boldsymbol{f}}_{\boldsymbol{ji}}^{\boldsymbol{t}}$ is the contact force applied tangentially (N); $\boldsymbol{k_n}$, $\boldsymbol{k_t}$ are the elastic coefficients on the normal and the tangential directions, respectively (N/m); $\boldsymbol{\delta_n}$, $\boldsymbol{\delta_t}$ are the overlap distances in the normal and the tangential directions, respectively (m); $\boldsymbol{\gamma_n}$, $\boldsymbol{\gamma_t}$ are the viscoelastic damping coefficients in the normal and the tangential directions, respectively (N·s/m); and $\boldsymbol{v_{rn}}$, $\boldsymbol{v_{rt}}$ are the relative velocities in the normal and the tangential directions, respectively (m/s).

The H-MD contact force model is a nonlinear viscoelastic-type model, in which the elastic terms ($\boldsymbol{k_n}$, $\boldsymbol{k_t}$) conserve the kinetic energy, and the viscous terms ($\boldsymbol{\gamma_n}$,$\boldsymbol{\gamma_t}$) control the amount of energy dissipation. In the normal direction, the coefficient of restitution ($\boldsymbol{e}$, dimensionless parameter) determines the amount of energy loss after each collision. The term $\boldsymbol{\gamma_n}$ is estimated from **Eq. 2.3** to **2.5** as follows:

$$\boldsymbol{\gamma_n} = -2\sqrt{\frac{5}{6}}\frac{\boldsymbol{ln(e)}}{\sqrt{\boldsymbol{ln^2(e)+\pi^2}}}\sqrt{\boldsymbol{S_n}\left(\frac{1}{\boldsymbol{m_1}}+\frac{1}{\boldsymbol{m_2}}\right)} \quad \text{..... (2.3)}$$

$$S_n = 2Y^* \sqrt{\left(\frac{1}{R_1} + \frac{1}{R_2}\right)\delta_n} \quad \text{..... (2.4)}$$

$$Y^* = \left(\frac{1-{v_1}^2}{Y_1} + \frac{1-{v_2}^2}{Y_2}\right) \quad \text{..... (2.5)}$$

where Y_1, Y_2 are the Young's moduli of elasticity of granular materials 1 and 2, respectively; (Pa); v_1, v_2 are the associated Poisson ratios (dimensionless); m_1, m_2 are the masses of the two colliding particles (kg); and δ_n is the normal overlap distance (m). In the tangential direction, the dimensionless friction coefficient (μ) also controls the amount of the energy dissipation by limiting the total tangential force ($\vec{f}_{ij}^{t}$), which is defined as

$$\vec{f}_{ij}^{t} = -k_t \delta_t \vec{t}_{ij} - \gamma_t v_{rt} \vec{t}_{ij} \quad \text{..... (2.6)}$$

Eq. 2.6 is valid when the total tangential force is smaller than the Coulomb's criterion, which is defined as follows:

$$\left\|\vec{f}_{ij}^{t}\right\| \leq \mu \left\|\vec{f}_{ij}^{n}\right\| \quad \text{..... (2.7)}$$

When the tangential force reaches the Coulomb criterion, a particle will slide in the tangential direction. Thus, the tangential overlap distance should be truncated to the following value:

$$\delta_t = \frac{1}{k_t}\left(\mu \left\|\vec{f}_{ij}^{n}\right\| + \gamma_n v_{rn}\right) \quad \text{..... (2.8)}$$

Both e and μ are dimensionless parameters, with values ranging from 0 to 1. There are limited measured values of e and μ for sand and proppant particles in the literature.

Additionally, the few laboratory measurements that are available show that both parameters are subject to large variations. Reagle et. al. (2012) measured the coefficient of restitution for Arizona Road Dust (sand) and reported that $\boldsymbol{e}$ could range from 0.2 to 0.6, with a mean value of 0.4. USACE (1992) reported that the friction coefficient between a concrete surface and various soil particles (ranging from silty clay to coarse gravel) ranged from 0.30 to 0.70. A common practice in DEM simulations is to determine $\boldsymbol{e}$ and $\boldsymbol{\mu}$ by matching laboratory-scale experiments to their numerical representations. In this study, I followed the same approach: I obtained the values of $\boldsymbol{e = 0.4}$ and $\boldsymbol{\mu = 0.5}$ by matching earlier laboratory bed load transport experiments (Patankar et al., 2002) to the predictions of my numerical simulator, and used these values in all my field-scale simulations.

2.2. Governing Equations of the Fluid Phase

2.2.1. Formulation of Mass and Momentum Conservation

As discussed earlier, I used the CFD method to simulate the motion of the fluid phase. The mass conservation and momentum conservation equations for the fluid phase are described in **Eq. 2.9-2.10** as

$$\frac{\partial(\rho\varepsilon_f)}{\partial t} + \nabla \cdot \left(\rho\overrightarrow{u_f}\right) = 0 \quad \text{..... (2.9)}$$

$$\rho\frac{\partial(\varepsilon_f\overrightarrow{u_f})}{\partial t} + \rho[\overrightarrow{u_f} \cdot \nabla\left(\varepsilon_f\overrightarrow{u_f}\right)] = \nabla \cdot \overleftrightarrow{\sigma} - \frac{1}{V_{cell}}\sum_{i=1}^{kv}\vec{f}_i^{f-p} + \rho\varepsilon_f\vec{g} \quad \text{..... (2.10)}$$

where $\boldsymbol{\rho}$ is the fluid density (kg/m3); $\boldsymbol{\varepsilon_f}$ is the volume fraction of fluid; $\overrightarrow{\mathbf{u_f}}$ is the fluid velocity (m/s); $\boldsymbol{\mu_f}$ is the fluid viscosity (Pa.s); $\vec{f}_i^{f-p}$ is the fluid-to-particle force for particle

i (N); $\boldsymbol{kv}$ is the number of particles in the corresponding fluid cell; and $\boldsymbol{V_{cell}}$ is the volume of the fluid cell (m^3).

The fluid-to-particle force ($\vec{\boldsymbol{f}}_{\boldsymbol{i}}^{\boldsymbol{f-p}}$) is the term that couples the particle phase and the fluid phase. It contains the pressure gradient force, the fluid drag force and the fluid shear force. Instead of computing each of the individual component forces listed above, one can use the "Model A" formulation to reduce the coupling term ($\vec{\boldsymbol{f}}_{\boldsymbol{i}}^{\boldsymbol{f-p}}$) to the fluid drag force ($\vec{\boldsymbol{f}}_{\boldsymbol{i}}^{\boldsymbol{d}}$).

A detailed derivation of the Model A formulation in a 3-dimensional rectangular Cartesian coordinate system is available in the earlier work of Kou et al. (2018b), and is also provided in **Appendix A**. The final form of the momentum balance equation in the x-direction (taken as the main direction of flow in the HF) is shown in **Eq. 2.11**. The formulation for the *y* and *z* directions can be obtained by simply replacing the primary variable index (u_x) by y and *z* as new primary variable, *i.e.*,

$$\frac{\boldsymbol{\partial}\left(\boldsymbol{\varepsilon_f u_x}\right)}{\boldsymbol{\partial t}}+\frac{\boldsymbol{\partial \varepsilon_f u_x u_x}}{\boldsymbol{\partial x}}+\frac{\boldsymbol{\partial \varepsilon_f u_x u_y}}{\boldsymbol{\partial y}}+\frac{\boldsymbol{\partial \varepsilon_f u_x u_z}}{\boldsymbol{\partial z}}=$$

$$-\frac{\boldsymbol{1}}{\boldsymbol{\rho}}\frac{\boldsymbol{\partial p}}{\boldsymbol{\partial x}}+\frac{\boldsymbol{1}}{\boldsymbol{\rho}}\left(\frac{\boldsymbol{\partial \varepsilon_f \tau_{xx}}}{\boldsymbol{\partial x}}+\frac{\boldsymbol{\partial \varepsilon_f \tau_{xy}}}{\boldsymbol{\partial y}}+\frac{\boldsymbol{\partial \varepsilon_f \tau_{xz}}}{\boldsymbol{\partial z}}\right)-\frac{\boldsymbol{1}}{\boldsymbol{V_{cell}}}\sum_{\boldsymbol{i=1}}^{\boldsymbol{kv}}([\vec{\boldsymbol{f}}_{\boldsymbol{i}}^{\boldsymbol{d}}]_{\boldsymbol{x}})+\boldsymbol{\varepsilon_f g_x} \quad \ldots. (2.11)$$

Eq. 2.11 is the governing equation of momentum balance of the fluid phase. It is a modified version of the Navier-Stokes equation for incompressible fluids. The modification is represented by the summation term on the right-hand side of **Eq. 2.11**. The drag force acting on particle *i* is calculated during the DEM simulation, and then passed to the CFD simulation. For each CFD cell, the computational process involves first the summation of the drag forces acting on the particles within the CFD cell, and then

averaging the force using the cell volume ($\boldsymbol{V_{cell}}$). The average drag force is then subtracted from the right-hand side of the momentum balance equation.

2.2.2. Formulation of the Coupling Force Term

As shown in **Eq. 2.1** and **Eq. 2.11**, the fluid-to-particle drag force is the term that couples the CFD and the DEM components of the simulation process. To calculate the fluid-particle drag force ($\vec{f}_i^d$) in **Eq. 2.11**, I use the Di Felice model (Di Felice, 1994), described by the following **Eq. 2.12-2.15**:

$$\vec{f}_i^d = 3\pi\mu_f d_p \hat{f}_i^d (\overrightarrow{u_f} - \overrightarrow{v_i}) \quad \text{.....(2.12)}$$

$$\hat{f}_i^d = \frac{C_d}{24} Re_i \varepsilon_f^{-\chi} \quad \text{.....(2.13)}$$

$$\chi = 3.7 - 0.65 e^{(-0.5*(1.5-log_{10}Re_i)^2)} \quad \text{.....(2.14)}$$

$$C_d = (0.63 + 4.8 Re_i^{-0.5})^2 \quad \text{.....(2.15)}$$

where, $Re_i$is the particle Reynolds number; $\overrightarrow{v_i}$ is the velocity of particle **i** (m/s); d_p is the particle diameter (m); ε_f is the volume fraction of the fluid; u_f is the fluid velocity (m/s); $\overrightarrow{u_f}$ is the fluid velocity (m/s); and C_d is the dimensionless drag coefficient.

Fig. 2.1 shows the performance of the Di Felice (1994) drag force model by demonstrating the relationship between its associated dimensionless drag coefficient and the particle Reynolds number, vis-à-vis the drag coefficient obtained from experimental data summarized by Duan et al. (2015).

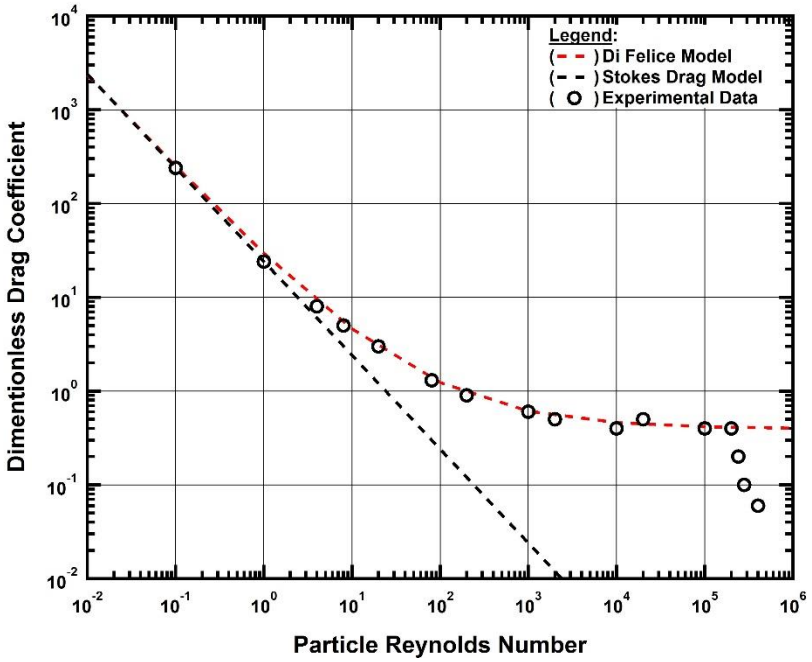

Figure 2.1 Di Felice model vs Stokes drag model vs experimental data (reprinted from Duan et al. 2015) on dimensionless drag coefficient

As is evident from this figure, the Di Felice model matches the experimental data over a wide range of Reynolds numbers. For comparison, I also plotted the drag coefficient estimated from the Stokes law (King et al., 2002), which is commonly used for predicting the settling velocity of particles. The deviations of the predictions of the Stokes law from the experimental data are significant and increase as the particle Reynolds number rises above 1.0. Another advantage of the Di Felice model is that it takes local particle concentration into consideration by including the voidage function term $\varepsilon_f^{-\chi}$, where ε_f is the volume fraction of the fluid (dimensionless), and χ is an empirical dimensionless correction factor estimated from experimental data (Di Felice, 1994).

3. PARTICLE SCALE AND LABORATORY SCALE VALIDATION

In this section I discuss the CFD-DEM simulations I conducted in order to duplicate numerically (to the extent possible) the laboratory experiments. This section is divided into three subsections. In the first subsection, I use a collision duration test to validate our contact force model. In the second subsection, I use a terminal velocity experiment to validate the drag force model in my coupled simulator. Lastly, in the 3rd subsection I compare my numerical simulation predictions to two proppant transport experiments on a laboratory scale.

To perform the coupled simulation, I use LIGGGHTS (Kloss et al., 2012) as the solid phase solver. This is an open-source DEM software based on the granular packages of LAMMPS (Plimpton, 1995). LAMMPS is a classical molecular dynamics code developed by Sandia National Laboratories. I used OpenFOAM as the fluid phase CFD solver. The CFD model of fluid flow uses the Pressure-Implicit with Splitting of Operators (PISO) solver, which is included in the OpenFOAM standard solver libraries (Weller et al., 1998).

The coupling of the solid and the fluid phases is achieved by the open-source software CFDEMcoupling (Goniva et al., 2012). CFDEMcoupling provides a modified solver based on OpenFOAM standard solver library. The modified solver calls the LIGGHTS solver in between CFD simulation timesteps, to achieve the couple simulation. The time step sizes for the CFD and the DEM simulations are 0.001 s and 0.1 s respectively, which yields a coupling ratio of 100:1. The mesh size of the CFD domain is tested by increasing progressively the number of the CFD cells in a trial-and-error manner. Details of mesh independency is available in Section 3.2. Furthermore, a clear description of each of the

simulators, their capabilities, how they are coupled, and what are the computer facilities used is available in Section 4.

3.1. Collision Duration Test

As shown in the Section 2, modeling the motion of the proppant particles involves description of two fundamental forces: the particle-particle contact force and the fluid-particle drag force. To verify and validate the contact force model that I used in this study, I performed contact duration simulations that attempted to numerically duplicate the experimental results of Stevens et al. (2005). In these experiments, two stainless steel spheres collide at various impact velocities. The properties of the materials in my DEM simulation were as reported in the Stevens et al. (2005) study (see **Table3.1**). In **Fig. 3.1** I compared the DEM predicted contact duration and experimental results.

Table 3.1 Properties of stainless-steel spheres from Stevens et al. (2005)

Parameters	SI Unit
Radium, $\boldsymbol{R}$	0.0127 m
Density, $\boldsymbol{\rho}$	8030 kg/m^3
Young's modulus, $\boldsymbol{Y}$	1.93×10^{11} N/m^2
Poisson ratio, $\boldsymbol{\upsilon}$	0.35
Coefficient of restitution, $\boldsymbol{e}$	0.879
Impact velocity, **v**	0.2-1.5 m/s

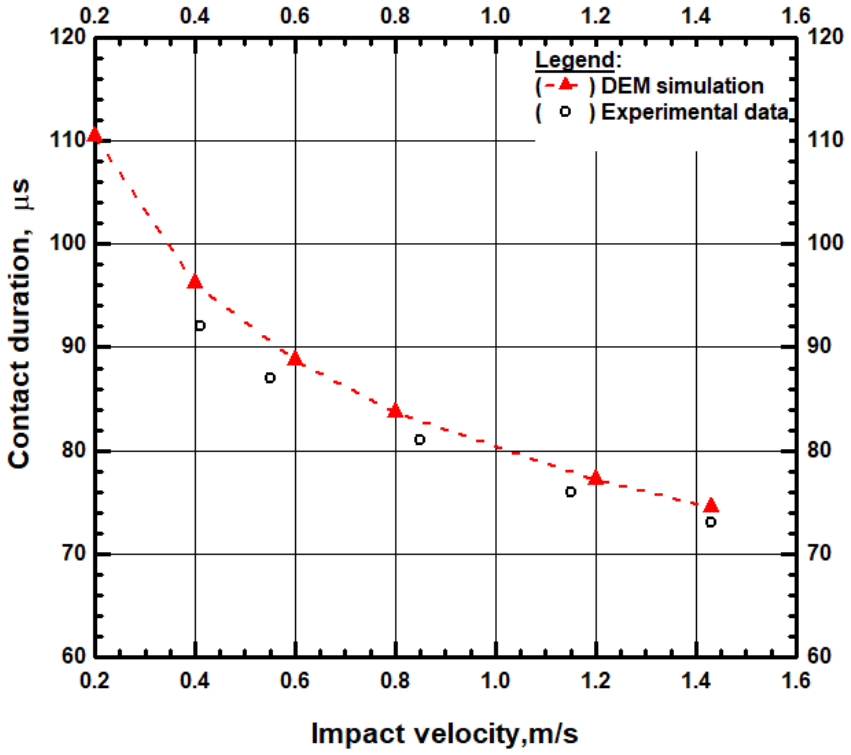

Figure 3.1 Contact duration DEM simulation vs experimental measurement (reprinted from Stevens et al., 2005)

The experimental results and the DEM numerical predictions in **Fig. 3.1** show that the collision duration decreases as the impact velocity increases and are in excellent agreement, thus providing evidence in support of the validity of the DEM component of my coupled simulator.

3.2. Terminal Velocity Test

3.2.1. Proppant Settling Experiment and Simulation

To verify the drag force model that couples the particles and the fluid phases, I performed a coupled CFD-DEM simulation that described numerically a laboratory test of settling proppant particles that I conducted within the framework of this study. **Fig. 3.2** shows the laboratory set-up that I used to measure the terminal velocity of the proppant particles.

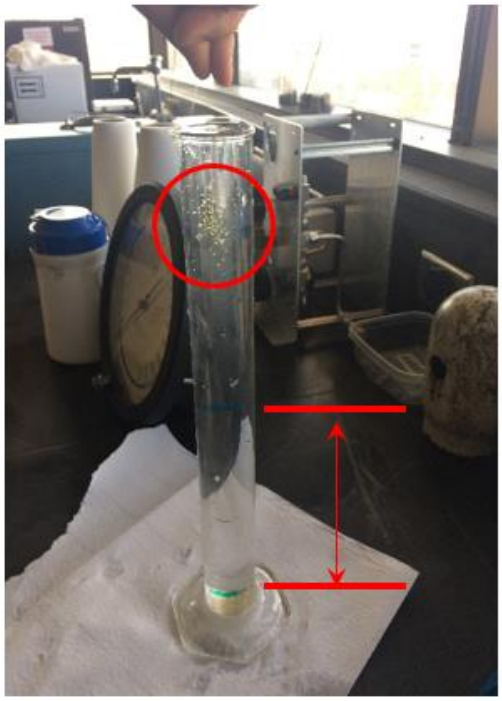

Figure 3.2 Laboratory measurement of terminal velocity

To collect experimental data over a wide range of flow regimes, I measured the terminal velocity of three proppant with different particle sizes of (20-30 mesh, 30-40mesh and 50-70 mesh) in two types of fluids (water and oil). I studied six differences cases (**Table 3.2**) of particle terminal velocity: Case 1 involved 50-70 mesh sand settling in water through

0.4m distance. Case 2 involved 50-70 mesh sand settling in water through 0.15m distance. Case 3 involved 20-30 mesh sand settling in water through 0.4m distance. Case 4 involved 20-30 mesh sand settling in water through 0.15m distance. Case 5 involved 30-40 mesh sand settling in water through 0.7m distance. Case 6 involved 30-40 mesh sand settling in water through 0.4m distance. To ensure that proppant particles reached indeed terminal velocity, I measured the terminal velocity at two different locations along the length of the settling tube. The detailed data collected from the experiments are shown in **Table 3.2.**

Table 3.2 Terminal velocity measurements for combinations of proppant sizes and fluid viscosity

Case	Viscosity cp	Distance m	Time (1) s	Time (2) s	Time (3) s	Average Time, s	Terminal Velocity, m/s
1	1.0	0.4	11.01	10.18	10.66	10.62	0.0377
2	1.0	0.15	4.34	4.74	4.68	4.59	0.0327
3	1.0	0.4	4.21	4.28	4.03	4.17	0.0958
4	1.0	0.15	1.61	1.54	1.58	1.58	0.0951
5	20.0	0.7	77.32	79.1	102.28	86.23	0.0081
6	20.0	0.4	39.7	33.65	36.55	36.63	0.0109

I then conducted CFD-DEM simulations to numerically duplicate the process of estimating the terminal velocity. **Fig. 3.3** shows the simulation domain I created for the numerical settling test. The height, length and width of the simulation domain were 0.25m, 0.1m and 0.1m, respectively. The CFD mesh size is 0.025x 0.025x0.025 m. The DEM

particle size is 0.512 mm. The proppant particle accelerates from its initial zero velocity at the point of release in the fluid to reach the final terminal velocity.

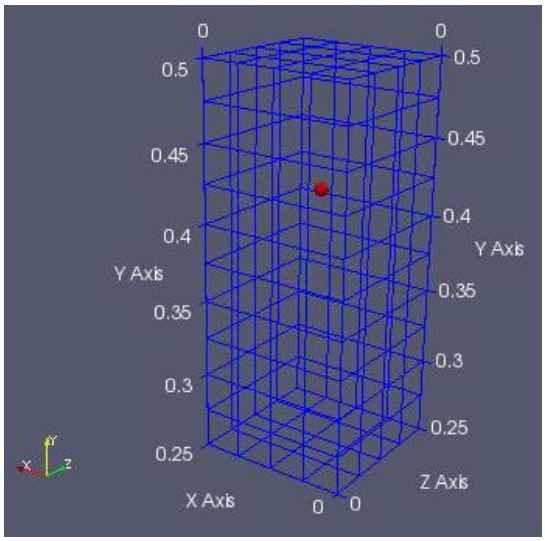

Figure 3.3 CFD-DEM simulation of proppant settling test with particle size = 0. 512 mm, mesh size = 0.025m

To ensure that the size of the element of simulation mesh used in this study does not influence the settling simulation, I tested 3 different CFD mesh element sizes (see **Fig. 3.4**), ranging from 0.025m to 0.005m. I simulated the terminal velocity of particle (size = 0.531mm) in each of the simulation domains in **Fig. 3.4** and recorded the terminal velocity. **Table 3.3** shows the particle size, the simulation element size on y direction (the direction of particle settling) in the mesh elements, and the terminal velocity measure from settling sensitivity test.

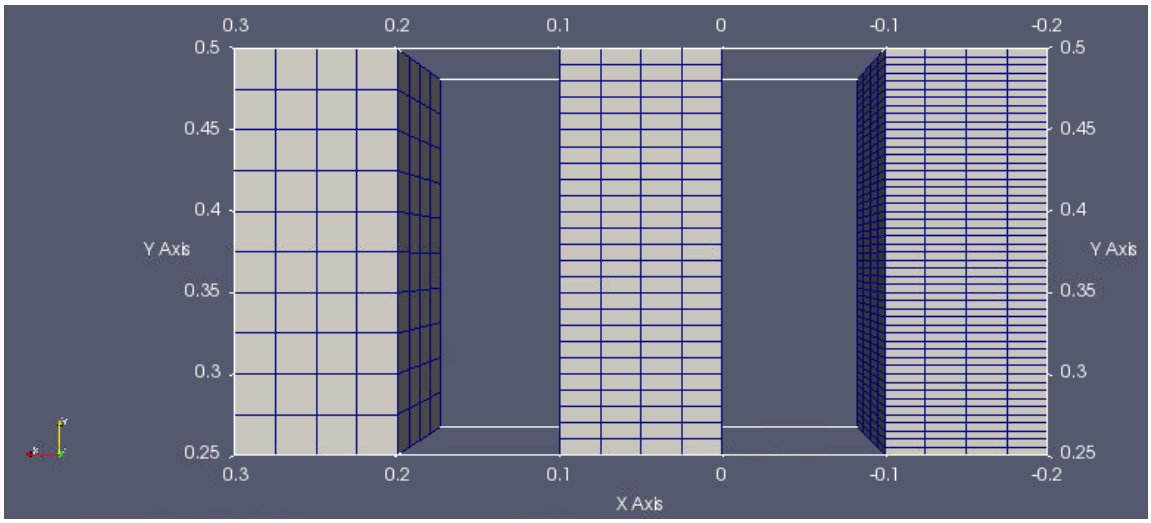

Figure 3.4 Mesh sensitivity test for settling test, with Y direction (the settling direction) mesh of 0.025m (left), 0.010m (middle) and 0.005m (right)

Table 3.3 Terminal velocity sensitivity to mesh size

Case	Simulation Element Size on y Direction	Particle Size, mm	Fluid Viscosity, cp	Terminal Velocity, m/s
1	0.025	0.512	1.0	0.03758
2	0.010	0.512	1.0	0.03758
3	0.005	0.512	1.0	0.03758

Table 3.3 shows that the terminal velocity does not change when the Dy (the simulation element size on y direction) of the mesh elements is refined from 0.025 m to 0.005 m. Thus, I decided to use the mesh size of 0.025m for the following terminal velocity tests. **Fig. 3.5** shows the terminal velocities estimated from the CFD-DEM simulations, as well as those measured in the laboratory experiment. For comparison purposes, we also

included an estimate of the terminal velocity calculated from the Stokes law (King et al., 2002).

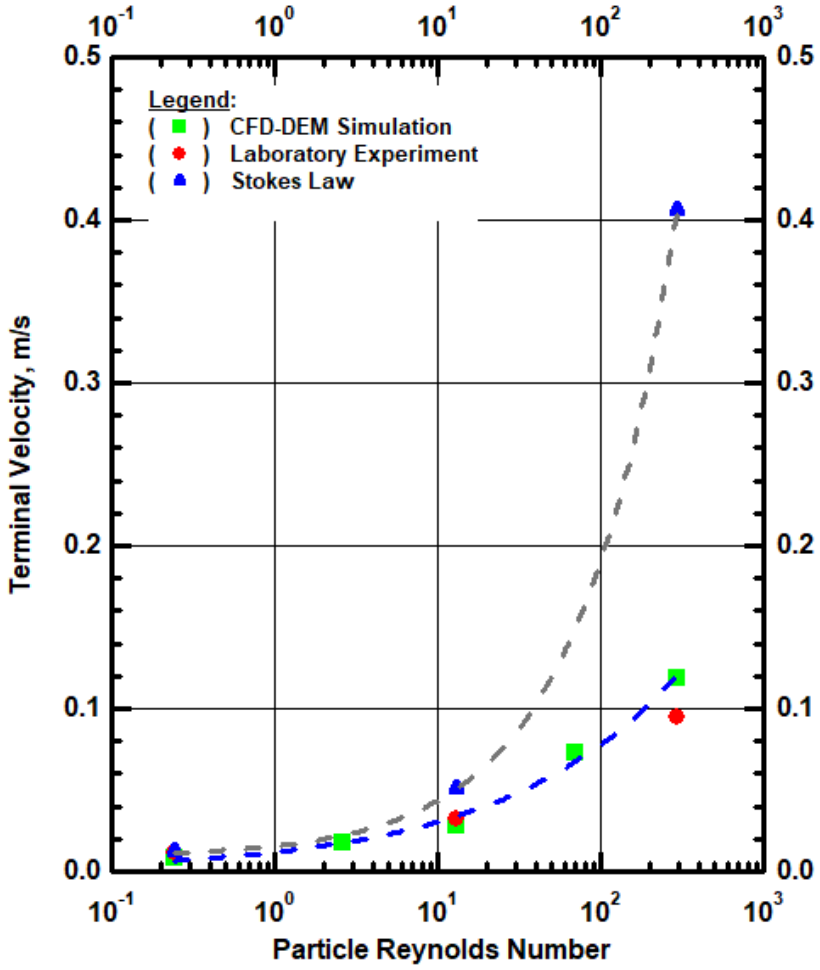

Figure 3.5 Terminal velocity from the CFD-DEM simulation (green cubic) vs Stokes Law (blue triangle) and experimental measurements (red circle)

Fig. 3.5 shows 3 experimental measurements (denoted by red circles; the first red circle is covered by the other two markers), 5 CFD-DEM simulation results and 3 estimates of the

settling velocity computed using the Stokes Law. Note that each of the red circle represents the average from 2 settling test experiments shown in **Table 3.2**. At a low Reynolds number, all three estimates coincide. The terminal velocity estimated from the CFD-DEM simulation matches well with the experimental data, but small deviations from the analytical solution are observed as the particle size increases. These can be attributed to experimental error, as the measurement of the terminal velocity was based on visual observations that were not particularly accurate. For large particle Reynolds numbers, the terminal velocity estimate from the Stokes law is clearly inaccurate because the associated drag coefficient (shown in **Fig. 2.1**) deviates significantly from the actual measurements.

3.2.2. Development of Scaling Relationships

Following the verification of the fundamental force models in my CFD-DEM simulator through the particle scale simulations, I introduced upscaling to the model using the CG-particle method that was briefly mentioned in the introduction. The sheer number of proppant particles (referred to as 'original particles') is so large that it can overwhelm the ability of even the most powerful high-performance computing platforms to describe their flow and behavior. Thus, the only alternative is to use the concept of composite particles (referred-to as 'coarse-grained' or CG-particles) that represent an agglomeration of original particles, coupled with appropriate scaling factors. As discussed earlier, the coarse-grained DEM simulations can speed up the DEM simulations without compromising the accuracy of the results.

To determine the scale factors, I followed the analysis suggested by Chu et al., (2016). I first defined $\boldsymbol{\alpha}$ as the ratio of the radius of a CG particle ($\boldsymbol{R_{cg}}$) to that of an original particle ($\boldsymbol{R_o}$). Thus, each CG particle contains $\boldsymbol{N_p}$ original particles according to

$$\boldsymbol{R_{cg} = \alpha R_o} \quad \text{.....(3.1)}$$

$$\boldsymbol{N_p = \alpha^3} \quad \text{.....(3.2)}$$

I further assumed that the density of the CG particle is the same as that of the original particle ($\boldsymbol{\rho_{cg} = \rho_o}$). Therefore, the mass and mechanical energy of a CG particle are described by **Eq. 3.3-3.4** as

$$\boldsymbol{m_{cg} = \alpha^3 m_o} \quad \text{.....(3.3)}$$

$$\boldsymbol{E_{cg} = m_{cg}\, g + \frac{1}{2} m_{cg} {v_{cg}}^2 = \sum_{i=1}^{Np} E_o = \sum_{i=1}^{Np} (m_o g + \frac{1}{2} m_o {v_o}^2)} \quad \text{.....(3.4)}$$

where $\boldsymbol{E_{cg}}$ is the mechanical energy of the CG particle (J), $\boldsymbol{E_o}$ is the mechanical energy of original particle (J), and all other terms are as previously defined. **Eq. 3.4** shows that when the two particle systems (coarse-grained and original) have the same mechanical energy, the velocity of the CG particle is the same as that of the original particle ($\boldsymbol{v_{cg} = v_o}$). Bringing this observation into the impulse-momentum equation for particles ($\boldsymbol{ft = mv}$), it is easy to show that

$$\boldsymbol{f_{cg} t_{cg} = m_{cg} v_{cg} = \alpha^3 m_o v_o = \alpha^3 f_o t_o} \quad \text{.....(3.5)}$$

where $\boldsymbol{t_{cg}}$and $\boldsymbol{t_o}$ are the acting times of the various forces in the CG and in the original system, respectively.

Bierwisch et al. (2009) and Sakai et al. (2014) suggested that the acting time for fluid-particle impulse should be the same ($t_{cg}{}^{f-p} = t_o{}^{f-p}$) in both systems. Thus, elimination of the time term in **Eq. 3.5** yields the following fluid-particle force relationship:

$$f^{f-p}{}_{cg} = \alpha^3 f^{f-p} \quad \text{.....(3.6)}$$

Eq. 3.6 shows that the fluid-particle force acting on a coarse-grained particle should be equal to the original fluid-particle force multiplied by the scaling factor α^3. I implemented this scaling factor into my CFD-DEM simulator using the high-level Application Programming Interface (API) provided by the CFDEMcoupling. This allows the simulation of large-scale proppant transport within reasonable lengths of computation time.

3.3. Laboratory Proppant Transport Experiments

The two validation simulations discussed in the previous sections were conducted at the particle scale. To test our numerical model at a larger scale, I conducted two more numerical simulation studies to emulate two well-known laboratory proppant transport experiments. The first laboratory experiment is the slot transport experiment, where proppant and fluid are injected from one side of the slot, and motion and accumulation of the proppant are recorded through the transparent walls. The specific slot experiment that I emulated in this study has a single fluid inlet. It was selected because the single inlet enhances the suspension transport regime, which I consider to be the dominant flow regime and responsible for the bulk of proppant transport into the fracture. The second

laboratory experiment that I duplicated numerically involves the equivalent bed height measurement. During this experiment, proppant and fluid are injected in a direction that perpendicular to the main flow direction. In this case the suspension transport is minimized, and bed load transport is enhanced. Agreement of the numerical predictions with the experimental observations provided significant evidence in support of the validation of my CFD-DEM model over a wide range of flow regimes.

3.3.1. Slot Transport Experiment with Single Fluid Inlet

The settling test and the Stokes equation are 2-way coupling problems in which the fluid-to-particle drag force and the gravity force dominate, but do not involve the particle-to-particle and particle-to-wall interactions that are the norm in the case of transport of even low-concentration proppant-carrying fluids. Thus, the confirmation of the ability of the coupled CFD-DEM model to describe such transport is insufficient to provide the confidence needed for the model application to proppant transport in fractures. This is a dense particle transport problem, in which the particle-to-particle forces play an important (and possibly a key) role.

Therefore, it is necessary to test and calibrate my model in a problem involving such a dense particle system. This was accomplished by using the study of Tran et al. (2017), who conducted lab scale experiments to study how PGA (Polyglycolide) fiber increase the transport efficiency of proppant by creating flow channels in the sand dune. **Table 3.4** shows the parameters used in the experiment of Tran et al. (2017), which were also the input parameters in my simulator for this validation study.

Table 3.4 Experimental parameters from Tran et al. 2017

Parameters, units	Value
Length (x direction), cm	120
Height (y direction), cm	30
Width (z direction), cm	0.5
Fluid viscosity, cp	3.5
Particle size, mesh	30-60
Injection rate, ml/min	650

This laboratory-scale experiment involved 2 transparent plates and a slick water injection port. The single injection port is located on the left-hand side of the flume in the apparatus shown in **Fig. 3.6a**. The dimensions of the rectangular apparatus were 30 cm x 120cm x 0.5cm. The experiment involved injection of 30/60 mesh proppant in slick water (with a viscosity of 3.5 cp) at a rate of 650 ml/min. Tran et al. (2017) observed that the proppant settled near the injection port and formed a “dune”.

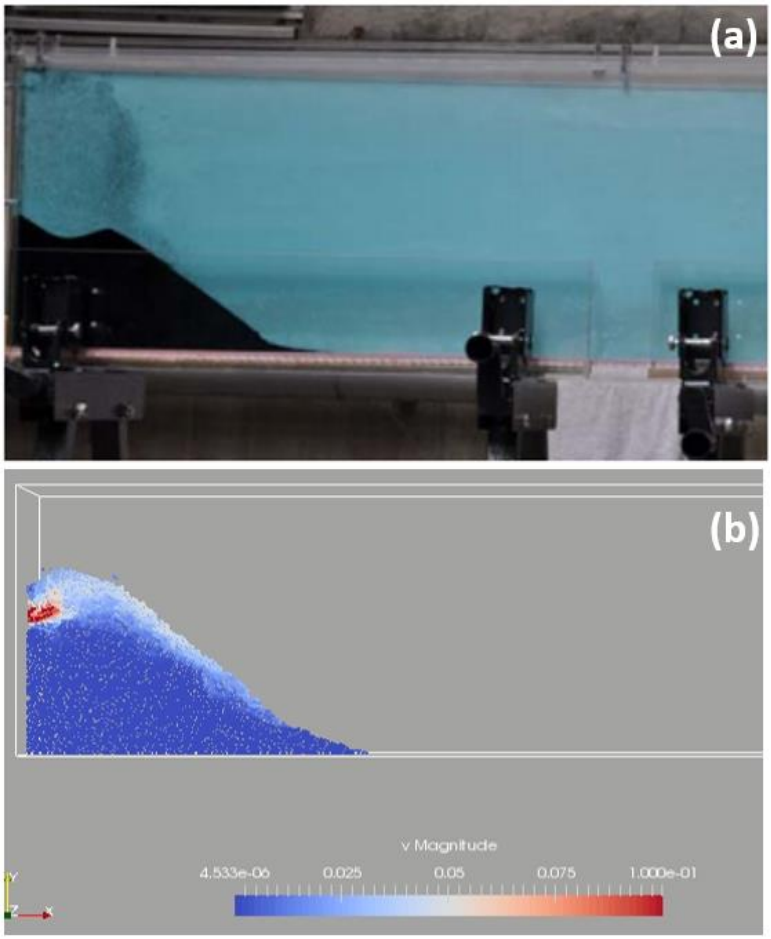

Figure 3.6 Comparison of (a) Lab scale proppant transport experiment (reprinted from Tran et al. 2017), and (b) Lab scale proppant transport simulation using the coupled CFD-DEM model

Fig. 3.6(b) shows the simulation-based predictions of the location and accumulation of the injected proppant particles, as well as the particle velocities. The latter are depicted by the variations in the color of the particles according to the color scale included in the figure. Comparison of the simulation results and the laboratory observations in **Fig. 3.6(a)**

indicates that my simulator captured faithfully the settling behavior in the slot transport experiment in terms of both the shape of the "dune" and its extent (or "reach").

Thus, the simulation reproduced the shape of the sand dune and its frontal and back slopes. The proppants entering the planar fracture have a relatively high velocity (indicated by the red color) because of the fluid drag force. Then, proppants move along the top of the existing dune and gradually lose momentum. Finally, the proppants at near-zero velocity (indicated by the dark blue color) settle, forming the base and the downslope part of the dune. This simulated proppant transport behavior at the laboratory injection rate agrees with other recent experimental studies (*e.g.*, Sahai et al. 2014, Tong et al., 2017), all of which show that the proppants settle and form a bank near the injection point when the injection rate is low. The low viscosity of slick water and the low injection rate in this experimental study caused bed load transport to be the dominating mechanism.

Laboratory experiments can provide valuable insights into the subject of settling behavior of proppants, but they are limited by the magnitude of the fluid velocities that they can accommodate. A larger fluid velocity will exert a larger drag force on the particles and is certain to result in a different system behavior. Because the fluid drag force is the only driving force that transports proppant into the fracture, it is necessary to simulate proppant transport with realistic fluid velocities that correspond to field-level pumping rates. In Section 4, we will show that when fluid velocity reaches a magnitude similar to that attained during the fracturing and stimulation operations in the field, suspension transport becomes the dominating transport mechanism.

3.3.2. Equilibrium Bed Height Experiment

The second laboratory-scale test that I investigated as a validation problem is the equilibrium bed-height experiment. In this experiment, suspension transport is avoided by either injecting the inlet stream in a direction perpendicular to the main flow direction, or by using a low fluid velocity at the injection point.

Patankar et al. (2002) performed a set of equilibrium bed-height experiments and measured the channel height (depicted by H_1 in **Fig. 3.7**). For this validation study, the CFD-DEM simulation domain dimensions and the input parameters describing the system properties and conditions were those reported in the laboratory study of Patankar et al. (2002) and are listed in **Table 3.5**.

Table 3.5 Experimental parameters from Patankar et al., 2002

Parameters, units	Value
Length (x direction), cm	244
Height (y direction), cm	30.5
Width (z direction), cm	0.8
Fluid viscosity, cp	1.0
Particle size, mesh	16-30
Injection rate, ml/s	180.4

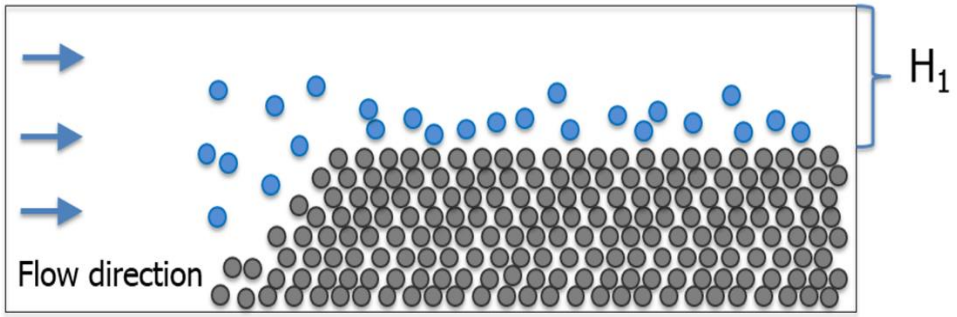

Figure 3.7 Illustration of the equilibrium bed-height experiment and depiction of the open-channel height H_1.

Fig. 3.8 shows a plot of the relationship between the volume fraction of the fluid (ε_f) and the vertical distance (height, measured from the bottom) in the experimental flume. From this ε_f plot, two regions of proppant occurrence are evident: (a) the packed bed region (below the dashed line defining the H_1 region) and (b) the flow channel region (identified by the H_1 parameter). In the packed bed region, ε_f varies from between 0.55 and 0.6. For reference, a perfect cubic lattice packing of mono-sized spheres has a void fraction of 0.476. This packed region has a void fraction larger than that of a perfect cubic lattice packing, which clearly shows the existence of substantial voids in the packing.

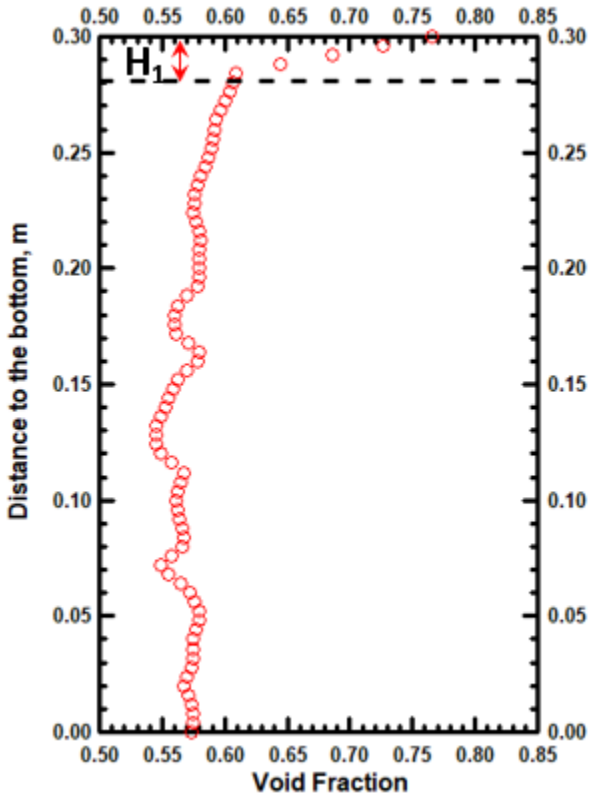

Figure 3.8 Plot of void fraction (fluid volume fraction) as a function of vertical distance

In the flow channel region, ε_f shows a steep increase as the proppant particles approach the top boundary. The sudden change in the ε_f value corresponds to the change of the proppant particles regime from the packing state to a mobile state. The vertical distance from the first mobile layer of proppant to the top boundary of the flow domain is defined as the channel height (H_1). The dashed line in **Fig. 3.8** defines the experimental H_1 value measured by Patankar et al. (2002), which agrees well with the numerical estimate of H_1 that is determined from the sudden change in the slope of the ε_f curve.

The very strong agreement of the laboratory observations and the numerical results indicate that my simulator accurately described the geometry and the physics of this problem (including the force model) of slick water-based proppant interaction and provides additional confidence in the validity of my numerical model.

4. SIMULATOR SPECIFICS AND THE COMPUTATIONAL PLATFORMS

In this section I describe the DEM and CFD codes that I used in the development of my coupled simulator. I also discuss the implementation of the coarse grain function using the Application Programming Interface (APIs) and I provide some basic information on the code compilation process. I also introduce the Texas A&M University supercomputer facilities that I used for this study, and specifically the Ada cluster. Finally, I discuss the parallelization and domain decomposition tests I conducted as part of this study, and the corresponding speedups and efficiencies.

4.1. The DEM Simulator LIGGGHTS

The DEM simulator I used in this study is LIGGGHTS (Kloss et al., 2012). It is an open-source DEM software based on the granular packages of LAMMPS (Plimpton, 1995). Both LAMMPS and LIGGGHTS are written in C++, and offer highly programable input scripts. Installation of LIGGGHTS on the Linux system followed the instructions in the User's Manual (https://www.cfdem.com/media /DEM/docu/Manual.html).

LIGGGHTS executes by reading commands from an input script file named "in.liggghts". Commands are read one at a time. Each command causes the LIGGGHTS executable to take a certain action, including setting the simulation domain boundaries, creating the internal variable, reading the files describing the domain geometry, and running the simulation. An example of a complete "in.liggghts" file is available in **Appendix B**.

The first sets of commands in a "in.liggghts" file define the specifics of the simulation domain. As shown in the code snippet below, the "boundary" command specifies a fixed

domain boundary (as opposed to a moving boundary) in all directions. The dimensions of the simulation domain are in SI units. In the snippet, I create a region that is 10 meters long (in the *x*-direction), 2 meters high (from -1 to +1 in the *y*-direction), and 0.1 meters wide (in the *z*-direction). The simulation domain comprises a single region, *i.e.*, the entire domain is that defined by the region described above. For the calculation of the collisions between neighboring particles, the cut-off distance of 0.003 m. This means that only particles within the cut-off distance will be considered in the collision list.

```
boundary        f f f
units           si
region          reg block 0 10 -1 1 0 0.1 units box
create_box      1 reg
neighbor        0.003 bin
```

Figure 4.1 LIGGGHTS commands to set up simulation domain

The powerful "*fix*" command is used to achieve several functions. As shown in the code snippet **Fig. 4.2**, the *fix* command can be used to describe the particle properties, including the Young's modulus of elasticity, the Poisson ratios, the coefficient of restitution and the friction factor. It can also be used to set the simulation time step and the global external force (= gravity). The *fix* command is commonly used to create walls in the simulation domain. In this example, I created 4 geometry files (named geometry0.stl, geometry1.stl, geometry2.stl, geometry3.stl) using the Paraview package (a powerful 3D plotting software, Ayachit 2015), and then imported these geometries as walls using the *fix*

command. The *fix* command is also used to create a particle "source" region and to specify the quantity and frequency of the particles that are generated in the source region.

```
# Material properties required for granular pair styles
fix         m1 all property/global youngsModulus peratomtype 5.e6
fix         m2 all property/global poissonsRatio peratomtype 0.45
fix         m3 all property/global coefficientRestitution
peratomtypepair 1 0.4
fix         m4 all property/global coefficientFriction
peratomtypepair 1 0.5
# timestep, gravity
timestep    0.00001
fix         gravi all gravity 9.8 vector 0.0 -1.0 0.0

# read walls
fix     geo0 all mesh/surface file ../DEM/geometry0.stl type 1
fix     geo1 all mesh/surface file ../DEM/geometry1.stl type 1
fix     geo2 all mesh/surface file ../DEM/geometry2.stl type 1
fix     geo3 all mesh/surface file ../DEM/geometry3.stl type 1

# walls
fix     xwalls1 all wall/gran model hertz tangential history
primitive type 1 xplane 0
fix     xwalls2 all wall/gran model hertz tangential history
primitive type 1 xplane 10
fix     ywalls1 all wall/gran model hertz tangential history
primitive type 1 yplane -1.0
fix     ywalls2 all wall/gran model hertz tangential history
primitive type 1 yplane 1.0
fix     zwalls1 all wall/gran model hertz tangential history
primitive type 1 zplane -2.98
fix     zwalls2 all wall/gran model hertz tangential history
primitive type 1 zplane 0.08
fix     otherwalls all wall/gran model hertz tangential history
mesh n_meshes 4 meshes geo0 geo1 geo2 geo3

# create single partciles
region      bc block 0 0.5 0 0.1 0.045 0.055 units box
fix                 pts1 all particletemplate/sphere 15485863
atom_type 1 density constant 2650 radius constant 0.005
fix                 pdd1 all particledistribution/discrete
15485867  1 pts1 1.0

fix             ins all insert/rate/region seed 32452843
distributiontemplate pdd1 vel constant 1 0 0 nparticles 1500000
particlerate 15000 insert_every 100 overlapcheck yes region bc
```

Figure 4.2 LIGGGHTS command that utilize the "fix" function.

The “variable” command is invoked to create the appropriate variables and obtain the desired outputs from the application of LIGGGHTS. **Fig. 4.3** below shows the use of the *variable* command to (a) create the variables *vx*, *vy*, *vz* and *time* and (b) to monitor and print their evolution over time in a file named “velocity.txt”. Also Fig. 4.3 shows how to store the simulation output (locations, velocity and forces) for every 10,000 timesteps into the “dump.liggghts_run” file.

```
variable    vx equal vx[1]
variable    vy equal vy[1]
variable    vz equal vz[1]
variable    time equal step*dt
fix         extra all print 10000 "${time} ${vx} ${vy} ${vz}" file
../DEM/post/velocity.txt title "#" screen no

dump    dmp all custom 10000 ../DEM/post/dump.liggghts_run id type
x y z ix iy iz vx vy vz fx fy fz omegax omegay omegaz radius time
```

Figure 4.3 LIGGGHTS command that create variable and monitoring their evolution over time.

As a DEM software, LIGGGHTS is endowed with a highly programable input script. From my experience with LIGGGHTS, the desired functionality can be achieved by creating variables and combining built-in functions within the input script.

4.2. The CFD Simulator OpenFOAM

The CFD simulator I used in this study is based on the OpenFOAM standard solver libraries (Weller et al., 1998). These open source libraries are written in C++. Installation of OpenFOAM on a computational platform running the Linux system (such as the Ada

supercomputer) is described in the installation manual (https://openfoam.org/download/7-ubuntu/). One of the greatest benefits of using `OpenFOAM` is that it offers many pre-built CFD solvers. Each solver is a separate CFD simulator implemented using a different governing equation. Among the base solver libraries, `icoFOAM` is the solver applicable to my formulation (without coupling with particles). The momentum conservation equation solved in `icoFOAM` is:

$$\boldsymbol{\rho}\frac{\boldsymbol{\partial}(\boldsymbol{\varepsilon_f}\overrightarrow{\boldsymbol{u_f}})}{\boldsymbol{\partial t}} + \boldsymbol{\rho}[\overrightarrow{\boldsymbol{u_f}} \cdot \boldsymbol{\nabla}(\boldsymbol{\varepsilon_f}\overrightarrow{\boldsymbol{u_f}})] = \boldsymbol{\nabla} \cdot \overleftrightarrow{\boldsymbol{\sigma}} + \boldsymbol{\rho}\boldsymbol{\varepsilon_f}\vec{\boldsymbol{g}} \quad \text{.....(4.1)}$$

Eq. 4.1 is implemented in `OpenFOAM` using the code shown in **Fig 4.4**

```
// Momentum predictor
fvVectorMatrix UEqn
(
     fvm::ddt(U)
  +  fvm::div(phi, U)
  -  fvm::laplacian(nu, U)

);
```

Figure 4.4 OpenFOAM code to implement momentum conservation equation shown in Eq. 4.1

In **Fig. 4.4**, the various terms are as explained below:

- `fvm::ddt(U)` is the API for calculating the accumulation term $\boldsymbol{\rho}\frac{\boldsymbol{\partial}(\boldsymbol{\varepsilon_f}\overrightarrow{\boldsymbol{u_f}})}{\boldsymbol{\partial t}}$
- `fvm::div(phi,U)` is the API for calculating the divergence term $\boldsymbol{\rho}[\overrightarrow{\boldsymbol{u_f}} \cdot \boldsymbol{\nabla}(\boldsymbol{\varepsilon_f}\overrightarrow{\boldsymbol{u_f}})]$
- `fvm::laplacian(nu,U)` is the API for calculating the viscous force term $\boldsymbol{\nabla} \cdot \overleftrightarrow{\boldsymbol{\sigma}}$

Comparison of **Eq. 4.1** to the momentum conservation equation in the coupled CFD-DEM formulation (Eq. **2.10**) reveals that the only difference between the two is the term of the summation of the external particle forces ($\frac{\mathbf{1}}{\boldsymbol{V_{cell}}}\sum_{\boldsymbol{i=1}}^{\boldsymbol{kv}}\vec{\boldsymbol{f}}_{\boldsymbol{i}}^{\boldsymbol{f-p}}$): it is on the right-hand side of Eq. 2.10, but absent from Eq. 4.1. However, it is easy to implement the missing term by using a high-level API available in `OpenFOAM`. The necessary commands to fully implement Eq. 2.10 in `OpenFOAM` are described in the **section 4.3**.

The high-level APIs provides `OpenFOAM` with significant flexibility, allowing the implementation of a wide range of user-specific formulations and enhancing the code legibility. However, to implement a new solver with non-standard formulations, substantial effort is needed in order to navigate through the API documents and to test the compatibility of the standard and the user-specified API functions. To use `OpenFOAM` without modifying the standard solvers, a user only needs to generate the mesh of the simulation domain and to provide the information on how the simulation is to be conducted in the input file. An example of (a) a mesh file (named `blockMeshDict`) creating a vertical fracture model and (b) of the corresponding running specification file (named `ControlDict`) for an `OpenFOAM` simulation can be found in **Appendix B**.

4.3. The Coupling software CFDEMcoupling

I use the `CFDEMcoupling` software (Kloss et al., 2012) to couple `LIGGGHTS` and `OpenFOAM`. `CFDEMcoupling` is an open source software written in C++ (Kloss et. al, 2012). Instructions for the installation of `CFDEMcoupling` on a standard Linux machine are found on the user manual section of the CFDEM website

(cfdem.com/media/CFDEM/docu/CFDEMcoupling_Manual.html). Installation of `CFDEMcoupling` on a supercomputing cluster requires working with the system administrator in order to correctly set up the environment variables for the operating system of the supercomputer.

The process for coupling `LIGGGHTS` and `OpenFOAM` using `CFDEMcoupling` involved the following steps:

1. Compilation of `OpenFOAM` to generate the standard solver library and utility executables.
2. Compilation of `LIGGGHTS` to generate the dynamic library
3. Compilation of `CFDEMcoupling` as a modified CFD solver by calling a utility executable from `OpenFOAM`. This modified solver also calls the `LIGGGHTS` dynamic library during run time.

This process essentially creates a modified version of the `OpenFOAM` solver.

Recall the Model-A formulation of the momentum conservation equation of fluid phase (Eq. 2.11). The code snippet in **Fig. 4.5** below shows how **Eq. 2.11** is implemented as a modified solver using the high-level `OpenFOAM` APIs. This process is similar to the `icoFOAM` solver we explained in Section 4.2.

```
// Momentum predictor

fvVectorMatrix UEqn

(

fvm::ddt(voidfraction,U) - fvm::Sp(fvc::ddt(voidfraction),U)

+ fvm::div(phi,U) - fvm::Sp(fvc::div(phi),U)

+ particleCloud.divVoidfractionTau(U, voidfraction)

==

- fvm::Sp(Ksl/rho,U)

+ fvOptions(U)

);
```

Figure 4.5 OpenFOAM code to implement momentum conservation equation shown in Eq. 2.11

The various items in the snippet of **Fig. 4.5** are as follows:

- `fvm::ddt(voidfraction,U)` is the API for calculating the accumulation term $\frac{\partial(\varepsilon_f \mathbf{u_x})}{\partial \mathbf{t}}$
- `fvm::div(phi,U)` is the API for calculating the divergence term $\frac{\partial \varepsilon_f \mathbf{u_x u_x}}{\partial \mathbf{x}} + \frac{\partial \varepsilon_f \mathbf{u_x u_y}}{\partial \mathbf{y}} + \frac{\partial \varepsilon_f \mathbf{u_x u_z}}{\partial \mathbf{z}}$
- `particleCloud.divVoidfractionTau(U,voidfraction)` is the term for calculating external force from the particles $\frac{1}{V_{cell}} \sum_{i=1}^{kv} ([\vec{f}_i^{\,d}]_x)$. This API will trigger LIGGGHTS simulator.

- `fvm::Sp(Ksl/rho,U)` is the API for calculating the viscous force term $\frac{1}{\rho}\left(\frac{\partial \varepsilon_f \tau_{xx}}{\partial x}+\frac{\partial \varepsilon_f \tau_{xy}}{\partial y}+\frac{\partial \varepsilon_f \tau_{xz}}{\partial z}\right)$
- `fvOptions(U)` is the API for calculating optional forces, including gravity.

To implement the Coarse Graining (CG) method I used in this study (see Section 3.2), I also used the OpenFOAM high-level API. Recall the scaling factor $\boldsymbol{\alpha}$ for the fluid-particle force (**Eq. 3.6**), and that the fluid-particle force is multiplied by a factor of $\boldsymbol{\alpha^3}$ to ensure that the CG particle have the same trajectory as the original particle. To implement the scaling factor $\boldsymbol{\alpha}$, I invoked the `OpenFOAM` APIs described in the code snippet in **Fig. 4.6**.

```
forceModels
(
    DiFeliceDrag
);

DiFeliceDragProps
{
    velFieldName "U";
    voidfractionFieldName "voidfraction";
    granVelFieldName "Us";
    verbose false;
    scaleDrag 1000;
    //- use of scalar viscosity for drag
    //scalarViscosity true;
    //nu [ 0 2 -1 0 0 0 0 ] 1e-04;
}
```

Figure 4.6 OpenFOAM code to implement Coarse Graining method

In the snippet of **Fig 4.6**, I construct a `forceModels` data structure (list) and initialized the `forceModels` list with one `DiFeliceDrag` object. Then I call the

`DeFeliceDragProps` API to modify the `DeFeliceDragProps` dictionary. The "`scaleDrag`" keyword (an optional scaling factor that allows the application of an unproportionally large drag force) is set to a value of 1000. This is the $\boldsymbol{\alpha^3}$ scaling factor in **Eq. 3.6** for the case of CG particles that are 10 times the size of the original particles. Note that the default value for the `scaleDrag` parameter is 1. The CG method makes possible the significant reduction in the number of monitored/tracked particles and the completion of large-scale proppant transport simulations within an acceptable time.

4.4. The Ada Cluster at High Performance Research Center

For the needs of this study, I used the three high performance computer clusters (Ada, Curie and Terra) that are available to Texas A&M University students for large-scale parallel computations. I used mostly the Ada cluster (see **Fig. 4.1**), which has the largest number of computation nodes — 856 computational nodes and 17,436 cores in total — and the largest library of installed software.

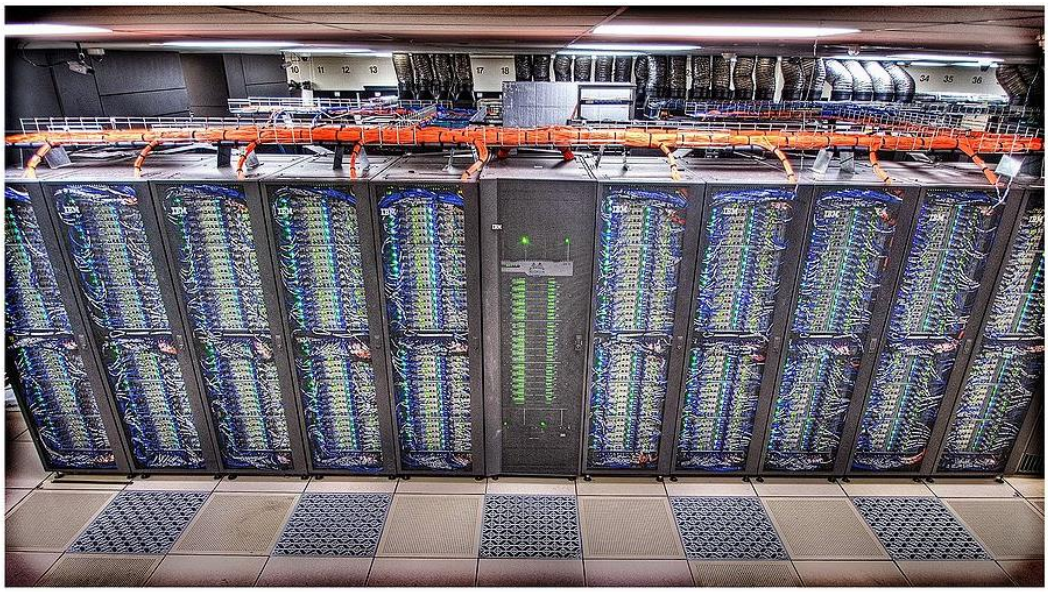

Figure 4.7 Computation rack of Ada cluster (reprinted from https://hprc.tamu.edu/wiki/Ada:Intro)

The majority (792 out of 856) of the Ada computational nodes are IBM NeXtScale nx360 M4 dual socket servers, each one of which has two Intel Xeon 10-core processor. This computation node is commonly known as the Ivy Bridge. **Fig. 4.8** shows the Ivy Bridge architecture, which involves 10 cores and 32 GB of memory for each processor. Every two processors are connected through a QuickPath interconnect, which makes the Ivy-bridge computational nodes "appear" to have 20 cores. The communication between nodes is through a FDR-10 Infiniband.

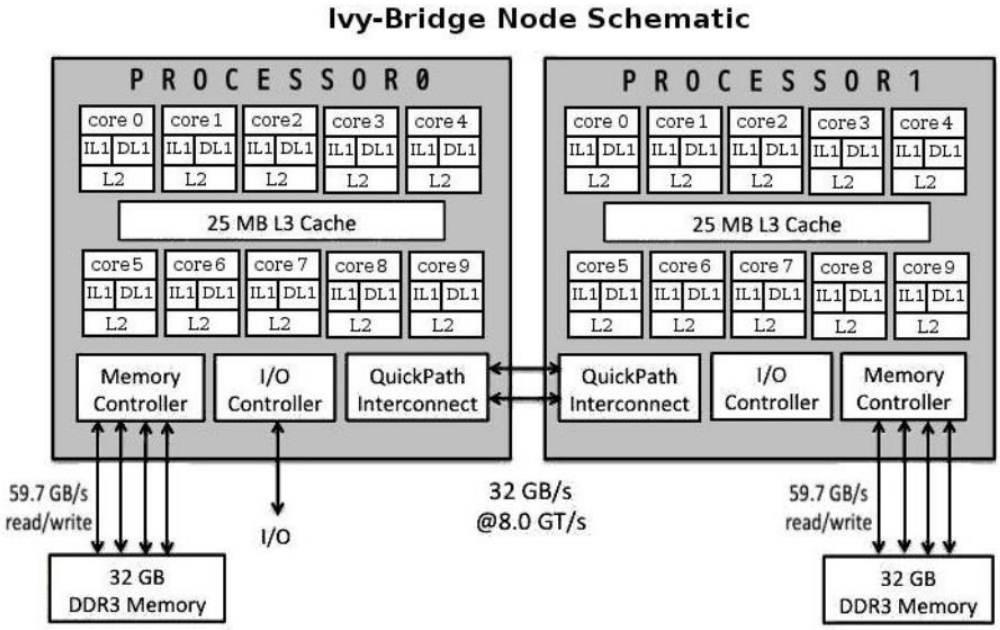

Figure 4.8 Architecture of the Ivy-bridge computation node in Ada cluster (reprinted from https://hprc.tamu.edu/wiki/Ada:Intro)

Computational tasks (*i.e.*, numerical simulations) on the Ada cluster are submitted to the queueing system using a job file. The computational job is assigned to different queues

based on two criteria: (1) the total number of cores requested by the job file, and (2) the computation time requested by the job file. The code snippet in **Fig. 4.9** shows an example of a job file I used to submit a CFD-DEM simulation. In this example job file, I requested (a) 24 hours of computation time and (b)10 cores, enforcing that (c) the 10 cores be on the same node.

```
##NECESSARY JOB SPECIFICATIONS

#BSUB -J CFDEM_Frac1         #Set the job name

#BSUB -L /bin/bash           #Uses the bash login shell

#BSUB -W 24:00                #Set the wall clock limit to 24hr

#BSUB -n 10                   #Request 10 core

#BSUB -R "span[ptile=10]"     #Request 10 core per node.

#BSUB -R "rusage[mem=5000]"  #Request 5000MB per process (CPU) for

the job

#BSUB -M 5000                #Set the per process enforceable

memory limit to 5000MB.

#BSUB -o Vertical_frac_Out.%J      #Set output file name

##OPTIONAL JOB SPECIFICATIONS

#BSUB -P 123456              #Set billing account to 123456

#BSUB -u email_address       #Send all emails to email_address

echo "start time"
date
./Allrun.sh
echo "finish time"
date
```

Figure 4.9 Example code to submit CFD-DEM simulation to Ada cluster

Even though there is a large collection of pre-installed software on the Ada cluster, the coupling `CFDEMcoupling` software I needed for my study was not pre-installed. As discussed earlier, the installation of this piece of software is quite complex and was accomplished only with the help of the system administrator because the process required setting of the environmental variables necessary to locate the fundamental libraries (*e.g.*, `glibc`) and the versions that were compatible with the source code. Thus, on the Ada cluster, the user needs to load the specific library modules and select the appropriate version. The Bash script (written by the system administrator) that automated the process of loading modules and setting the appropriate environmental variables that enabled the simulations of my coupled CFD-DEM code appears in Appendix B.

4.5. Domain Decomposition of the Simulation and Efficiency

To speed up the parallelized numerical simulations in this study, I used a domain decomposition method. Fig. 4.4 shows one of the decomposition scenarios, in which I decomposed the vertical fracture domain along its length (x-direction) into 10 subdomains. Computations within each subdomain are performed on a single core, and the boundary values of each of the subdomain are communicated using the Message Passing Interface (MPI) framework. Both the `OpenFOAM` and the `LIGGGHTS` software come with MPI fully implemented.

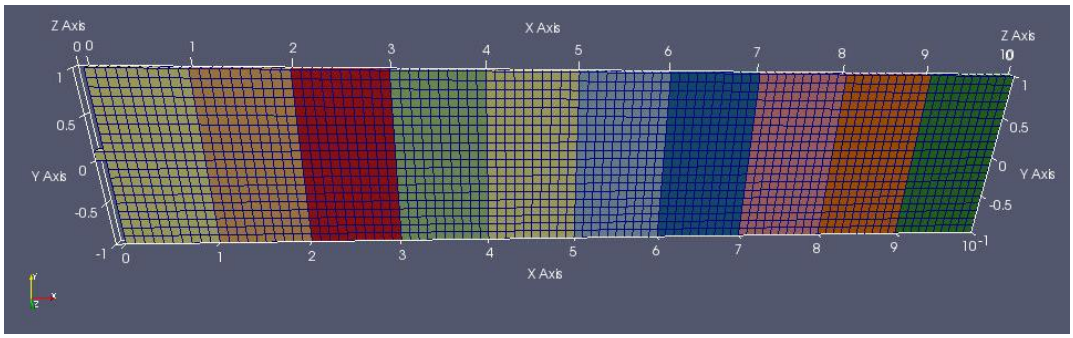

Figure 4.10 Vertical fracture simulation domain decomposed into 10 subdomains, each represented by a different color

To determine the optimal domain decomposition scheme, I conducted speed-up and efficiency tests using up to 40 cores. Each test case involved the solution of the vertical fracture problem (details are available in Section 5.2) for 5000 CFD timesteps, recording the time needed to complete the simulation, and calculating the speed-up and efficiency.

Fig. 4.11 shows the parallel computation time using up to 40 cores. Initially, there is a rapid reduction in the computation time as the number of cores N_c increases from 1 to 10, but further reductions in the execution time become progressively smaller as N_c increases from 10 to 40. **Figs. 4.12** and **4.13** show the speed-up and efficiency for the test case.

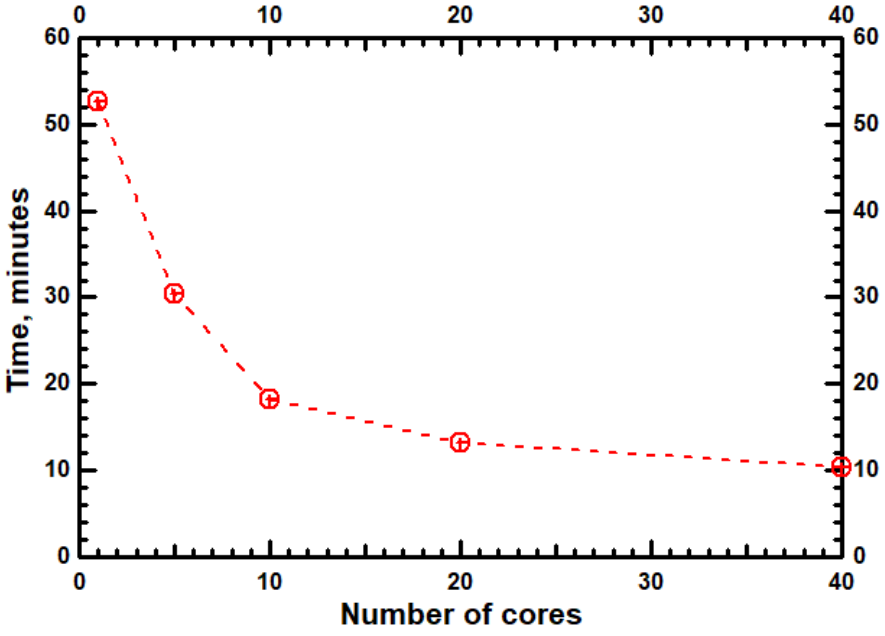

Figure 4.11 Computation time for 5,000 timesteps simulation using various number of cores, ranging from 1 to 40 cores

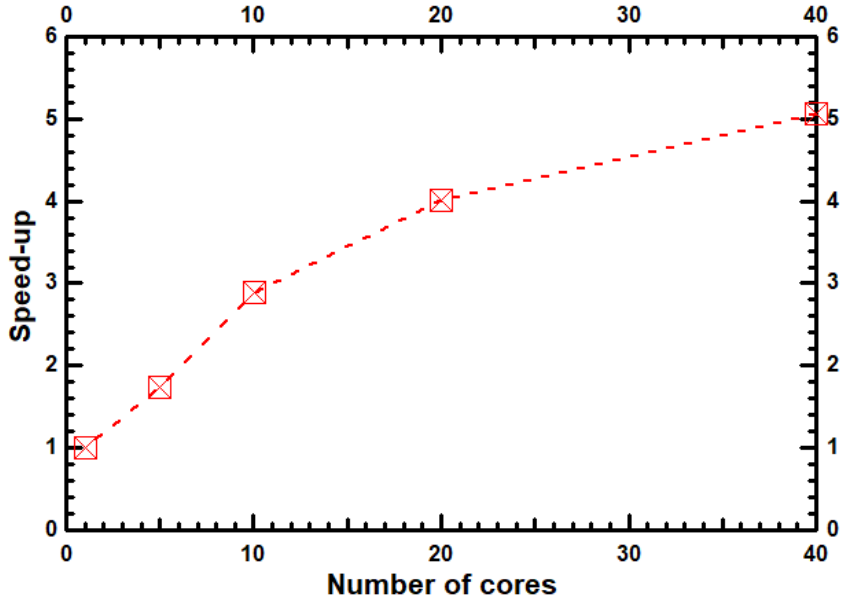

Figure 4.12 Parallel speed-up performance using various number of cores, ranging from 1 to 40 cores

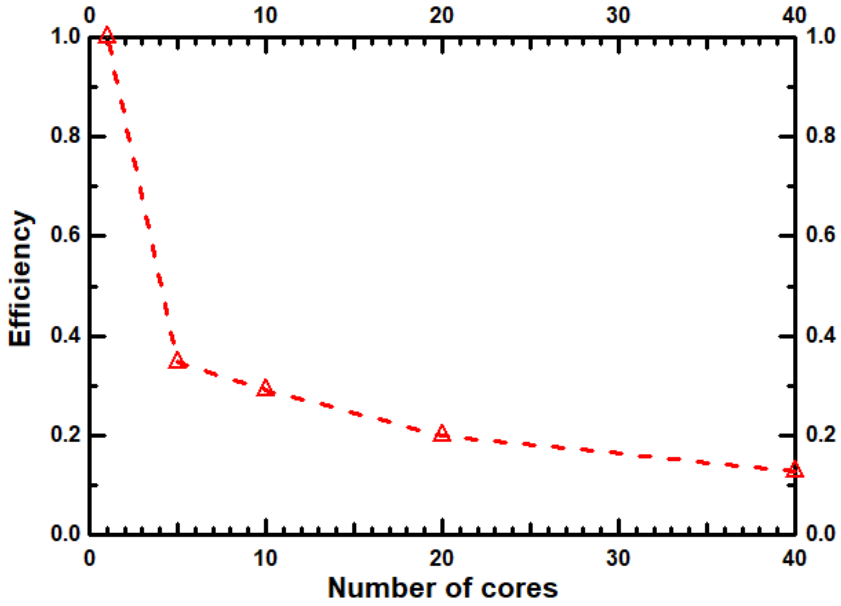

Figure 4.13 Parallel efficiency for using various number of cores, ranging from 1 to 40 cores

This test showed that increasing the number of cores (N_c) reduced the computation time. But increasing N_c above 10 resulted in diminishing returns. Thus, I decided to use 10 cores for the rest of the study, because (a) this N_c leads to a significant reduction in the computation time (compared to that for N_c = 1), (b) it represents a rather minor fraction of the computational resources of the Ada cluster, thus avoiding the job scheduling problems associated with large processor requests, and (c) it does not generate a large number of small-sized output files that would make the post processing of the simulation results a laborious task.

5. PROPPANT TRANSPORT IN VERTICAL AND DIPPING FRACTURES

Here I discuss the transport of proppants in vertical and dipping fractures. In **Section 5.1** briefly review the subject of the orientation of subsurface hydraulic fractures, and I provide evidence for the need to study dipping fractures. In **Sections 5.2** and **5.3**, I discuss the vertical fracture model that is used as the base case in this investigation, and I analyze the fluid and particle velocity profiles and regimes, as well as the corresponding proppant placement efficiencies at different distances from the injection point. In **Sections 5.4** and **5.5** I investigate the effect of the dipping angle on the proppant placement performance of three hydraulic fractures with different orientations.

5.1. Orientation of Subsurface Hydraulic Fractures

This section focuses on the study and analysis of proppant transport in planar (vertical or inclined) hydraulic fractures (HF). Hydraulic fractures are routinely assumed to be vertical, and this assumption is practically always followed in numerical simulation studies. A vertical fracture implies that the least principal stress is horizontal. However, field studies (Wright et al. 1998, Dinh et al. 2009) have shown that hydraulic fractures are rarely perfectly vertical. Kevin et al. (2017) showed that the majority of HFs in their Eagle Ford producer have a dipping angle of 75º-80º.

Wright et al. (1995) provided field examples showing that the dipping angle of HFs varied between 82º to 45º in two fracturing treatments over a long production period**. Fig. 5.1** shows several hydraulic fracture orientations in the Eagle Ford field, as reported by Raterman et al. (2017). These measurements were interpreted based on image logs and

calibrated using multiple real cores from the shale subsurface. Raterman et al. (2017) showed that the majority of the hydraulic fractures in the Eagle ford field are not vertical, but with a dipping angle in the 75º-80º range. Given that vertical fractures rarely exist in the subsurface, it is important to study how the dipping angle can influence the transport efficiency of proppants.

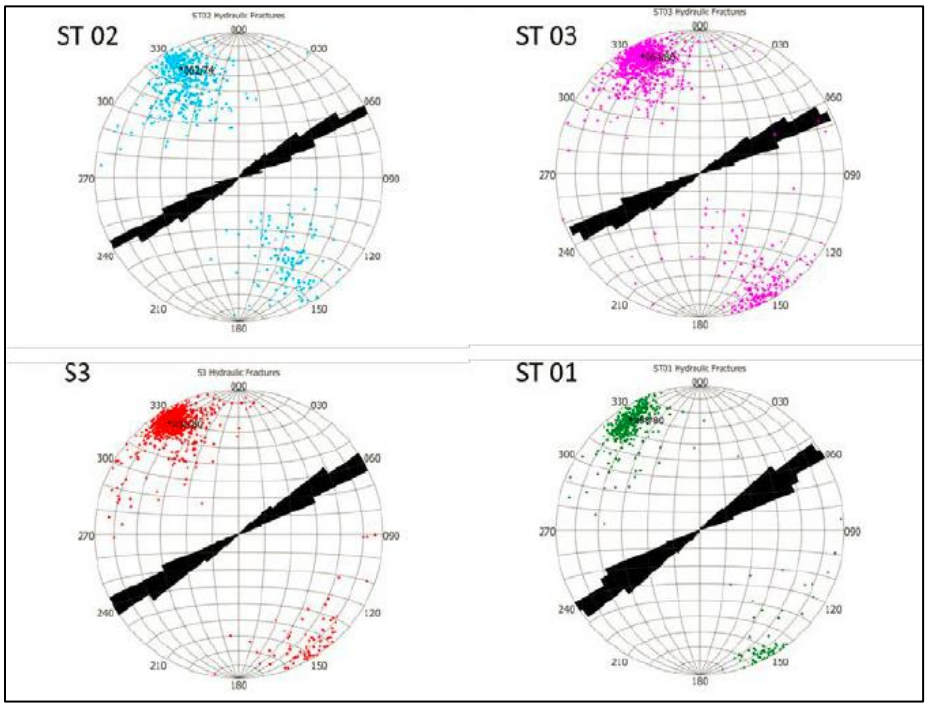

Figure 5.1 Hydraulic fracture orientation from image logs (reprinted from Raterman et al., 2017), each dot represent a fracture identified from the Image Logs.

For this study, I created vertical HFs, as well as dipping HFs, in order to study the influence of fracture dipping angle on the efficiency of proppant transport and placement. **Fig. 5.2** illustrates some of the HF geometries and orientations that I investigated.

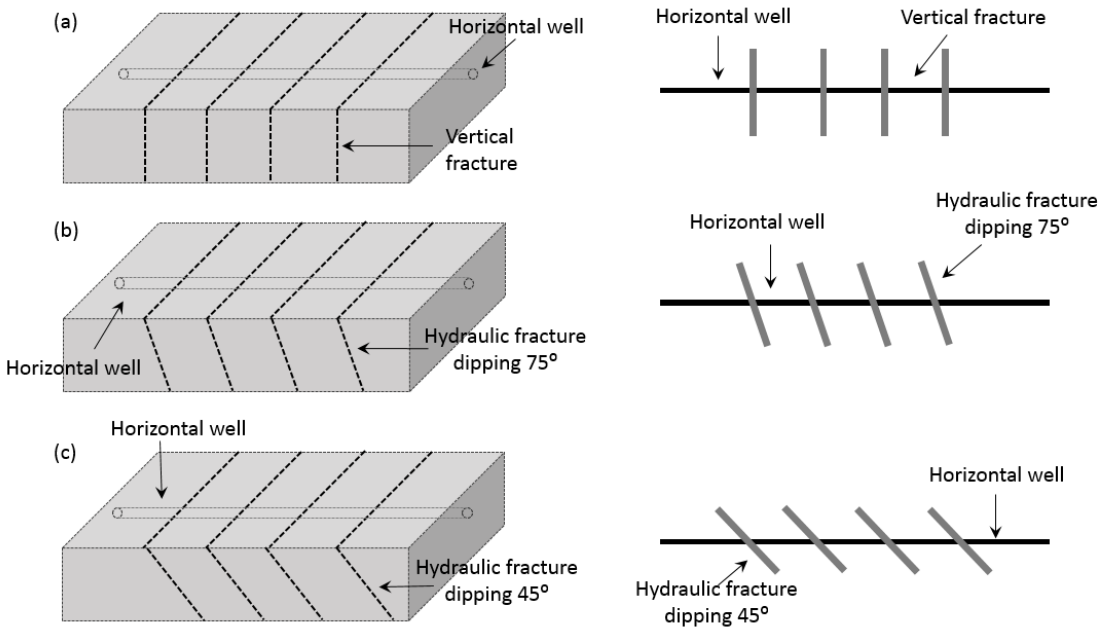

Figure 5.2 3D and 2D side view of (a) vertical hydraulic fractures, (b) dipping 75° hydraulic fractures, and (c) dipping 45° hydraulic fractures

The four planar simulation domains that I constructed represented subsurface HFs with dipping angles of 45º, 60º, 75º and 90º. The vertical (90º dipping angel) HF is the base case. The vertical and horizontal proppant velocity profiles associated with this case, and the corresponding extent of the proppant placement are compared to the those in the remaining three scenarios of inclined HFs. Detailed information on the simulation domains and the system properties and conditions in the vertical and the dipping fracture cases is provided in **Sections 5.2** and **5.4**.

5.2. Simulation Domain and System Conditions in the Study of Vertical Hydraulic Fractures

The scale of the domain that I consider in these simulations is sufficiently large to approach that in field operations. The simulation domain is half of the hydraulic fracture model in **Fig. 5.3(a),** in which the fluid inlet is defined by the intersection of the HF and the horizontal well and is denoted by an arrow.

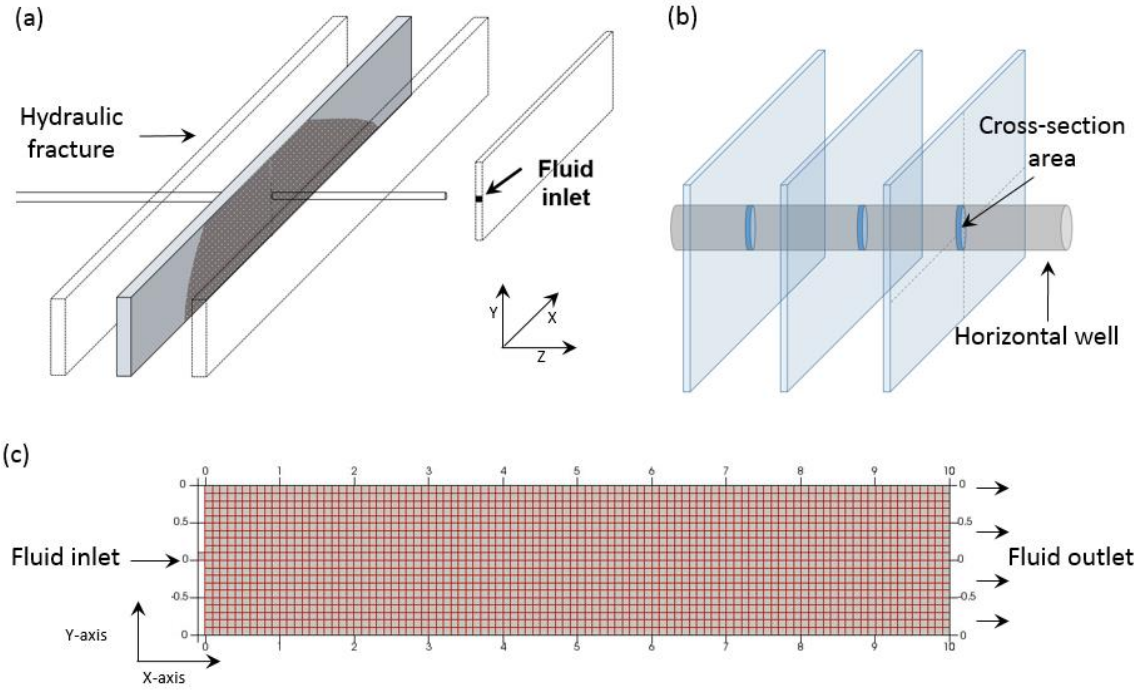

Figure 5.3. 3D illustration of (a) horizontal wellbore with multiple vertical hydraulic fractures (b) the Cross-section area between horizontal wellbore and hydraulic fracture plane and (c) 2D side view of the CFD simulation mesh for hydraulic fractures

Only half of the fracture illustrated in **Fig. 5.3(a)** needs to be simulated because of the assumption that the bi-wing hydraulic fracture is symmetrical about the vertical plane that passes by the length of the HF (**Figs. 5.3(a)** and **5.3(b)**). **Fig. 5.3(c)** provides a detailed description of the simulation domain, including its orientation, dimensions, boundary conditions (inlet and outlet) and discretization. The domain is discretized into the 2000 cells of uniform size (0.1m×0.1m×0.01m) that are shown in **Fig. 5.3 (c)**. The parameters of the vertical simulation domain are shown in **Table 5.1**.

Table 5.1 Parameters for the vertical planar fracture simulation domain

Parameters	SI Units	Field Units
Height, $\boldsymbol{h_f}$	2 m	6.56 ft
Length, $\boldsymbol{x_f}$	10 m	32.8 ft
Aperture, $\boldsymbol{w}$	0.01 m	0.4 inch
Inlet velocity, $\boldsymbol{v_{in}}$	5 m/s	16.4 ft/s
Outlet velocity, $\boldsymbol{v_{out}}$	0.25 m/s	0.82 ft/s

To introduce proppant particles into the HF, the simulation domain was expanded to include a "proppant tank" cell at the injection location, but outside the vertical boundary of the active HF domain. At each DEM time step, proppant particles with zero velocity were randomly generated in the *proppant tank* cell. During the CFD simulation, proppants

in the tank cell were mobilized and injected into the fracture domain by the fluid drag force.

To convert the surface pumping rate (in bpm) to fluid velocity at the inlet, I assumed that the horizontal well has a 5-inch production casing and that the slick water (the fracturing fluid) flowing through the wellbore cross-sectional area (*i.e.*, the surface area of the well-HF interface, see **Fig. 5.3b**) is evenly distributed among the HFs. The surface pumping rate is converted into the inlet boundary condition, *i.e.*, the inlet velocity, by the following equation:

$$\boldsymbol{V_{inlet}} = \frac{\boldsymbol{Q_{surface}/N_{cluster}}}{\boldsymbol{Cross\ Section\ Area_{inlet}}} = \boldsymbol{C} \times \frac{\boldsymbol{Q_{surface}/N_{cluster}}}{\boldsymbol{\pi \times OD_{casing} \times w_{frac}}} \quad (5.1)$$

where $\boldsymbol{Q_{surface}}$ is the surface pumping rate, in barrels per minute (bpm); $\boldsymbol{N_{cluster}}$ is the number of perforation clusters per fracturing stage; $\boldsymbol{OD_{casing}}$ is the diameter of the casing (in); $\boldsymbol{w_{frac}}$ is the fracture width (in); $\boldsymbol{V_{inlet}}$ is the inlet velocity (m/s); and C is a unit conversion constant that ensures results in SI units (m/s).

Assuming five perforation clusters per fracture stage, **Eq. 5.1** leads to an estimate of an inlet velocity of (a) 4.58 m/s for a surface pumping rate of 35 bpm, and (b) to an inlet velocity of 9.15 m/s for a surface pumping rate of 70 bpm. Note that the inlet velocity is defined as the fluid velocity at the intersection of the horizontal wellbore and the planar fracture. For the same surface pumping rate, the corresponding fracture inlet velocity can vary from case to case, as it can be influenced by factors such as the number of clusters per stage and the actual number of fractures per cluster.

Using the domain described above, we performed a series of simulations describing the injection into the hydraulic fracture and flow of slick water carrying 30/60 mesh proppant (*i.e.*, with a uniform particle diameter of 0.425 mm). **Table 5.2** shows all the cases in my study of proppant transport in vertical fractures. By varying the inlet velocity in cases V_1 - V_3, I investigated how the injection rate can influence the proppant transport in the vertical fracture. By varying the friction factor and the coefficient of restitution in cases V_4 - V_7, I investigated the sensitivity of our simulation results to these two parameters.

Table 5.2 Simulation cases created using the vertical fracture model

Case Number	Inlet Velocity V_{inlet}, m/s	Coefficient of Restitution ***e***	Friction factor **μ**
V_1	5.0	0.4	0.5
V_2	2.5	0.4	0.5
V_3	10.0	0.4	0.5
V_4	5.0	0.4	0.3
V_5	5.0	0.4	0.7
V_6	5.0	0.2	0.5
V_7	5.0	0.6	0.5

5.3. Simulation of Proppant Transport in Vertical Hydraulic Fractures

Case V_1 (inlet velocity = 5m/s) is the base (reference) case. **Fig. 5.4** shows snapshots of the spatial distributions of the fluid velocity in the hydraulic fracture at 4 different times in Case V_1. Near-zero fluid velocities are an indication of the occurrence of immobile proppant particles that form the base (and later the bulk) of the proppant bed. Thus, the footprint of the zero (and near-zero) to low fluid velocities is expected to be an analog of the particle bank and a good approximation of the bank shape. The situation is different with the larger fluid velocities that are concentrated at the top of the low-velocity footprint, because these cannot easily provide an indication of the occurrence of proppant particles, as higher velocities can easily occur in the absence of proppants.

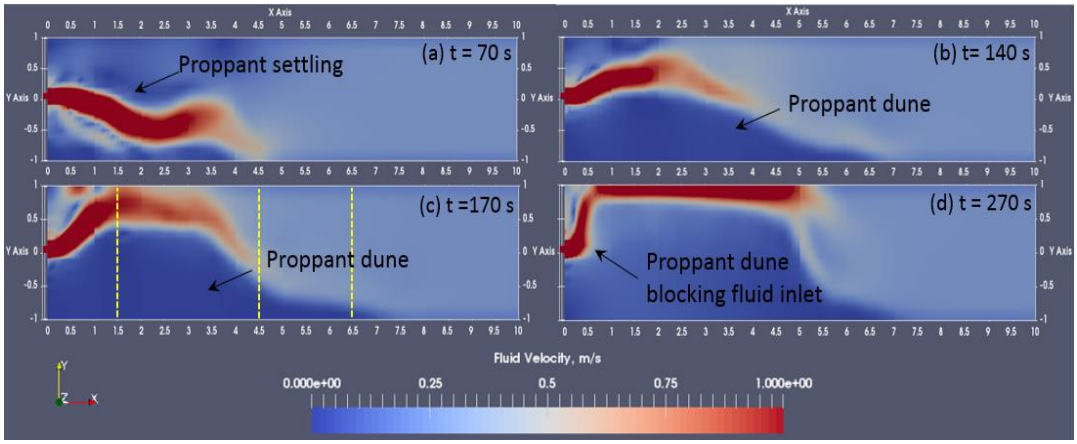

Figure 5.4 Fluid velocity field in the vertical hydraulic fracture at an inlet velocity of 5m/s, at (a) t=70s, (b) t=140s, (c) t=170s and (d) t=270s

At t=70 s, **Fig. 5.4(a)** shows the initial settling movement of the proppant slurry. At t =140 s**, Fig. 5.4(b)** shows that the proppant dune begins to form near the injection inlet. After the formation of the dune, the newly injected high velocity slurry rides on top of the

existing dune and continues to enlarge it. At t =170s, the proppant dune has increased mostly in height (in the Y direction) since the previous observation at t = 140s, while the length/extent of the dune (in the X direction) has not increased significantly. At t = 270 s, the height of the proppant dune shows that it has continued to increase since the previous observation and has approached the top boundary of fracture. The accumulation and packing of the proppants in the vicinity of the inlet (next to the wellbore intersection) is certain to eventually cause a screen-out, which prevents the dune from growing in size.

Fig. 5.5 shows snapshots of particle velocity at the 4 times identified in **Fig. 5.4**. Each particle is color coded by its velocity: a red color represents high velocity with a maximum of 1 m/s, and a blue color represents near-zero velocity. At t = 70s, the majority of the newly injected particles (shown in red) follow the main flow direction (*x*), and sat the same time some begin to settle due to the gravity force. The slurry direction is a combination of gravity and main flow direction (*x*-direction). The previously injected particles formed a thin bed (shown in blue). At t = 140s, the proppant bed height is approaching the height of the fracture inlet. The movement of the slurry (fluid and particles) is influenced by the accumulated bed to approach a near horizontal direction. At t = 170 s, accumulation in the proppant bed continues, thus causing the flowing slurry to move upward. At t = 270 s, the proppant bed almost reaches the top boundary of the fracture. This almost prevents ("chokes") the further transport of the proppants, leading eventually to a limit in the flow path of the proppant particles and causing a screen-out that prevents further proppant entry into the HF.

The fluid and particle velocities at 3 locations (indicated by the dashed lines in Fig. 5.4c) in **Fig. 5.6** allow the study and identification of three distinct flow regimes in the hydraulic fracture. **Fig. 5.6 (a)** shows the velocities of the proppant particle and fluid at x = 1.5 m from the wellbore (close to the inlet) across the whole fracture height. In this region, the velocities of the particles and of the fluids practically coincide. The reason for this behavior is because the fluid drag force dominates, and the counter-effects of the gravitational forces are minimal. This indicates that proppants in this region are in the suspension transport regime, in which particle and fluid are transported as a slurry mixture, and energy dissipation due to inter-particle collision is at a minimum.

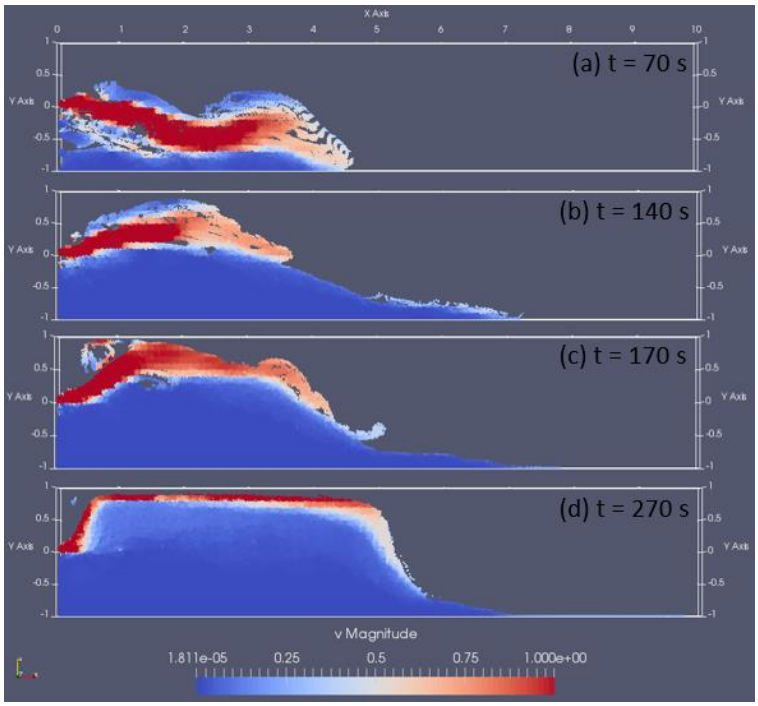

Figure 5.5 Particle velocity field in the vertical hydraulic fracture at an inlet velocity of 5m/s, at (a) t=70s, (b) t=140s, (c) t=170s and (d) t=270s

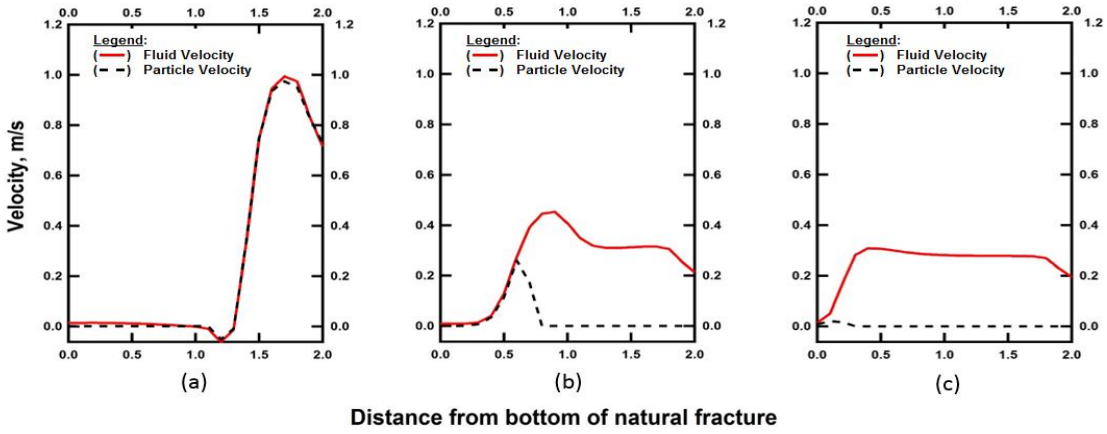

Figure 5.6 Fluid velocity (red) and particle velocity (black dash) at three different distance from the inlet, which are (a) 1.5m, (b) 4.5m, and (c) 6.5m from the wellbore

Fig. 5.6 (b) shows the slick water and the proppant particle velocities on the slope of the proppant dune at x = 4.5 m, and a differentiation of the two velocities begins to evolve. This slope transport regime occurs when both the drag force and the gravitational forces affect the particle velocity. Compared to the velocities in **Fig. 5.6(a)**, the maximum fluid velocity in this region is smaller because the location is farther from the inlet and the suspension transport region has expanded over a larger area and volume, causing the fluid velocity to decrease. The gravitational forces continuously act on the particles, causing them to precipitate, settle and accumulate at the lower parts of the HF, where the velocity rapidly drops to zero (**Fig. 5.6 (b)**). The combined effect of the reduced fluid velocity and the downward movement of the proppant particles caused a separation of particle phase from the fluid phase.

Fig. 5.6 (c) shows that, at x = 6.5 m, the proppants particles are transported (if at all) at a velocity which is much smaller than the fluid velocity. The fluid phase in this region has a near-uniform velocity across the fracture height. This indicates that the proppant phase is further separated from the fluid phase. The flow in this region is in the bedload transport regime, with the proppants already settled at the bottom of the fracture and a clear fluid region flowing on top of the bed region.

The proppant transport efficiency in the bed-load regime is much lower than that in the suspension regime because the majority of the kinetic energy transferred from the fluid to the particles is dissipated through inter-particle collision and particle-wall friction. A comparison of the magnitude of the particle velocities in the three transport stages leads to the conclusion that suspension transport is the dominating transport mechanism in the

hydraulic fractures under the conditions of this study. This conclusion is different from that reached in previous experiments (Medlin et al, 1985, Patankar et al., 2002), in which bed load transport dominated because of low inlet fluid velocities.

I investigated the sensitivity of the system behavior to three important input parameters: the inlet velocity, the coefficient of restitution (**e**) and the friction factor (**μ**). These sensitivity analyses were conducted by simulating Cases V_1-V_7 (Table 5.2). **Fig. 5.7** compares the proppant velocity plots in Cases V_1 (inlet = 5m/s), V_2 (inlet = 2.5m/s) and V_3 (inlet = 10m/s), and demonstrates the effect of the inlet velocity on proppant transport.

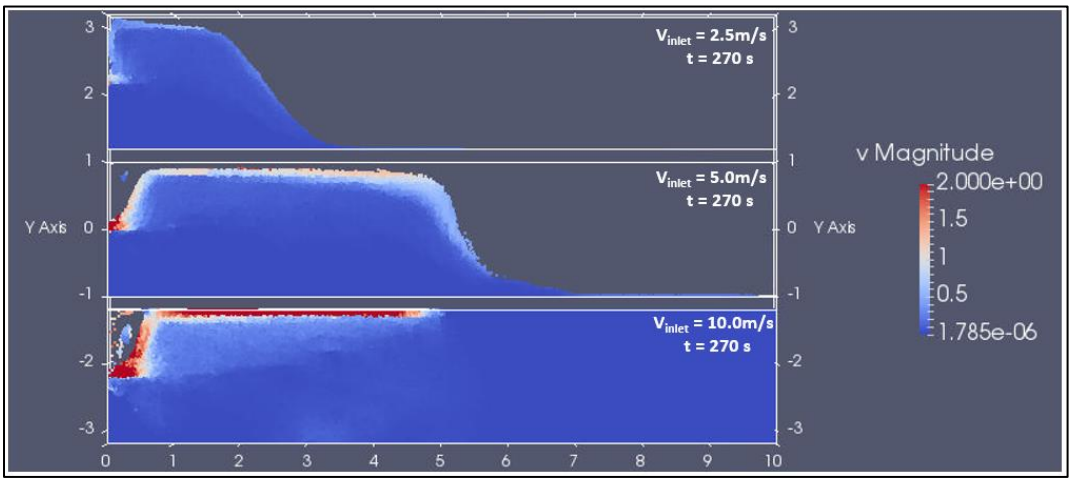

Figure 5.7 Sensitivity test for the inlet velocity using particle velocity plot

Thus, **Fig. 5.7** shows the significant influence of the inlet velocity on the distance over which proppants are transported. In Case V_2 (V_{inlet} = 2.5 m/s), the proppants are not transported far from the wellbore (inlet), but they tend to settle and form a dune near the

inlet, propping only a small part of the hydraulic fracture. The higher V_{inlet} in Case V_1 (5 m/s) causes proppants to be transported farther into the HF, propping open only half of the fracture. V_{inlet} in Case V_3 is the highest of the three cases (10 m/s) and is associated with the highest proppant transport efficiency as proppant particles are transported to the end of our simulation domain (10 meters from the inlet). In Case V_3, the entire length of the HF is propped. The fluid velocity contours corresponding to Cases V_1, V_2 and V_3 in **Fig. 5.8** help explain why proppants are transported farther into the HF as the inlet velocity increases.

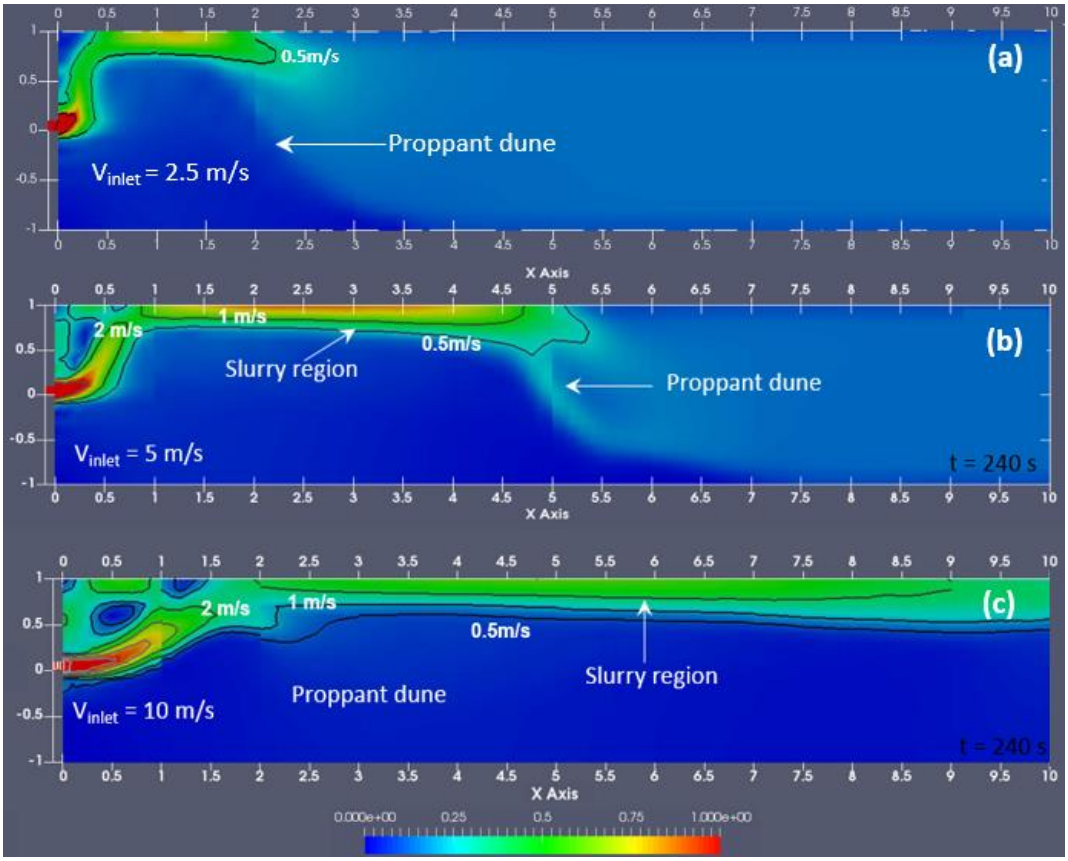

Figure 5.8 Sensitivity test for the inlet velocity using fluid velocity contour plot

Fig. 5.8 (a) shows that for V_{inlet} =2.5 m/s, the contour line for a fluid velocity of V_f = 0.5m/s terminates at a distance of x = 2.2 m from the inlet. Assuming that zero- to low-velocity regions are indicators for the occurrence of immobile or nearly-immobile particles that form the bulk of the proppant dune (bed), this observation leads to the conclusion that the majority of the proppants have also accumulated (settled or precipitated) within the same distance. Note that the V_f = 0.5m/s contour line serves as an estimator of the suspension transport regime/region. In fact, there is no clear cut-off value for the suspension transport region: when the fluid velocity is reduced, there is a wide transition zone in which the flow regime transitions slowly from suspension transport to purely bed load transport.

Fig. 5.8(b) shows that when V_{inlet} =5 m/s, V_f = 0.5m/s contour line and the proppant dune reach x = 5.3 from the inlet. When V_{inlet} = 10 m/s in **Fig. 5.8(c)**, the V_f = 0.5m/s contour line and the proppant dune reach the right-hand boundary (outlet) and in all likelihood extend beyond the right-hand boundary of simulation domain. Comparison of **Figs. 5.8(a), 5.8 (b) and 5.8 (c)** leads to the conclusion that a higher inlet velocity creates a larger suspension transport region, which enables proppants to advance deeper into the fracture (along the x-direction) and results in a larger propped-fracture area. Thus, an obvious way to increase the efficiency and extent of the proppant placement is to increase the inlet velocity and, consequently, the size of the suspension transport region. This can be accomplished by increasing the surface pumping rate or by decreasing the number of clusters per stage.

The sensitivity of the system behavior to the coefficient of restitution (**e**) is investigated in the study of Cases V_1, V_4 and V_5 (**Table 5.2**). **Fig. 5.9** provides a comparison of the proppant velocity plots in Cases V_1 (**μ** = 0.5), V_4 (**μ** = 0.3) and V_5 (**μ** = 0.7).

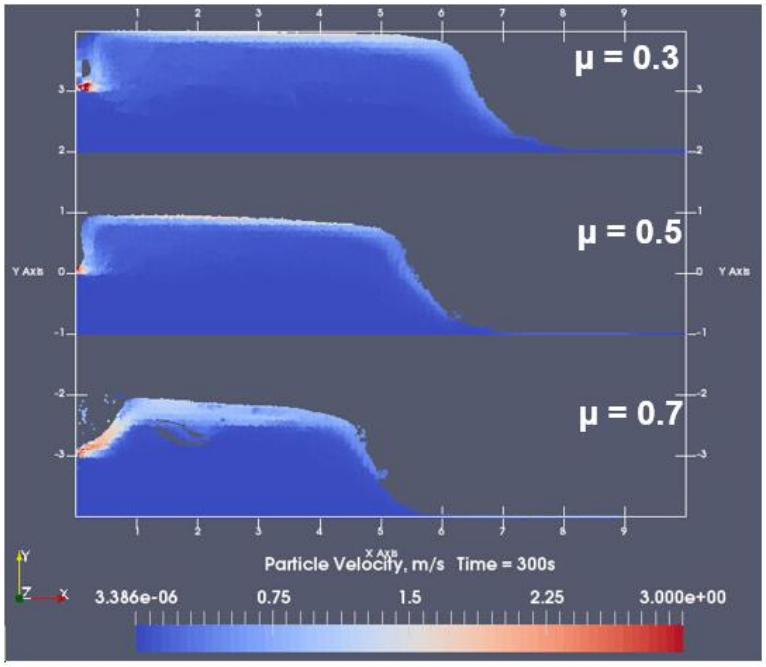

Figure 5.9 Sensitivity test for the friction factor using the vertical fracture model.

Fig. 5.9 shows that the friction factor μ has a significant influence on the proppant transport. A larger μ indicates a rougher fracture wall, which adversely affects the distance over which the proppant particles are transported. I used the median value of μ = 0.5 in all the simulations in the following section. The roughness of fracture walls may vary significantly, as affected by the properties and attributes of the shale and the specifics of the hydraulic fracturing process. Given the dependence of particle transport on the value of μ, reliable estimates of the wall roughness are essential for the design of reliable proppant transport operations, and these can be obtained from calibrated laboratory slot transport tests using representative slabs of the subsurface materials.

I also tested the system sensitivity to the coefficient of restitution (**e**) using the vertical fracture simulations described in Cases V_6 and V_7. **Fig. 5.10** shows a comparison of the particle velocities in Cases V_1 (**e = 0.4**), V_6 (**e = 0.2**) and V_7 (**e = 0.6**).

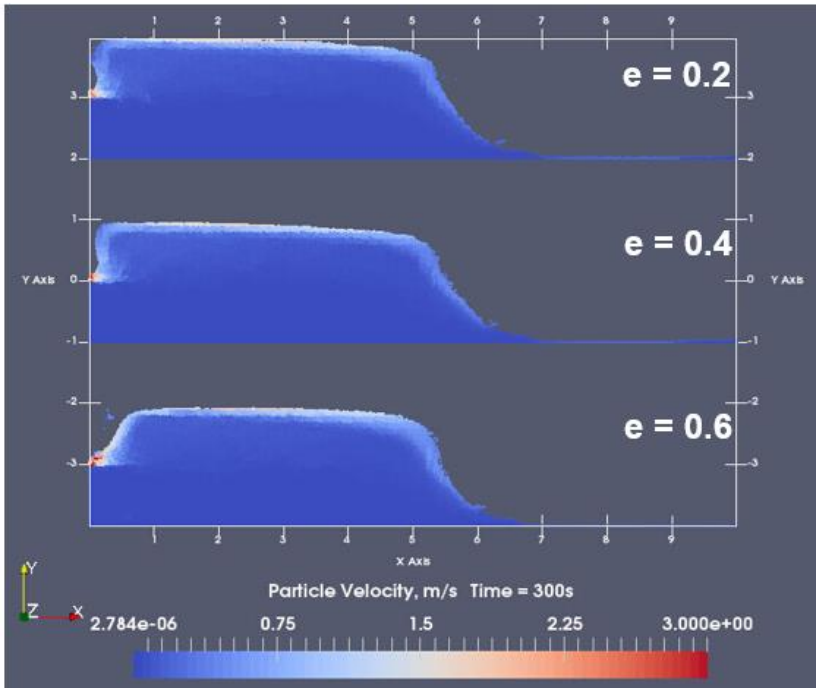

Figure 5.10 Sensitivity test for coefficient of restitution using the vertical fracture model.

Fig. 5.10 shows the limited impact of the coefficient of restitution (***e***) on the distance of proppant transport in the vertical hydraulic fracture. The only noticeable difference between the three cases is in the vicinity of the inlet. A larger ***e*** value is associated with a milder slope of the dune. This is because a larger **e** value leads to the conservation of more

energy during the collision. Consequently, proppants near the inlet have larger kinetic energy after collision with the dune, and are thus less likely to accumulate on the dune.

5.4. Simulation Domain and System Conditions in the Study of Dipping Fractures

As discussed in **Section 5.1**, the majority of in-situ hydraulic fractures are not perfectly vertical. To study the dependence of the proppant transport efficiency on the dipping angle, I conducted proppant transport simulations using the 3 HF domains with dipping angles of 75°, 60°, and 45° that were discussed in **Section 5.1**. The schematics in **Fig. 5.11** illustrate the vertical and dipping fractures I investigated in this study. The length and aperture of the dipping HFs are the same as in the vertical fracture case (shown in **Table 5.1**). The apparent height of each dipping fracture is the same (l =2 m) as in the vertical fracture, thus maintaining the same cross-sectional area, and the same level of fluid flux into the fracture. **Fig. 5.12** shows a 3D view of the meshing for the dipping fracture domains.

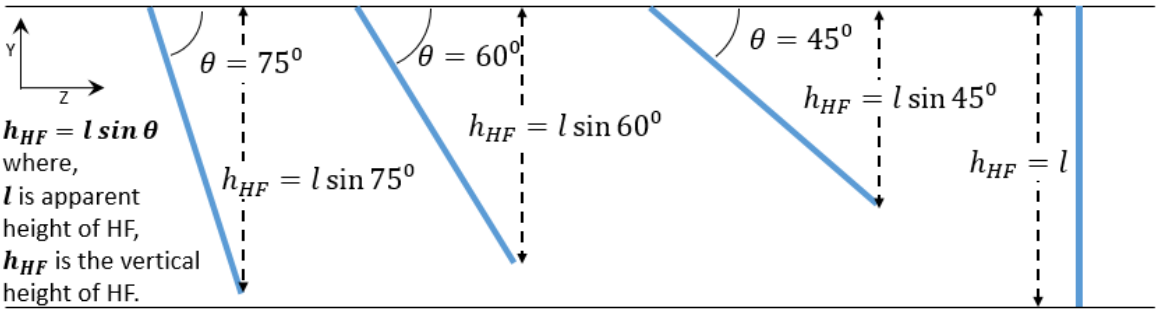

Figure 5.11 Schematic illustration of apparent height and vertical height of dipping fractures

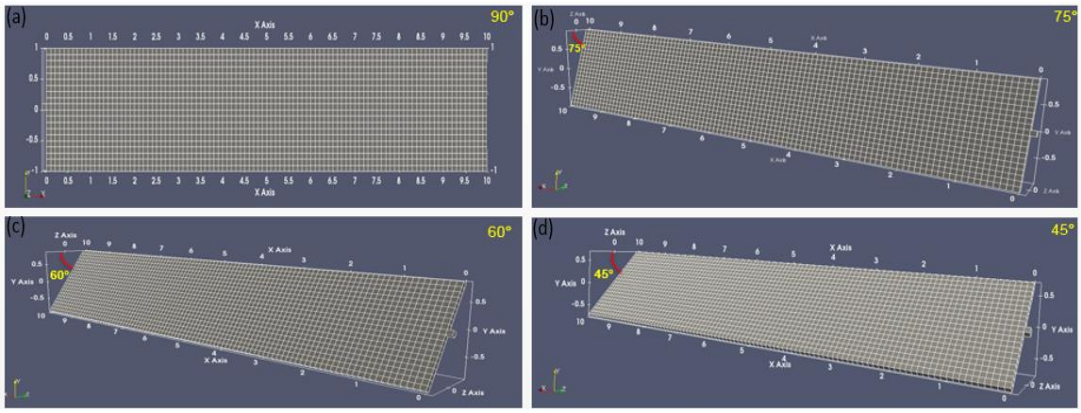

Figure 5.12 3D view of vertical and dipping hydraulic fracture domains: (a) mesh for vertical fracture, (b) mesh for 75° dipping fracture, (c) mesh for 60° dipping fracture and (d) mesh for 45° dipping fracture

A proppant with a uniform particle diameter of 0.425 mm (30/60 mesh) is injected in a slick water-based fluid into the three dipping hydraulic fractures at an inlet fluid velocity of 5 m/s. In all dipping-angle cases, the simulations use a friction factor $\boldsymbol{\mu}$ = to 0.5 and a coefficient of restitution $\boldsymbol{e}$ = 0.4. In fact, with the exception of the dipping angles of the domain, all properties and conditions in these simulations are the same as in the vertical HF case (**Table 5.1**). For easier future reference, we name the dipping fracture cases as follows: Case D_1 with a 90ºdipping angle (vertical fracture, coinciding with Case V_1), Case D_2 with a 75ºdipping angle, Case D_3 with a 60º dipping angle and Case D_4 with a 45ºdipping angle.

5.5. Simulation of Proppant Transport in Dipping Hydraulic Fractures

Fig. 5.13 shows the fluid velocity contours in the four dipping angle cases (45º to 90º). These contour plots correspond to the times when screen-out occurs. A screen-out occurs

when the proppant particles that accumulate in the vicinity of the fluid inlet are packed so solidly in the entire height of the HF that they prevent further slurry injection and flow into the HF.

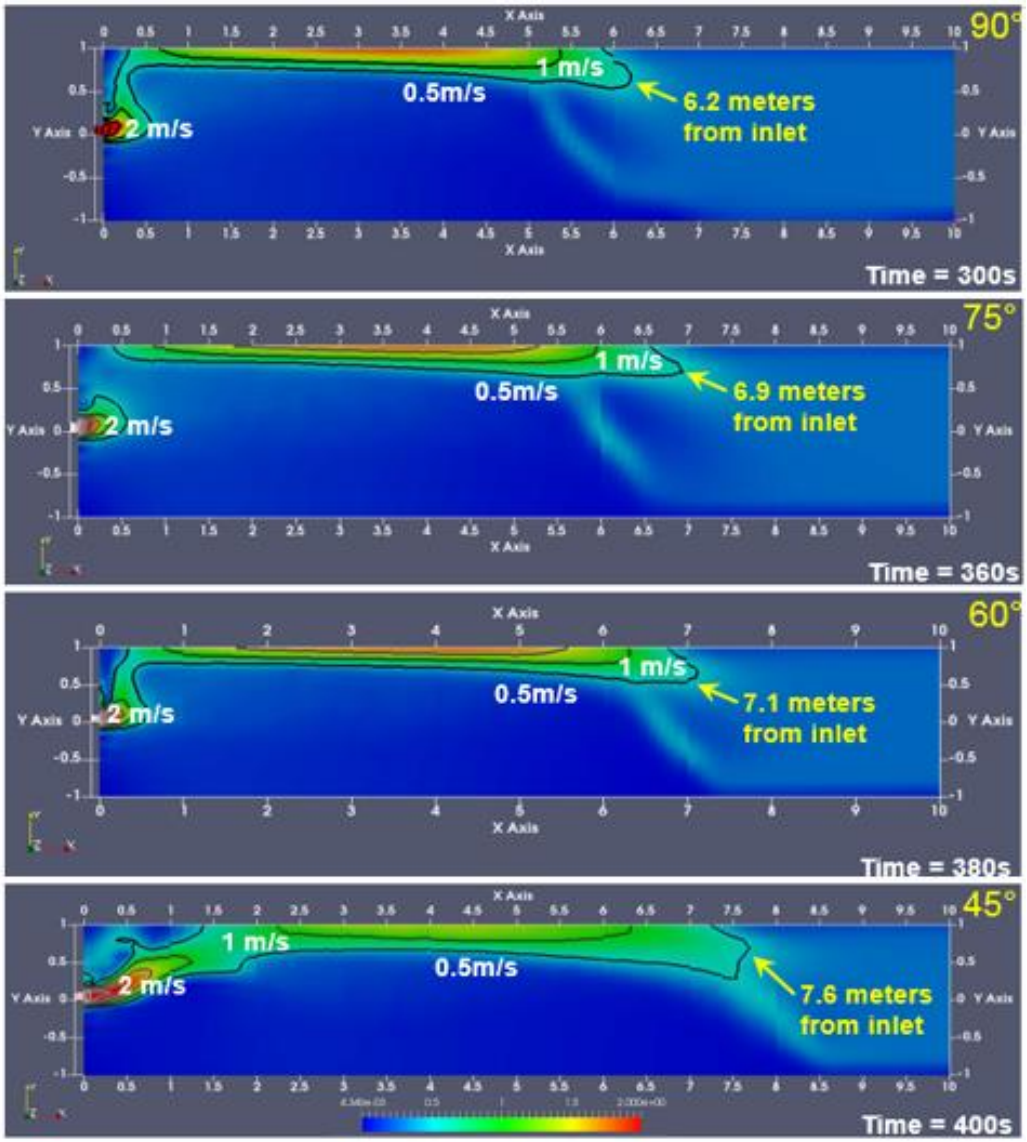

Figure 5.13 Plot of (a) X-Y plane view of fluid velocity contour in vertical and dipping fractures

Thus, the particle injection rate into the simulation system decreases dramatically (to almost zero) at screen-out. In my simulations, I continuously monitored the number of total particles in the system, and determined the occurrence of screen-out by the stabilization of the particle number in the system, at which point I terminated the computations. Review of the velocity contour plots at screen-out shown in **Fig. 5.13** reveals that the suspension transport region (delineated by the V_f = 0.5 m/s contour line) reaches further away from the inlet (from 6.2 m to 7.6 m) into the fracture as the dipping angle decreases from 90^0 to 45^0.

Fig. 5.14 shows the particle velocity and reach into the HF in Cases D_1 to D_4 at screen-out, and correspond to the fluid velocity contour plots in **Fig. 5.13**. The color of the particle represents its velocity. In the vertical fracture case (dipping 90^0), the proppant dune reached 5.2 m from the wellbore. Here we define the proppant reach as the distance from the inlet to the point where most of the height is practically fully packed, coinciding with the point where the forward slope of the dune increases (in an absolute sense) drastically.

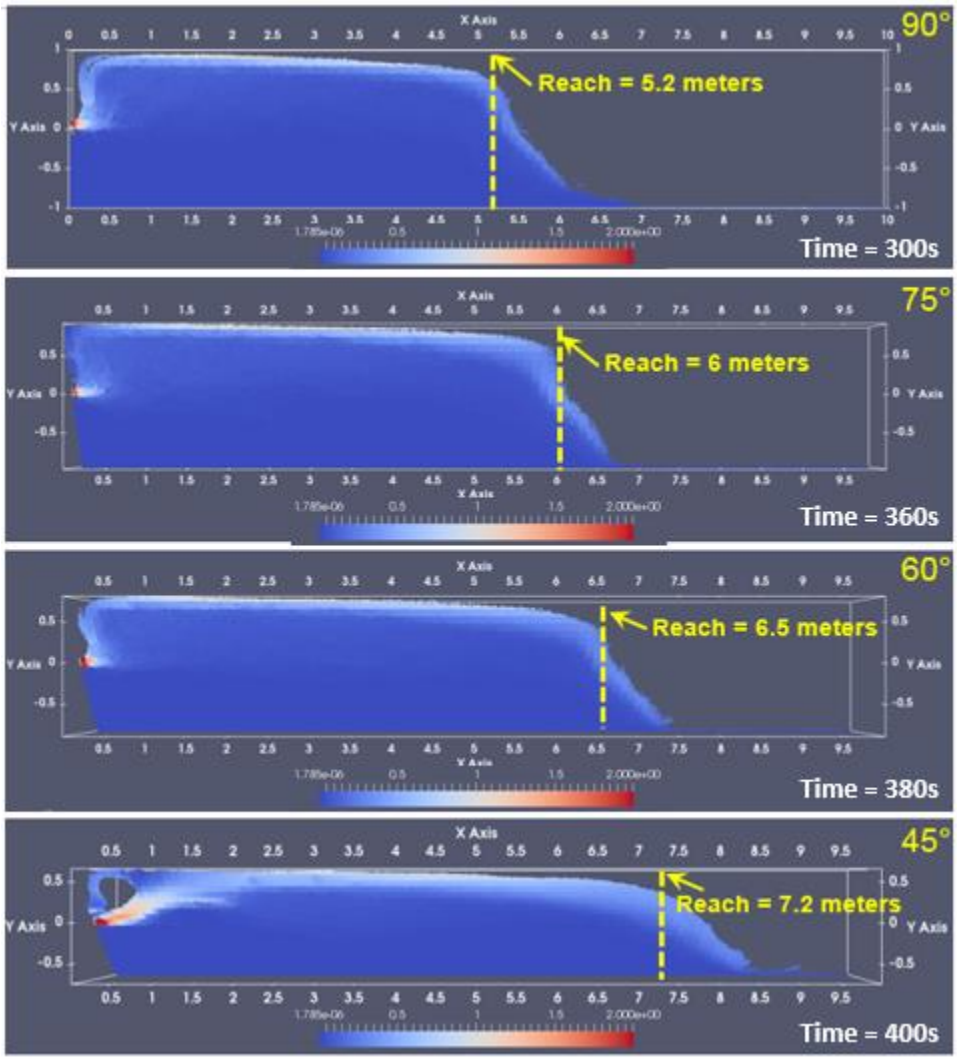

Figure 5.14. 3D view of particle velocity and location in vertical and dipping fractures

When the fracture dipping angle declines from 90^0 to 75°, 60°, and 45°, the proppant reach increases to 6 m, 6.5 m and 7.2 m, respectively. My simulations demonstrated a strong relationship between the dipping angle of the fracture and the reach of the proppant dune.

When the dipping angle decreases, the proppant reach increases, which means an improvement in the proppant placement efficiency.

We use the proppant reach and the proppant mass to quantify the level of the proppant placement improvement. The proppant mass is calculated by knowing the individual particle mass and counting the number of the proppant particles in the fracture at the time of screen-out. **Fig. 5.15** shows the relationship between the fracture dipping angle and the % improvement in proppant placement/efficiency, which increases monotonically (a) by 38.5% in the proppant reach and (b) by 33.1% in the proppant mass as the dipping angle decreases from 0^o in the reference case (D_1) to 90^o angle in Case D_4 of the 45° dipping angle.

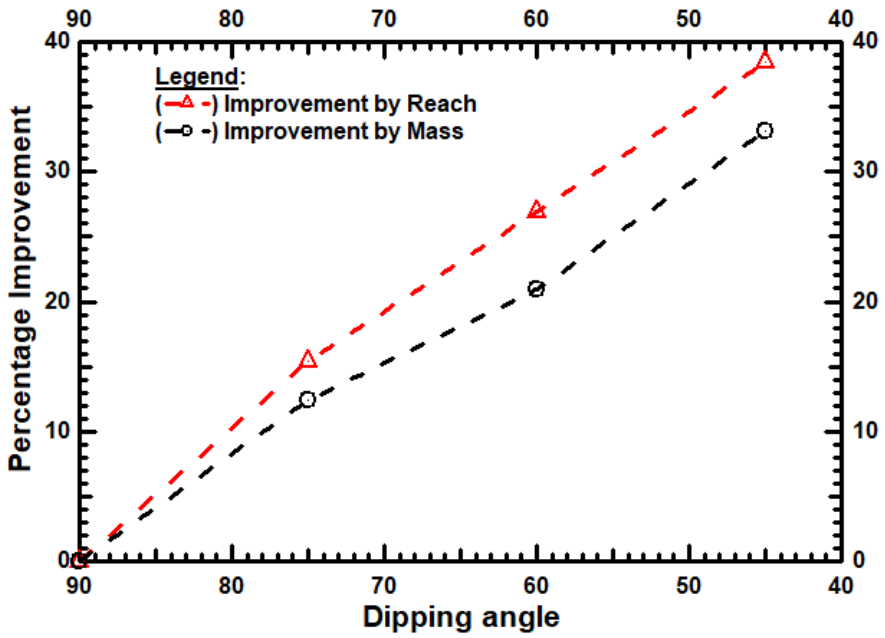

Figure 5.15 Percentage improvements by reach and mass of proppant in the dipping fractures

To understand the causes for the improvement in the proppant reach placement (and, consequently, efficacy) as the deviation from the vertical increases, I compared the vertical and horizontal components of the particle velocity in Cases D_1 to D_4. **Fig. 5.16** shows the dependence of the vertical component of the particle velocity on the distance from the base of the fracture at x= 0.9 m and t = 40 s. The negative value of the vertical velocity indicates a settling motion of the particles at this location (corresponding to **Fig. 5.5a**). As the dipping angle decreases from 90º to 45º, a clear trend of decreasing settling velocity becomes evident, with the maximum settling velocity reduced from -0.93 m/s to -0.73 m/s.

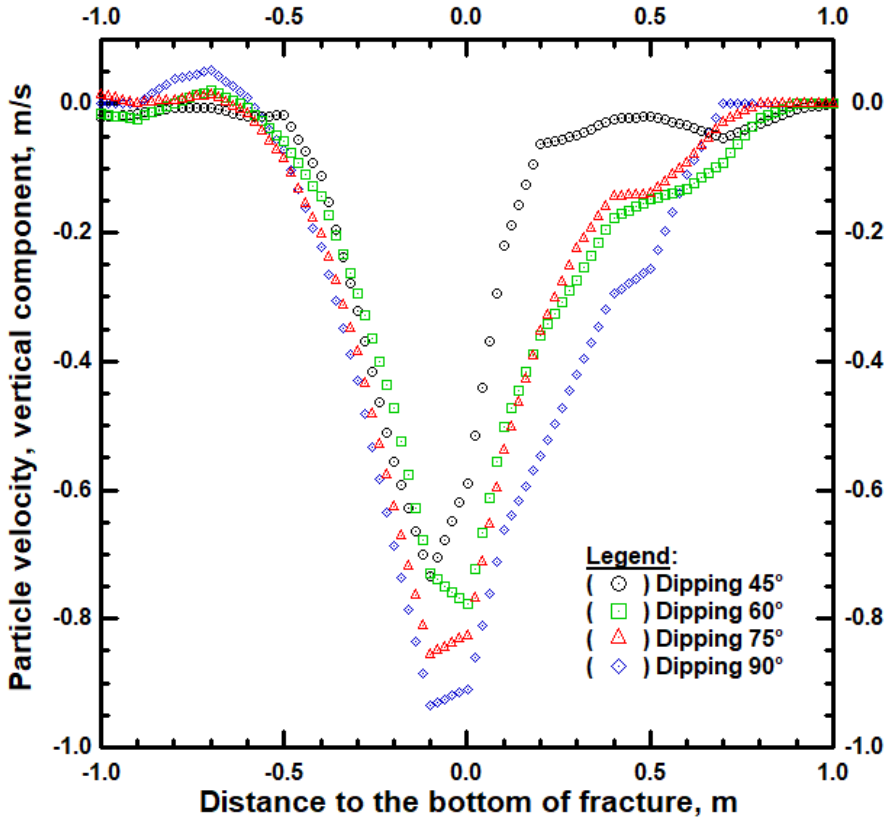

Figure 5.16 Vertical component of proppant velocity as a function of the distance from the base of the fracture and the dipping angle, measured at x=0.9m, t=40s

I attribute this decreasing trend in the settling velocity to the contact force of the fracture sidewall acting on the particles. Since the vertical component of the contact force is in the opposite direction to the gravity force, it cancels partly the gravity force and results in a lighter apparent particle weight, thus facilitating further proppant transport. **Fig. 5.17** illustrates the direction of gravity force and of the contact force during the downward (settling) and upward (lifting) motion of particles in dipping fractures.

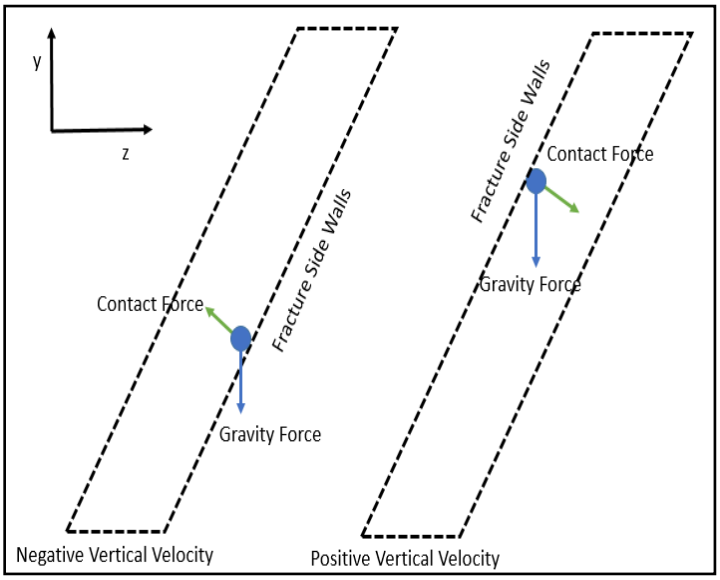

Figure 5.17 Schematic illustration of contact force and gravity force on proppant particle during downward and upward motion in the fracture

Similarly, **Fig. 5.18** shows the dependence of the horizontal component of the particle velocity on the distance from the base of the fracture, measured at x = 0.9 m and t = 250s. The positive value of the horizontal velocity indicates that the proppant particles are transported on top of the existing dune deeper into the fracture. The increase in the maximum horizontal velocity (a) increases with a decreasing dipping angle and (b) is large in magnitude, reaching a level that is double that for 90^o when the dipping angle is reduced to 45^o.

The enhanced horizontal component of the particle velocity can explain the increased proppant reach that is evident in **Fig. 5.18**. This enhancement in the particle velocity is attributed to the same cause explained above: because of the contact force of the fracture sidewall exerted upon the particles, the apparent weight of proppants in dipping fractures

diminishes. For the same fluid drag force, proppants in dipping fracture move faster (and farther) than in a vertical HF.

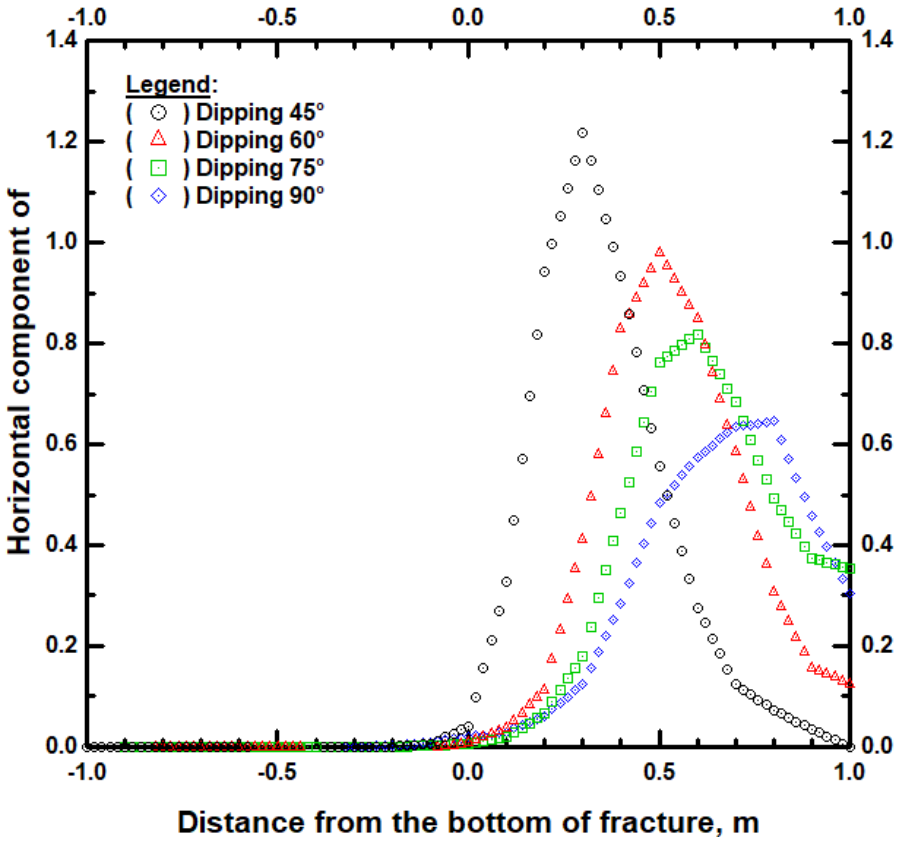

Figure 5.18 Horizontal component of the proppant velocity as a function of the distance from the base of the fracture and the dipping angle, measured at x=0.9m, t=250s

Fig. 5.18 also shows a distinct shift in the location where the maximum horizontal velocity is attained. This is because the horizontal velocity was measured along the vertical axis at x = 0.9 m, which is relatively close to the fluid inlet. At t = 250 s, the proppant dune has already reached a significant size at this location. The freshly injected slurry rides on top

of the existing slope and is transported farther into the fracture. The shift in the location of the peak velocity (towards zero, which is the height of inlet) indicates that the dune slope decreases in the dipping fractures.

The reduced dune height is more evidence of the enhanced mobility of the proppants (and longer reach) in dipping fractures. **Fig. 5.19** shows explicitly the relationship between the dipping angle and the height of the sand dune height near the inlet (0.9m from the horizontal wellbore). As the dipping angle decreases from 90º to 45º, the sand dune height decreases because more particles are mobile. This provides additional support to my argument that proppants in dipping fractures are more mobile, which reduces the risk of proppants blocking the flow path of the slurry and enables longer reaches deeper into the fractures.

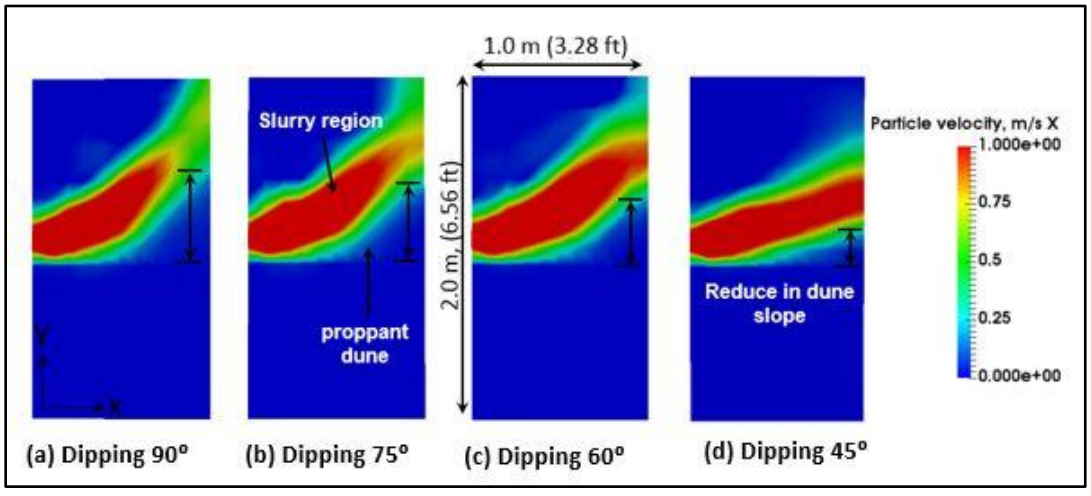

Figure 5.19 Reduced dune slope near the inlet caused by dipping angle of fracture, measured at x=0.9m, t=250 s

5.6. Flow and Transport in Vertical and Dipping Fractures: Some General Observations

To summarize the observations and conclusions from the dipping fracture simulations: proppant particles settle slower in dipping fractures. This is caused by the contact with, and the consequent friction force that is exerted by, the fracture walls. Because of the resulting longer settling period, proppant particles are mobilized by the fluid drag force and attain a higher velocity. Thus, the size of the corresponding suspension transport regions increases in a manner inversely proportional to the angle of the dipping fractures.

One of the most significant consequences is that the proppant particles are transported farther from the inlet and deeper into the HF, thus effecting better proppant placement and a longer reach into the fractures. Additionally, because proppants in dipping fractures are easier mobilized by the carrier fluid (slick water), they have a weaker tendency to block the flow path near the wellbore. The numerical simulation results also show that the dune height is lower in dipping fractures. This helps enlarge the suspension transport region and promotes better proppant placement efficiency.

6. PROPPANT TRANSPORT THROUGH COMPLEX, SHARPLY ANGLED INTERSECTING FRACTURES: T-INTERSECTIONS

In this section I investigate numerically the transport of proppants at different types of intersection of hydraulic fractures (HF) and natural fractures (NF). In **Section 6.1** I describe two complex intersecting HF-NF scenarios, namely a T- and a Z-intersection (to be defined later). **Section 6.2** presents the detailed model used for the study of a T-shape intersection, and provides a general description of T-shape intersection cases I investigated. **Section 6.3** presents the simulation results and comparisons of the T-intersection cases.

6.1. The Complexity of the Subsurface HF-NF Network

A challenging area in the study of proppant transport is the prediction of proppant placement in the intersecting hydraulic fracture-natural fracture (HF-NF) network. This is because of the complex geometry of the flow system and the even more complex physics involved in the associated proppant transport process. Existing proppant transport models generally assume a single HF with a simple vertical planar geometry. Such a simplification helps reduce the dimensionality of the problem and eliminates the need to consider the interaction between the proppant particles and the fracture walls at the junction of intersecting fractures. However, the subsurface reality is more complex than what such a simple model can describe (Tang et al., 2018, 2019, Zhang et al., 2018, 2019). A combination of depositional, geodynamic, and tectonic processes often results in very heterogeneous and anisotropic formations, with NFs of varying attributes distributed within their boundaries.

During the process of hydraulic fracturing, the propagating HF is generally assumed to intersect and connect with existing NF networks. Gu et al. (2012) summarized the possible scenarios of HFs interacting with preexisting NFs. **Fig. 6.1** illustrates two possible scenarios, both involving a NF connecting two HFs.

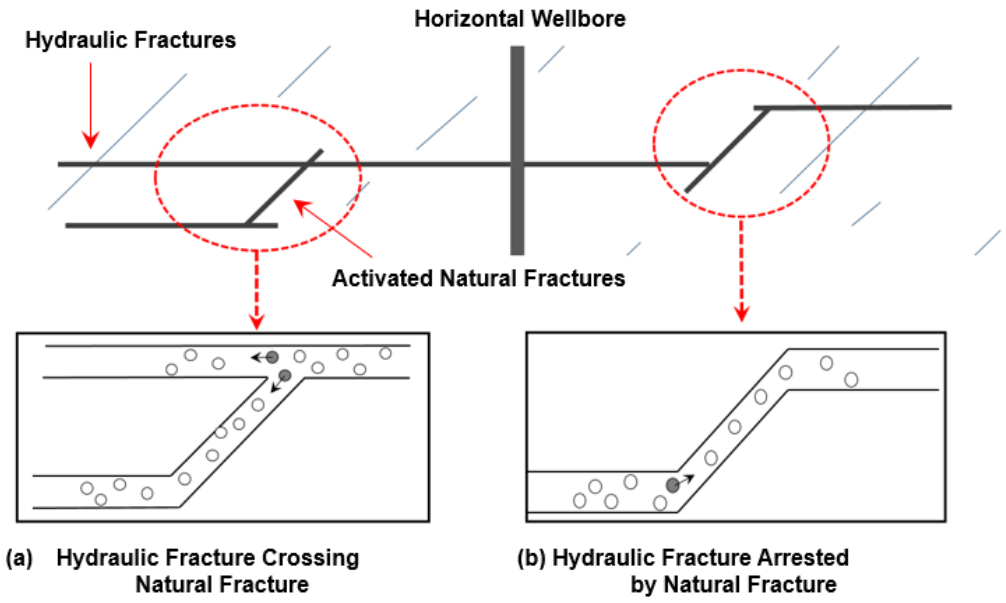

Figure 6.1 Two possible scenarios of the HF interacting with NF: (a) HF crossing and activating NF (T-intersection) and (b) HF arrested by the NF (Z-intersection)

In the 1st scenario, a HF encounters a NF and at the intersection the fracturing fluid and the proppants are split into two streams: one in the continuing HF and another entering and activating the NF, which is connected at its end with another HF or NF (**Fig. 6.1a**). In the 2nd scenario, the HF-NF intersection occurs at or near the termination of the HF, and the entire fluid and proppant stream in redirected into the NF toward the second HF;

in other words, the NF arrests the propagation of the HF (**Fig. 6.1b**). The first type of HF-NF junction is called a T-intersection, although the T may be stretched; the second type of HF-NF junction is called a Z-intersection, although the Z is inverted and can also be quite stretched.

The 3-dimensional geometries of the HF-NF network often involve multiple planar sections connected at sharp angles. Flow around these sharp angular features usually involves changes in the direction of flow and strong interactions between the proppant particles and the fracture walls. These features are expected to cause significant settlement of the proppants, and there is considerable uncertainty about the amount of the proppants that can enter the secondary NF. Most available models are limited in the dimensionality of the problems they can address (they are limited to 2D at best), and cannot adequately predict the distribution of proppant in such complex fracture geometries.

In the scenario of a T-intersection (**Fig. 6.1a**), the fluid and the proppants at the HF-NF junction will be distributed between the original HF and the activated NF. It is generally unknown what fraction of the proppant will be able to enter the NF. A simple assumption (made for the convenience of the researcher rather than in an effort to represent reality) would be to make the percentage of proppant mass entering the NF equal to the percentage of the fluid mass entering the NF. Such percentages are unknown a-priori, as they (logically) appear to depend on a number of factors (*e.g.*, apertures of the HF and NF fractures, angle of the intersection, proppant size, carrier fluid properties, etc.).

Introduction of such an approach in the computations of a numerical simulator would limit the involve (a) limiting the physics to an analysis of only the liquid part of the injected

stream and (b) ignoring completely the vastly different behavior of the particles, thus leading to unavoidably erroneous results. The same considerations apply to the study of transport at a Z-intersection (**Fig. 6.1b**), but with the simplification that the entire stream of slick water and proppants is diverted into the NF. In that case the entirety of the liquid will flow from the HF into the NF, but this is unlikely to be the case in the transport of proppants, as the latter are affected by the same factors listed above.

6.2. Simulation Domain and System Conditions in T-Intersection Studies

The simulation domain in the study of a T-intersection is expanded from its simpler single planar fracture in Section 4 to the more complex HF-NF system shown in **Fig. 6.2**. The domain consists of four sections: three sections corresponding to hydraulic fractures, and one section corresponding to a natural fracture. The natural fracture intersects the hydraulic fracture at a 45º angle at a distance of 2.5m from the wellbore. The activated natural fracture begins and ends at the two (parallel in **Fig. 6.2**) HFs. The original hydraulic fracture continues past its intersection with the NF.

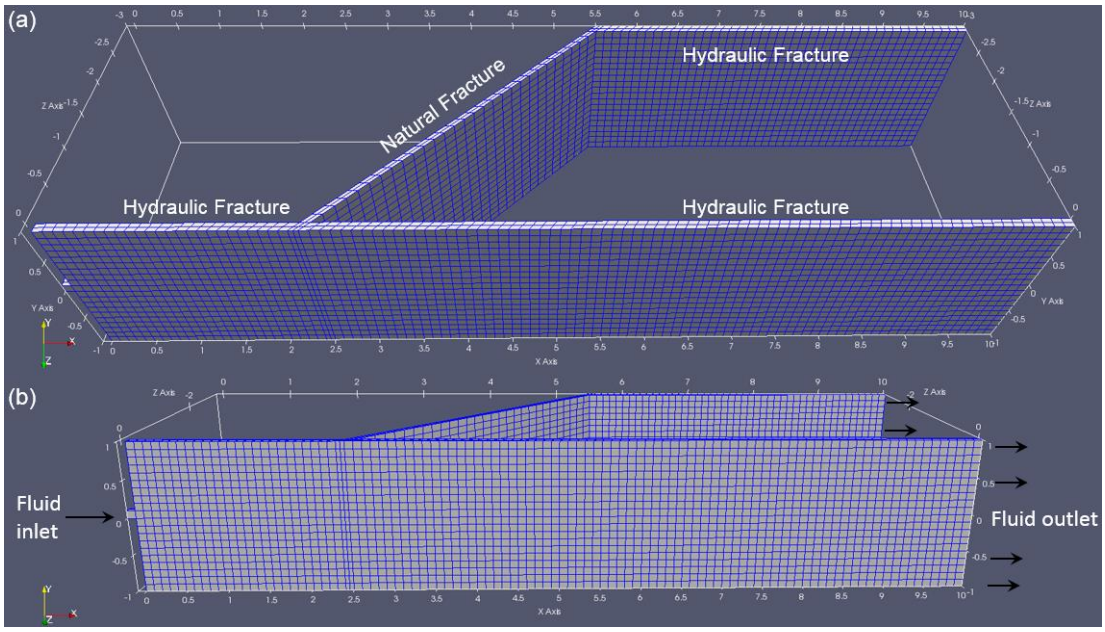

Figure 6.2 Visualization of the mesh for the T-shape intersection: (a) top view of the NF-HF intersection and (b) side view and boundary condition of the HF-NF intersection

The parameters of the domain for the T-intersection studies are shown in **Table 6.1**. The HF simulation domain is discretized into a CFD mesh with a uniform element size (with dimensions of 0.1m×0.1m×0.005m), and the NF simulation domain is also discretized into a mesh with a uniform element size (with dimensions of 0.1m×0.1m×0.0035m). Note that the aperture of the natural fracture is assumed to be 0.7 times that of the hydraulic fracture. The inlet and outlet conditions for the various cases of these studies are specified in **Section 6.3**.

Table 6.1 Parameters for the T-intersection fracture simulation domain

Parameters	SI Units	Field Units
Height, $\boldsymbol{h_f}$	2 m	6.56 ft
HF_1 Length, $\boldsymbol{x_{hf1}}$	10 m	32.8 ft
HF_2 Length, $\boldsymbol{x_{hf2}}$	4.5 m	14.7 ft
NF Length, $\boldsymbol{x_{nf}}$	4.4 m	14.4
HF Aperture, $\boldsymbol{w_{hf}}$	0.01 m	0.4 inch
NF Aperture, $\boldsymbol{w_{nf}}$	0.007 m	0.28 inch

6.3. Cases of T-Intersection Studies

I investigated multiple simulation cases in order to estimate the amount of proppant particles that entered the NF at various injection rates. **Table 6.2** lists the investigated cases, and their corresponding inlet velocities. Note that the boundary conditions of the two fractures outlets are set at "no reflectance outlet". I believe this is a boundary condition suitable for the far-field (away from wellbore) boundaries, because the out-going fluid is allowed to exit the domain without being reflected back to the fracture domain. The inlet velocity (ranging from 1 to 10 m/s) represents the fast "jetting" region where fluid and proppants enter the fracture through the casing perforations. As shown in **Section 5.2**, an inlet velocity V_{inlet} = 5m/s corresponds to a surface pumping rate of 35 bpm, and a V_{inlet} = 10m/s corresponds to a surface pumping rate of 70 bpm.

Table 6.2 Parameters for the T-intersection fracture simulation domain

Case Number	Inlet Velocity, m/s
T_1	5.0
T_2	2.5
T_3	3.0
T_4	3.5
T_5	4.0
T_6	4.5
T_7	2.0
T_8	5.5
T_9	6.0
T_{10}	6.5
T_{11}	7.0

6.4. Simulation of Proppant Transport at T-Intersection

Case T_1 (with V_{inlet} = 5m/s) is the reference case in the study of fluid flow and particle transport in T-shaped intersection systems. **Fig. 6.3(a)** shows the fluid velocity field in both the HF and NF components of the simualtion domain at time t = 250s. The white dashed line shown in **Fig. 6.3(b)** marks the location where the HF intersects the NF, which is 2.5m from the inlet. The different colors represent the magnitude of fluid velocity. Note that Fig. 5.3(a) is inverted from the domain shown in Fig. 5.2 — *i.e.*, that domain is viewed from the opposite direction: the original HF that continues past the intersection with the

NF — which was in the front in Fig. 5.2 – is now in the back and the inlet is at the midpoint of the right boundary of the domain.

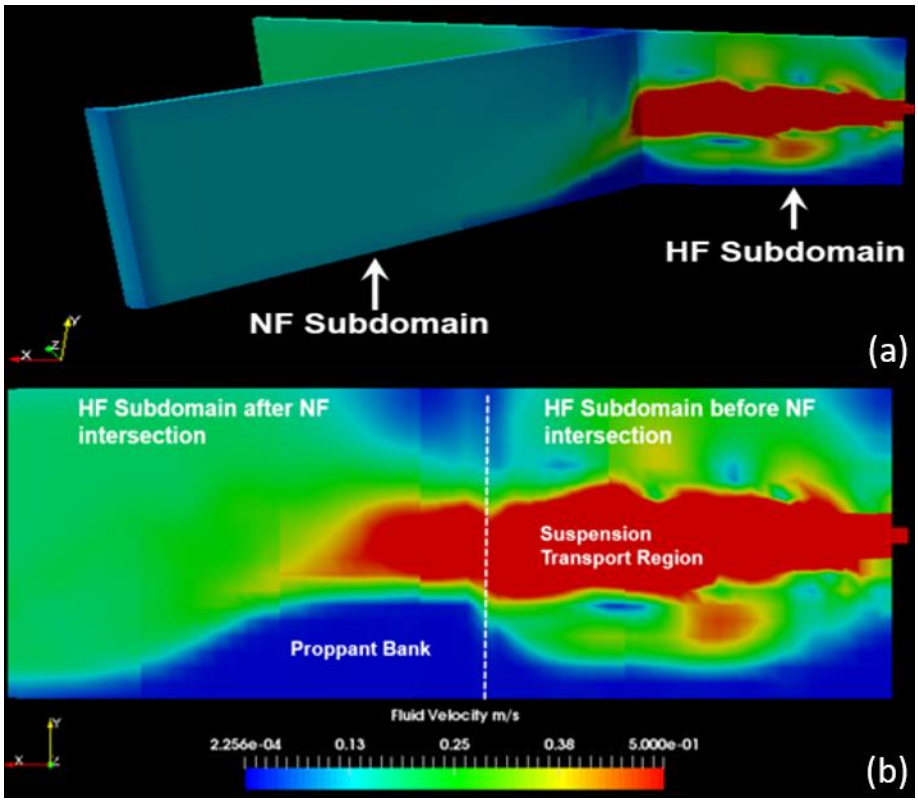

Figure 6.3 - Case T1 (inlet velocity = 5m/s):Visualization of (a) the 3D fluid velocity field in the HF and NF subdomains and (b) the 2D fluid velocity field in the original HF (t=250s)

For the reasons discussed in an Section 4.3, it is easy to identify the suspension transport region (shown in red) and a proppant bank region (shown in blue) in the original HF subdomain by assuming that the fluid velocity regimes are a reliable indicator of the occurrence of proppants (mobile and immobile). At the HF-NF intersection, a portion

(rather small, judging from the color variations in Fig. **6.3(a)**) of the suspension slurry is diverted into the NF subdomain.

Therefore, the size of suspension transport region is limited compared to that in the HF subdomain, and the height of the proppant bank in the NF decreases in the direction of flow. The peak proppant bank height in the NF subdomain is at the HF-NF junction. On the other hand, the maximum bank height in the original HF is observed a short distance after the HF-NF intersection.

The particle velocity plot in Case T_1 is shown in **Fig. 6.4**. The color of a proppant particle denotes its velocity. The blue area indicates accumulation of proppants with near-zero velocity, *i.e.*, these are proppants settled into immobile bed. The red area represents proppants with a velocity of at least 0.1m/s. These proppants could be transported in either in a bedload or a suspension regime.

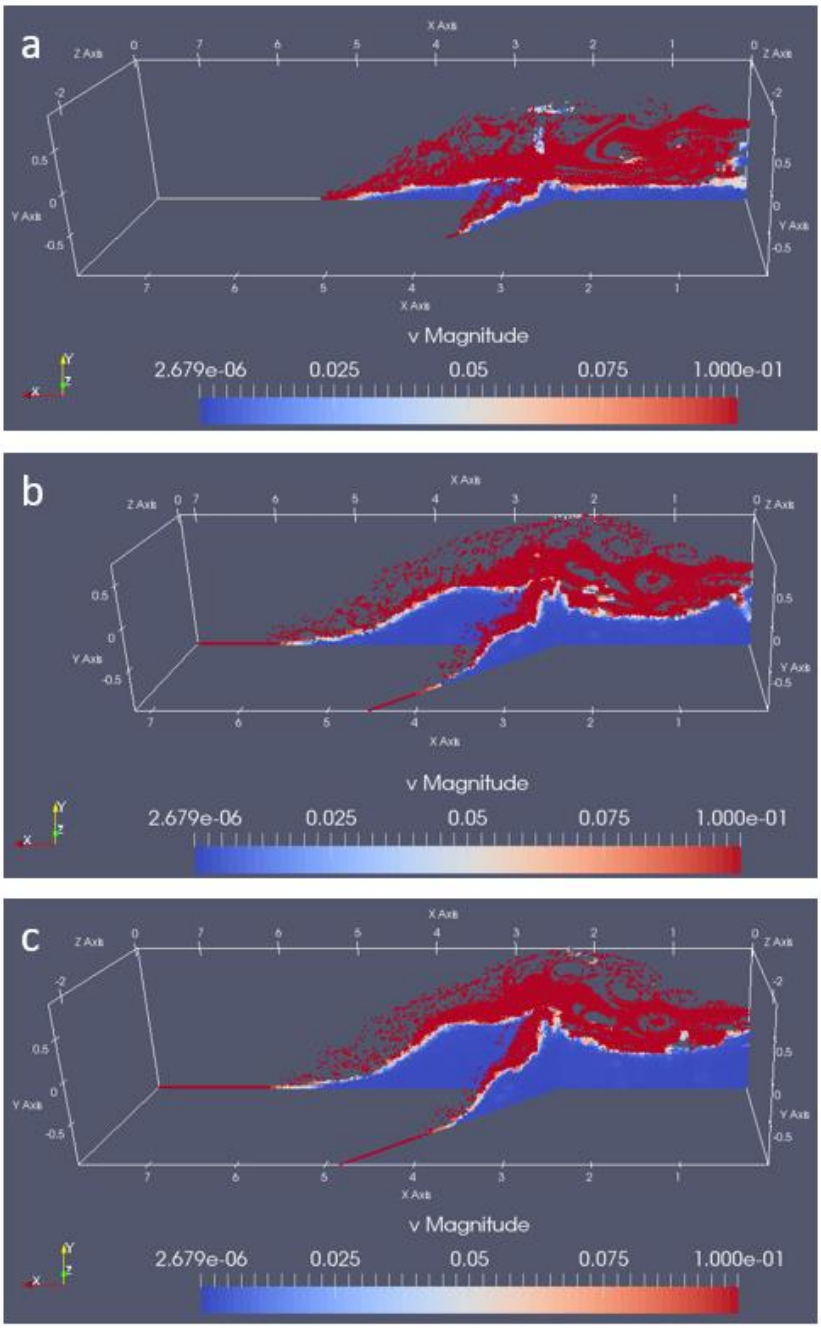

Figure 6.4 - Case T_1 (inlet velocity = 5m/s): Visualization of particle velocity and location for the case of inlet velocity of 5.0m/s at (a) t=100s, (b) t=200s and (c) t=250s

To determine the regime of the proppant particles at the T-intersection, I sampled the fluid and particle velocity profiles at three different locations: (a) at a distance of 0.2 m before the HF-NF intersection in the HF subdomain, (b) 0.2 m after the HF-NF intersection in the HF subdomain, and (c) at 0.2 m after the HF-NF intersection in the NF subdomain.

Fig. 6.5 shows the spatial distribution of the fluid and particle velocities in the subdomain profiles at each location and provides a measure of the flow and transport mechanisms in each subdomain. In all three plots, the particle velocity profile is close to the fluid velocity profile, indicating that suspension transport is the dominant flow regime at the sampled locations. Comparison of the fluid velocity profiles before (**Fig. 6.5 a**) and after (**Fig. 6.5 b**) the HF-NF intersection shows that the fluid and the velocities drop significantly in the HF past the HF-NF intersection.

Integration of the fluid velocity across the vertical length leads to an estimate of the percentage of the fluid entering the NF subdomain ($F_{F,NF}$) as 30.3 % of the flow inflow at the inlet. A dominant factor controlling the $F_{F,NF}$ is the ratio of the NF and HF apertures. Remember that the NF aperture is 0.7 times that of the HF aperture in this study. Further reduction of the aperture ratio is certain to decrease the $F_{F,NF}$ value.

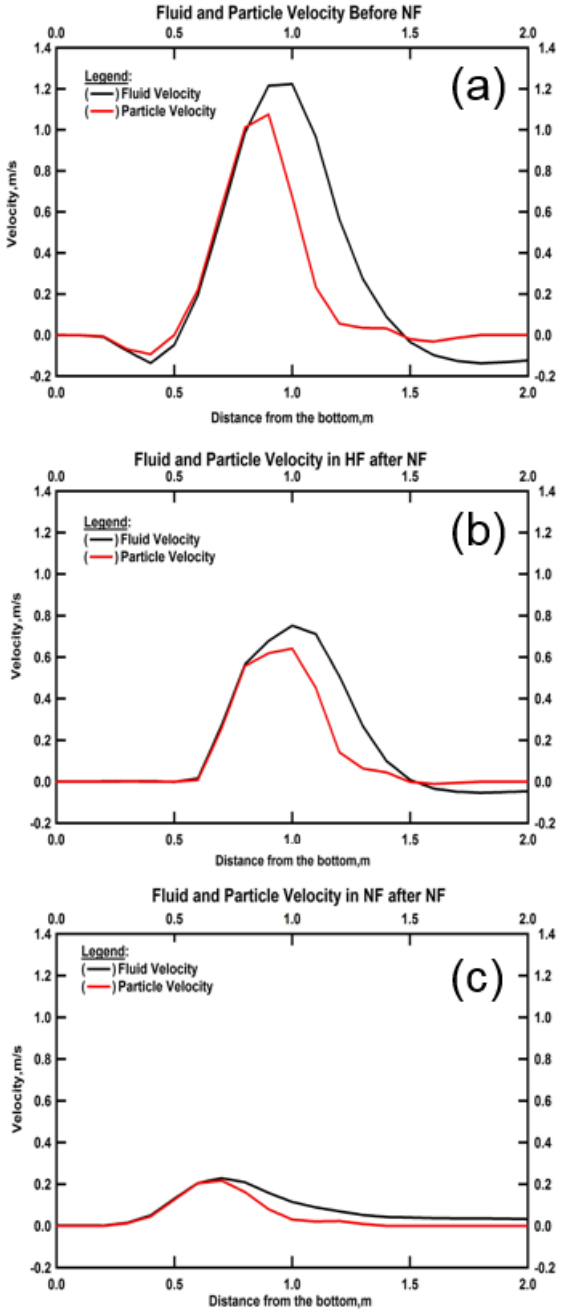

Figure 6.5 Fluid and particle velocities in Case 1 at three locations at t = 250 s: (a) 0.2m before the intersection in the HF domain, (b) 0.2m after the intersection in the HF domain and (c) 0.2m after the intersection in the NF domain

I also estimated the fraction of the proppant particles entering the NF subdomain ($F_{P,NF}$) by (a) tracking the location of each particle in all subdomains of the simulated system, (b) counting their respective numbers at 20-sec intervals and (c) by concentrating on the particle numbers in the NF. Thys, $F_{P,NF}$ is determined by the following step-by-step process:

(1) Record the total number of particles in the system at time *t*, which is $N_{t,total}$

(2) Count the number of particles in the NF at time *t*, $N_{t,NF}$.

(3) Record the total number of proppant particles in the system at time *t+5 s*, $N_{t+5,total}$

(4) Count the number of particles in the NF at time *t+5s*, $N_{t+5,NF}$.

(5) During the 5s time period, the percentage of proppant particles entering the NF subdomain is : $F_{P,NF} = (N_{t+5,NF} - N_{t,NF}) / (N_{t+5,total} - N_{t,total}) \times 100\%$

Fig. 6.6 shows estimates of the $F_{P,NF}$ fraction (estimated at 5s time intervals), which appear to be roughly constant at $F_{P,NF}$ = 12%-14% of the total number of particles during the duration of the study.

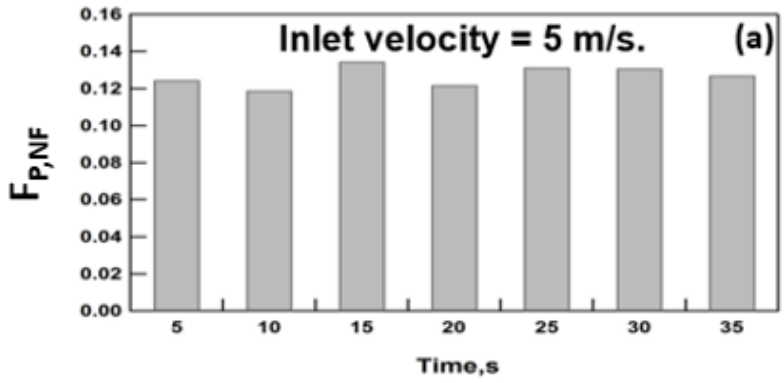

Figure 6.6 Fraction of particles entering the natural fracture subdomain, during each 5s interval at Vinlet =5.0m/s

Compared to the $F_{F,NF}$ = 30.3% of the fluid, $F_{P,NF}$ is much lower at the 12-14% level. This observation alone clearly demonstrates the superiority and the nessecity of using the discrete model (on which my simulator is based), as the interactions between proppant particles and fracture walls play an important role that cannot be ignored and lead to significant differences between $F_{F,NF}$ and $F_{P,NF}$, thus preclusing the use of $F_{F,NF}$ as an indivator of $F_{P,NF}$. The direct driving force that can make proppant particles change the initial direction of transport from the original HF into the NF is the drag force exerted by the fluid, as affected by the conservation of momentum. Before reaching the HF-NF intersection, the velocity of the proppant particles is unidirectional, with a single velocity component in the *x*-direction of the original HF. As the particles approach the intersection, the fluid drag force begins to add a *y*-component to the particle velocity vector, allowing movement in that direction. At the HF-NF intersection, the particle will enter the NF if it has moved sufficiently in the *y*-direction. The rest of the particles miss the NF window and are bounced back by the fracture walls to continue moving in the HF domain. This process is significantly different from the continuous mechanics that govern fluid transport (and are often used as an approximation of particle transport).

To investigate the influence of V_{inlet} on the proppant placement efficiency in the NF, I performed another simulation (Case T_2) with V_{inlet} = 2.5m/s, *i.e.*, only half of that in the reference Case T_1. The effect of the V_{inlet} is quantified by determining the corresponding $F_{P,NF}$, which is shown in **Fig. 6.7** that provides some significant results: compared to the $F_{P,NF}$ = 12-14% of proppant particles entering the NF in Case T_1, $F_{P,NF}$ in Case T_2 is significantly lower, *i.e.*, it is limited to the 2-3% level. Note that this fraction, estimated

at 5s time intervals, remains roughly constant for the duration of the study. This indicates that a reduction in V_{inlet} by 50% reduces $F_{P,NF}$ by a factor of about 5 compared to that in Case T_1.

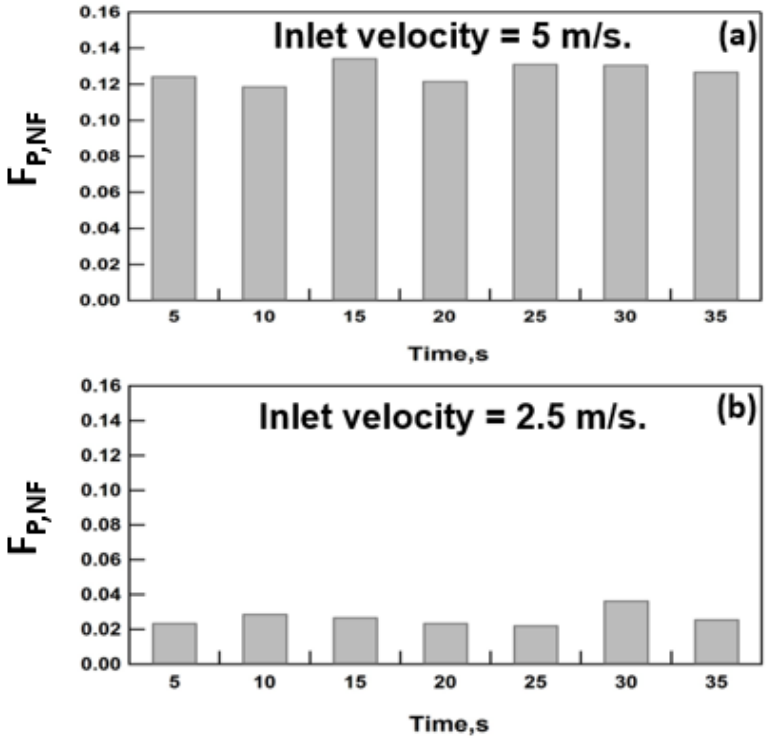

Figure 6.7 Fraction of particles entered the natural fracture subdomain, during each 5s interval at two boundary conditions: (a) Case T_1 V_{inlet} =5.0m/s (b) Case T_2 V_{inlet} = 2.5m/s

Fig. 6.8 shows a comparison of the fluid velocity fields in Cases T_1 and T_2. At the lower injection rate (which corresponds to the lower V_{inlet}) of Case T_2, the suspension transport region (shown in red in **Fig. 6.8(b)**) is significantly smaller than that in Case T_1 with the larger injection rate (see **Fig. 6.8(a)**). The white dashed line indicates the location of the

natural fracture. In Case T_2, the proppant bank build-up occurs before the HF-NF intersection, indicating that bedload transport is the dominant flow regime at the HF-NF interface. **Fig 6.8(b)** indicates that a very low number of proppant particles enter the NF (denoted by the regions of zero to very low fluid velocity), a dedution that is confirmed by the low numbers of particles entering the NF that have been independently computed and presented in **Fig. 6.7(b)**.

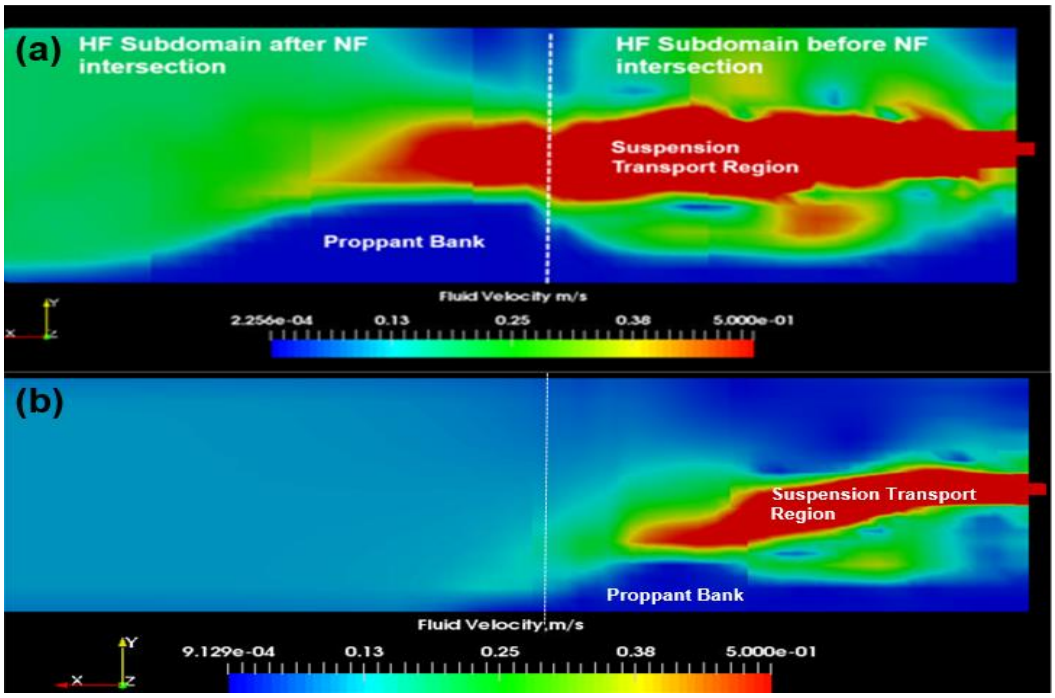

Figure 6.8 Comparison of the fluid velocity fields and size of the suspension transport regions: (a) Case T_1 with inlet velocity=5.0 m/s (b) Case T_2 with inlet velocity=2.5 m/s

Fig. 6.9 shows the particle velocity plots corresponding to Cases T_1 and T_2 at t = 200s. The amount (number) of proppant particles entering the NF in Case T_2 is very limited.

Combining this observation with the flow regime differences that I discussed above leads to a conclusion (rather expected) that the flow regime has a significant influence on the proppant placement efficiency in NF.

Specifically, proppant particles in the suspension transport regime (**Fig. 6.8(a)**) can be placed in the NF more efficiently than proppants in the bed load transport regime.

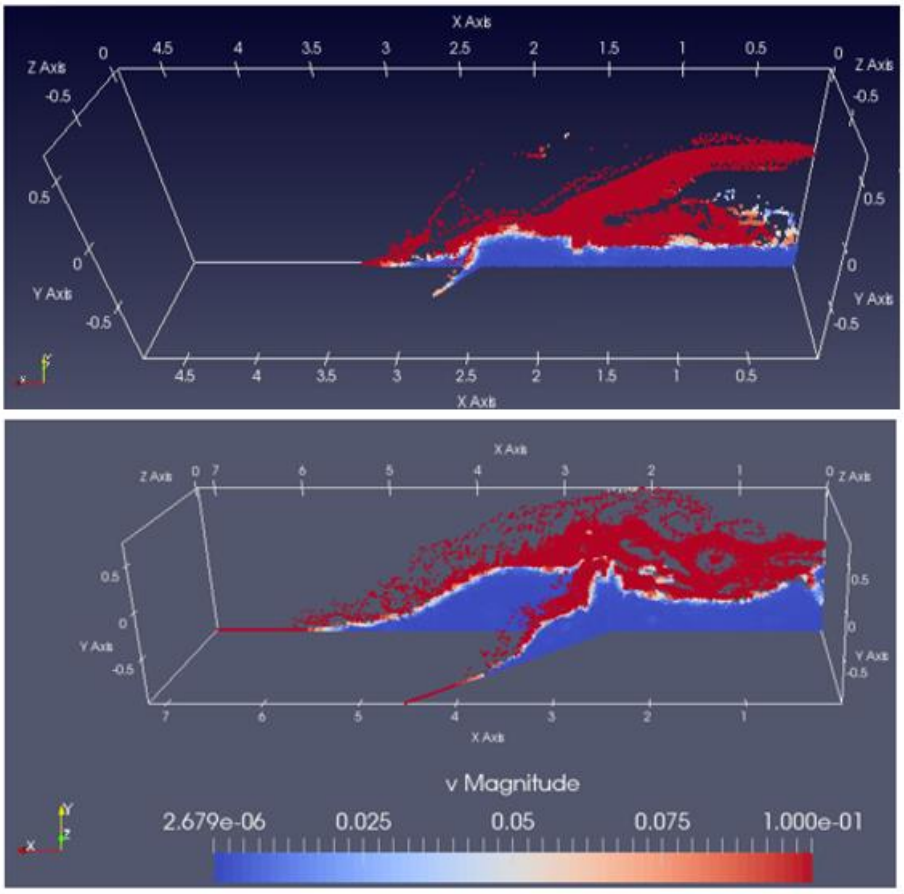

Figure 6.9 Comparison of the particle velocity and location plot : (a) Case T_2 with inlet velocity=2.5 m/s (b) Case T_1 with inlet velocity=5.0 m/s

For proppants in the bed-load transport regime (see **Fig. 6.8(b)**), the rolling friction and inter-particle collision rapidly dissipate the kinetic energy. Also, the fluid velocity is low in the bed-load transport regime, which provides a weaker driving force that can divert

proppants into the NF. The low proppant placement rate in the NF is attributed to these reasons.

To systematically study how the flow regime influces the proppant placement in the NF, I conducted a series of simulations using the T-shape domains discussed in Section X and listed in Table 6.2. This study included Cases T_3 to T_{11} in addition to Cases T_1 and T_2, from which they diferred only in the value of V_{inlet} that ranged from 2 m/s to 7 m/s. **Figs. 6.10** and **6.11** show the particle velocity distributions in the system subdomains, which is an accurate indicator of the proppant occurrence and distribution in the HF-NF continuum. These figures provide visual descriptions of the proppant numbers in the NF relative to the total particle numbers in the system for various V_{inlet} values.

Appendix C provides a more complete visualization of proppant velocity and location at various inlet velocity at multiple time steps. The most important observation from Figs. **6.10** and **6.11** is that the $F_{P,NF}$ behavior is not monotonic: it increases initially with a V_{inlet} increasing from 2 to 5 m/s, reaches a maximum for V_{inlet} = 5 m/s, and then $F_{P,NF}$ decreases for V_{inlet} > 5 m/s. Thus, there appears to exist an optimal velocity for maximal proppant placement in the natural fracture. As expected, the proppant reach increases with an increasing V_{inlet} for all T-cases.

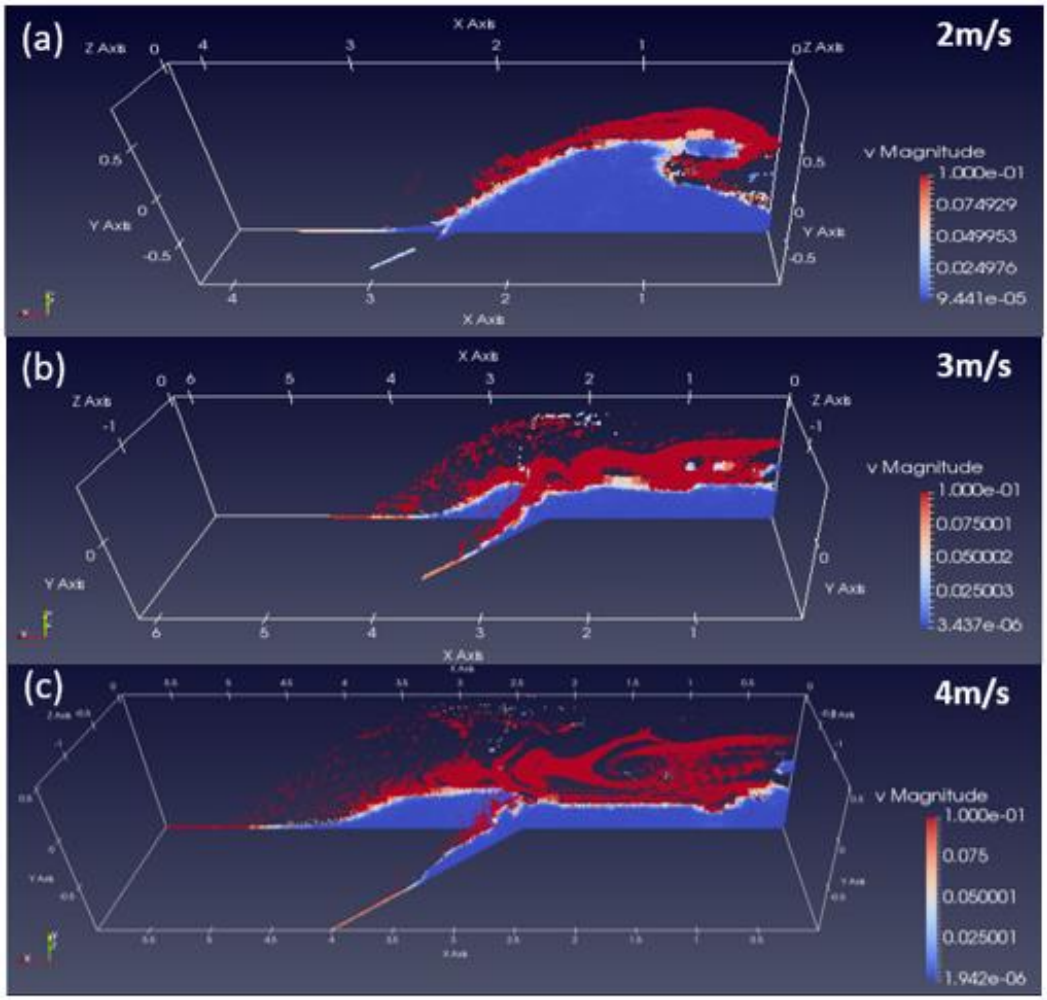

Figure 6.10 Proppant distribution at the HF-NF intersection with various of inlet velocity: (a) Vinlet=2m/s (b) Vinlet=3m/s (c) Vinlet=4m/s

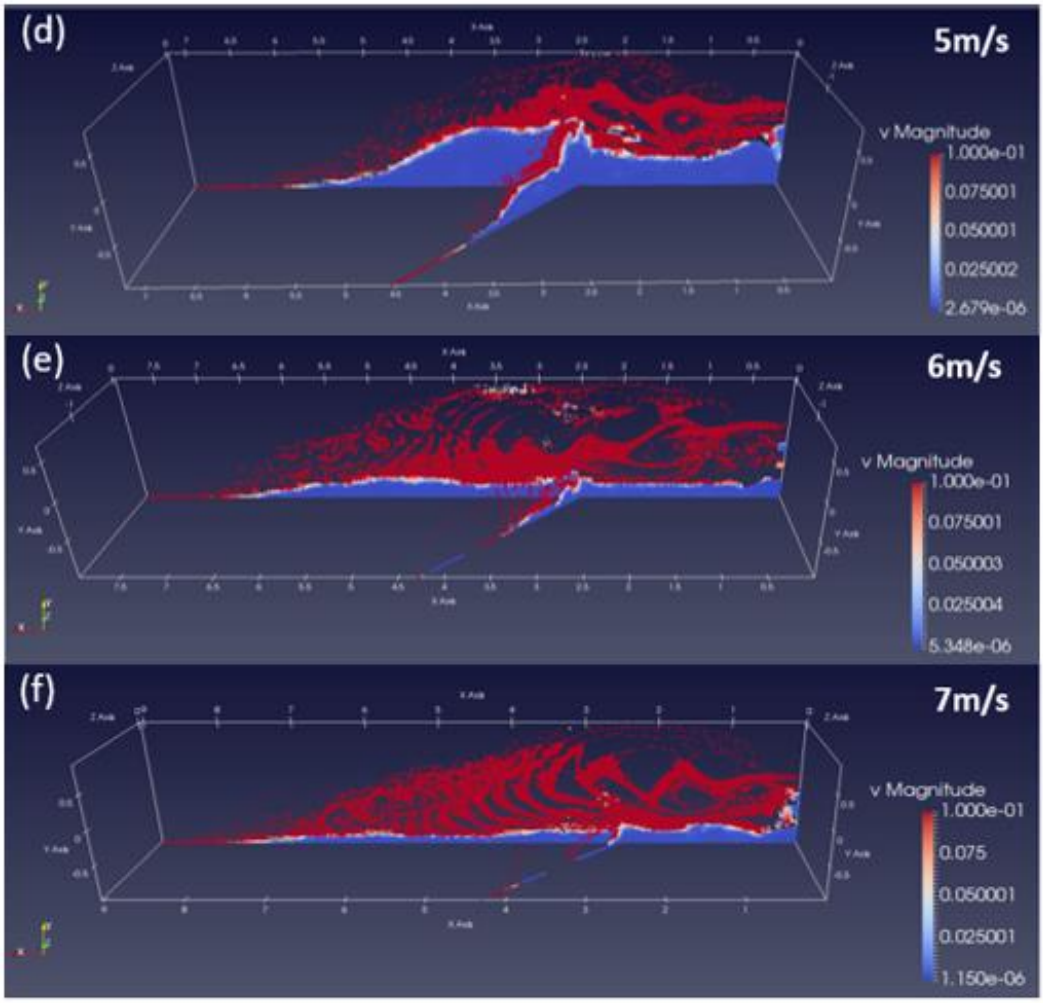

Figure 6.11 Proppant distribution at the HF-NF intersection with various of inlet velocity: (d) Vinlet=5m/s (e) Vinlet=6m/s (f) Vinlet=7m/s

In order to determine the relationship between the fluid velocity and $F_{P,NF}$, I sampled the fluid velocity in the HF at x = 2.4 m from the inlet, *i.e.*, at the location immediately before the HF-NF intersection that is denoted by the vertical dash line in **Fig. 6.12**.

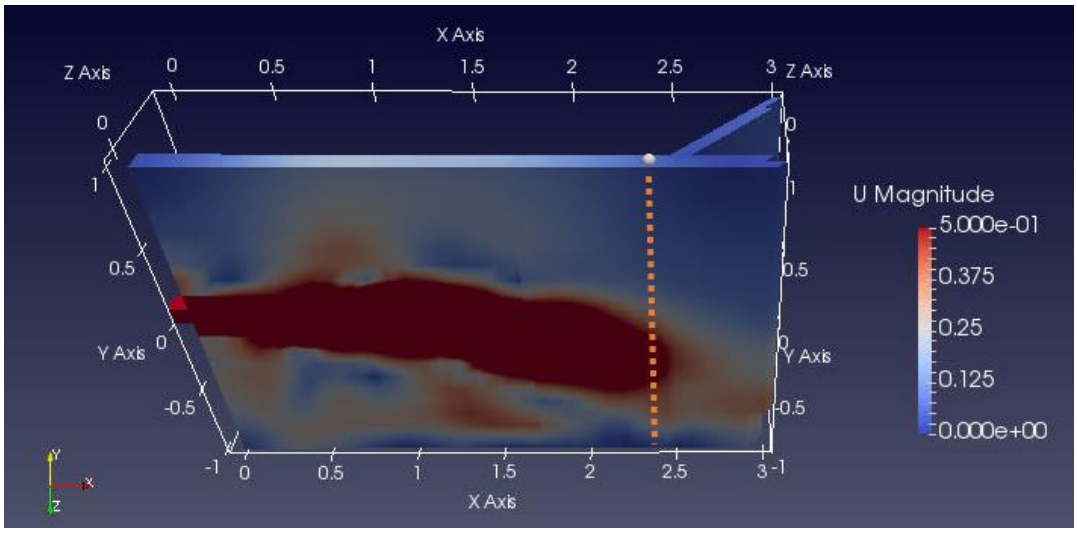

Figure 6.12. Location of flow velocity sampling (denoted by the dash line) immediately before the HF-NF intersection in all investigated cases (T_1 to T_{11}).

Figs. 6.13 and 6.14 show the variations in the fluid and particle velocity profiles (along the fracture height, measured from the base of the fracture) at a distance x = 2.4 m from the inlet and at t = 200 s for various V_{inlet} values. When V_{inlet} is low (= 2 m/s), it is clear that the flow regime at the HF-NF intersection is that of bed load transport regime (as shown in **Fig. 6.13 top**). As V_{inlet} increases, the flow regime transitions from bed load transport to suspension transport. **Figs. 6.13** and **6.14** show that for V_{inlet} > 3m/s, the proppant particles are transported at the same velocity as the fluid, which indicates that the flow regime is that of suspension transport in that region. In **Appendix D** I provide more fluid-particle velocity plots, in whichV_{inlet} increases at increments of 0.5 m/s.

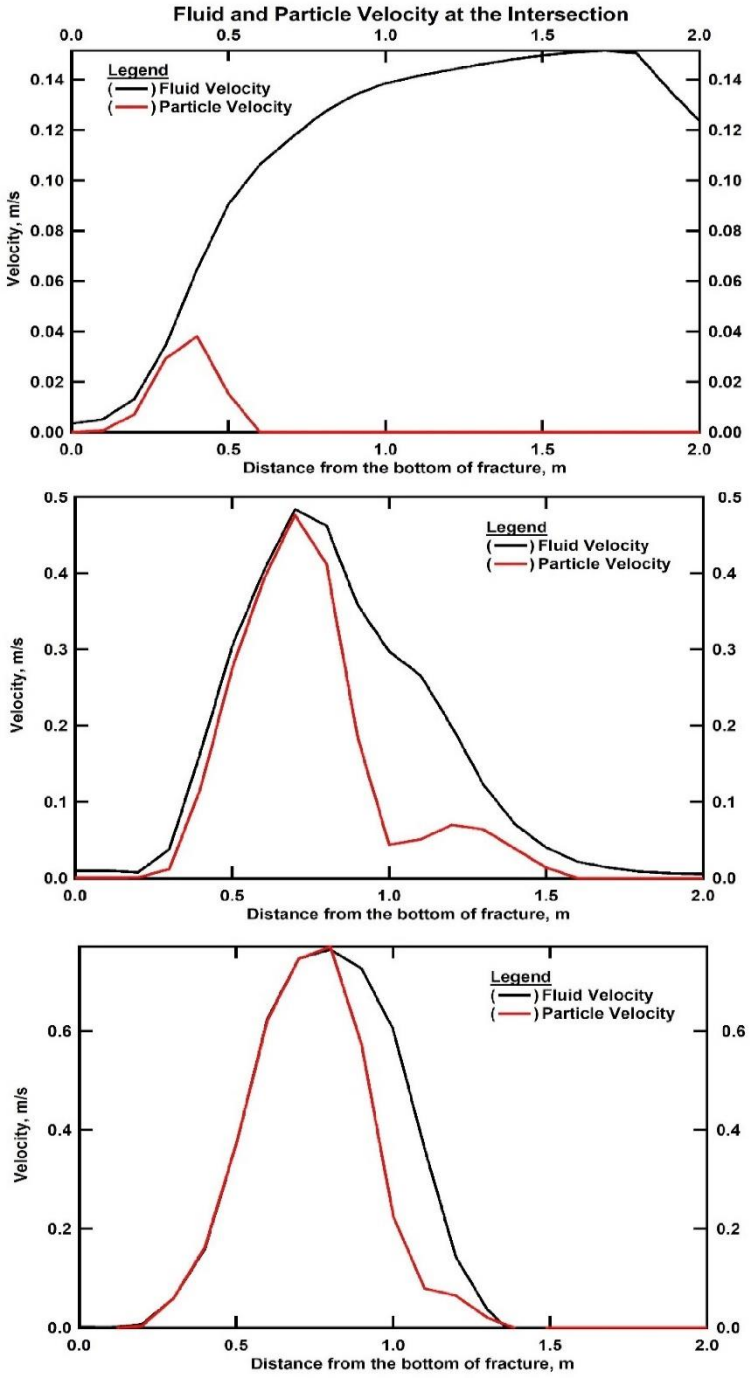

Figure 6.13. Fluid and particle velocity profile at HF-NF intersection at t=200s for cases: T_7 inlet velocity = 2m/s (top), T_3 inlet velocity = 3m/s (middle), and T_5 inlet velocity = 4m/s (bottom)

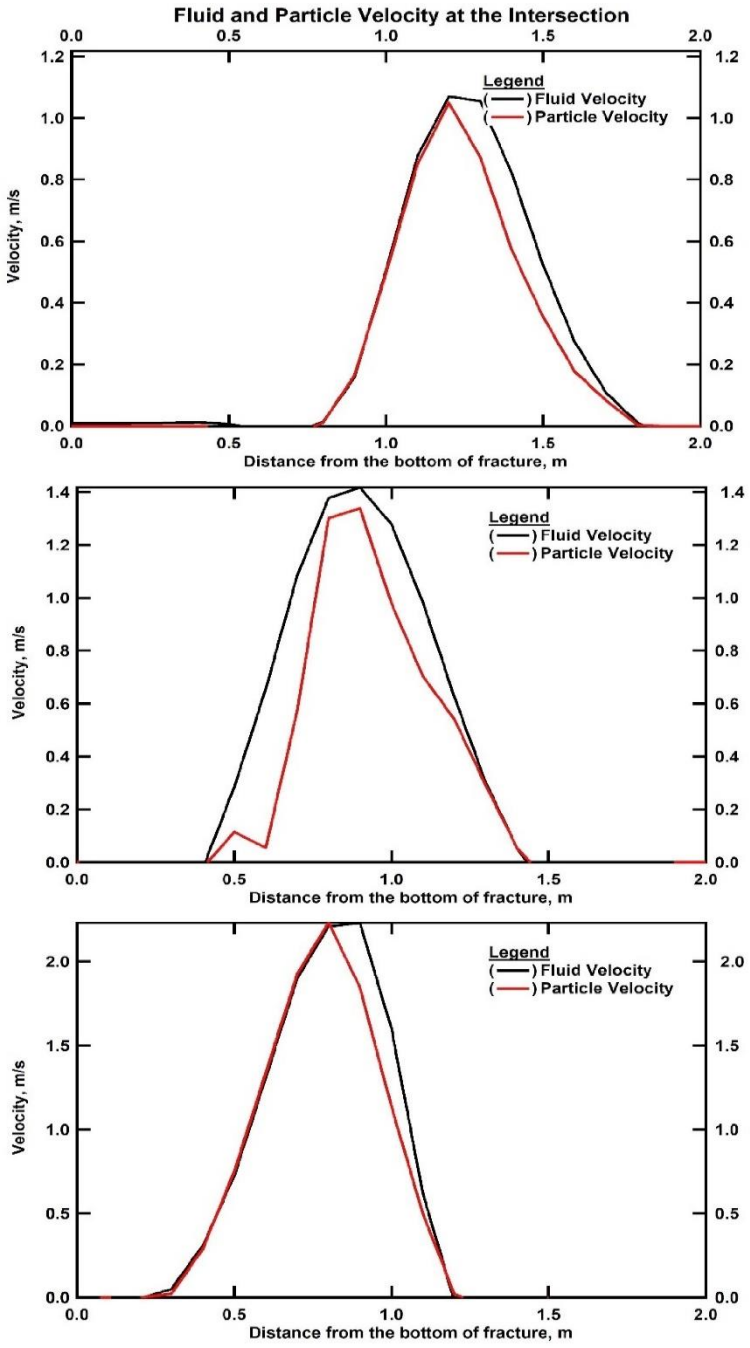

Figure 6.14. Fluid and particle velocity profile at HF-NF intersection at t=200s for cases: T1 inlet velocity = 5m/s (top), T9 inlet velocity = 6m/s (middle), and T11 inlet velocity = 7m/s (bottom)

The fluid velocity profiles in **Figs. 6.13** and **6.14** can be used to determine estimates of the peak fluid velocities at a monitoring location located 0.1 m away from the HF-NF intersection in all V_{inlet} cases. **Fig. 6.15** shows the peak fluid velocity at this sampling location near the HF-NF intersection. As V_{inlet} increases from 2 to 7 m/s, the peak velocity at the sampling location increases initially almost linearly with V_{inlet}, but the slope of the curve increases markedly for V_{inlet} > 6 m/s.

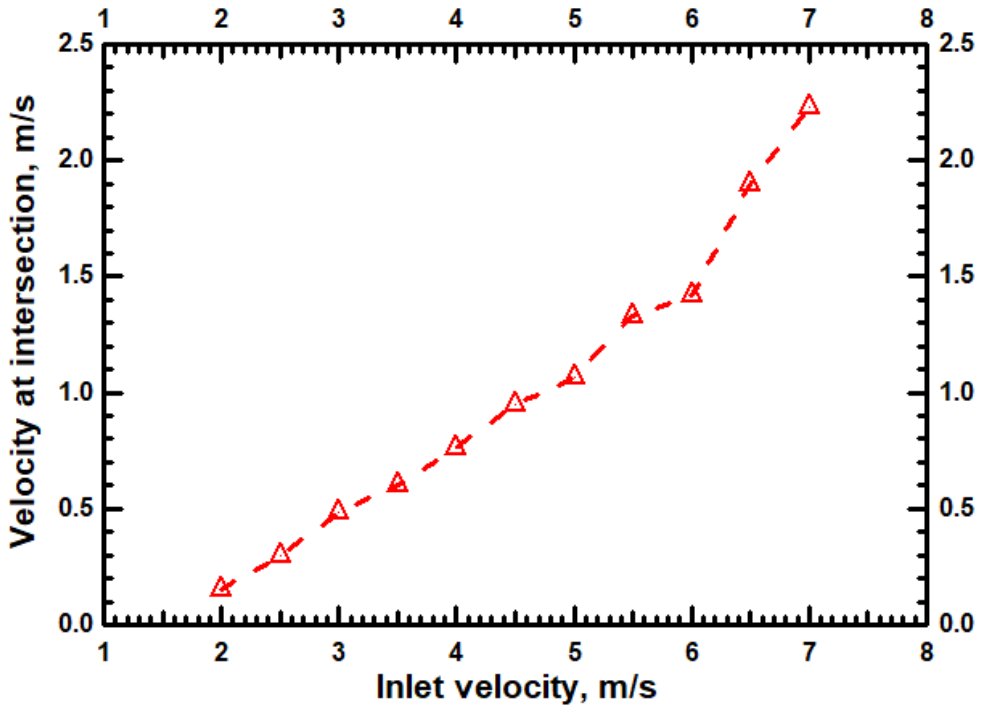

Figure 6.15 Peak fluid velocity 0.1 m away from the HF-NF intersection for inlet velocity ranging from 2m/s to 7m/s (t = 200 s)

Using the 5-step procedure I described earlier in this secion, I calculated the percentage of the proppant entering the NF domain ($F_{P,NF}$) during the entire simulation period. **Figs. 6.16** to **Fig. 6.26** shows the evolution of $F_{P,NF}$ in each of the V_{inlet} cases that I considered.

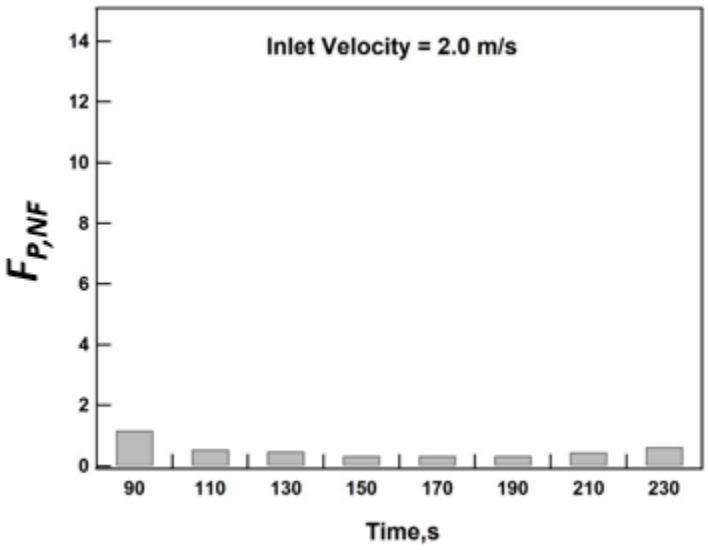

Figure 6.16 Percentage of proppant entered NF sub-domain during 20s interval, with inlet velocity = 2.0m/s

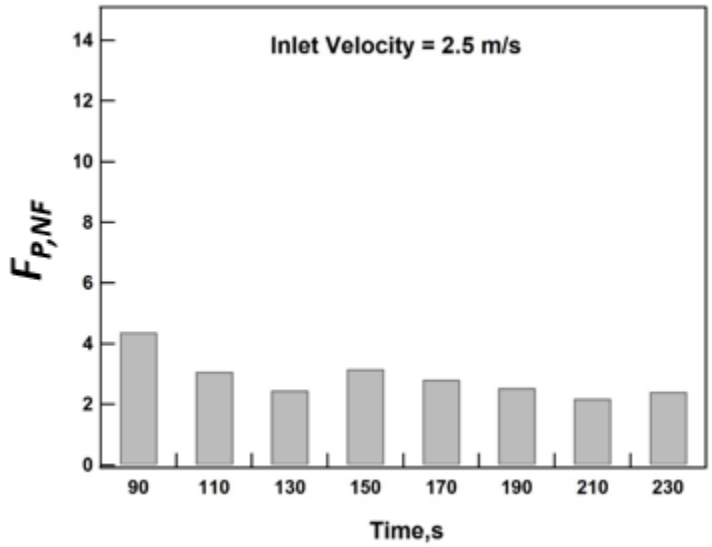

Figure 6.17 Percentage of proppant entered NF sub-domain during 20s interval, with inlet velocity = 2.5m/s

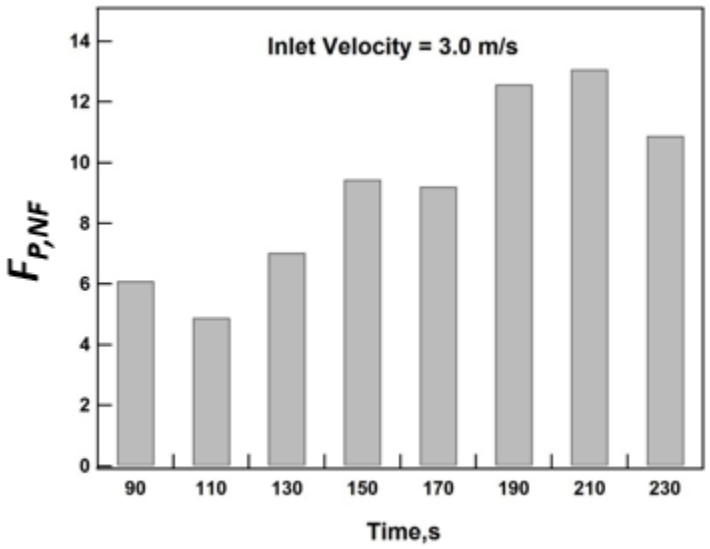

Figure 6.18 Percentage of proppant entered NF sub-domain during 20s interval, with inlet velocity = 3.0m/s

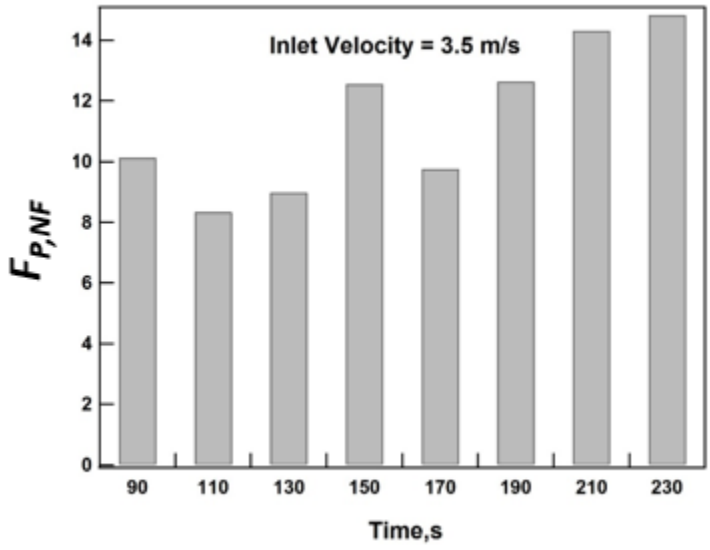

Figure 6.19 Percentage of proppant entered NF sub-domain during 20s interval, with inlet velocity = 3.5m/s

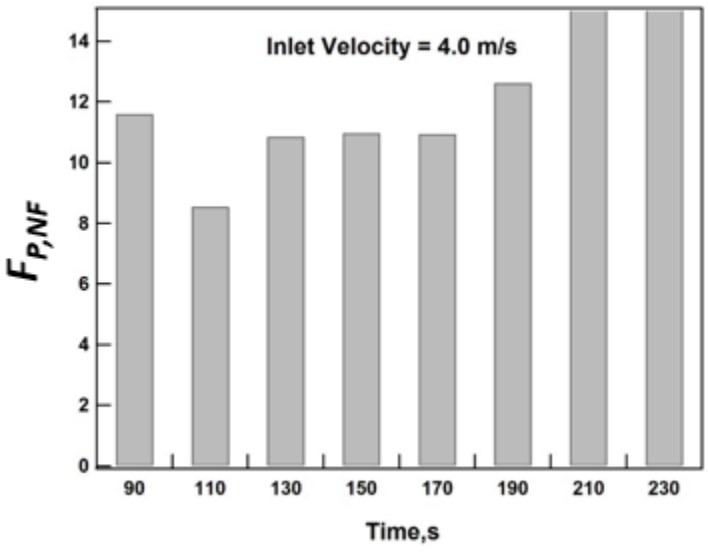

Figure 6.20 Percentage of proppant entered NF sub-domain during 20s interval, with inlet velocity = 4.0m/s

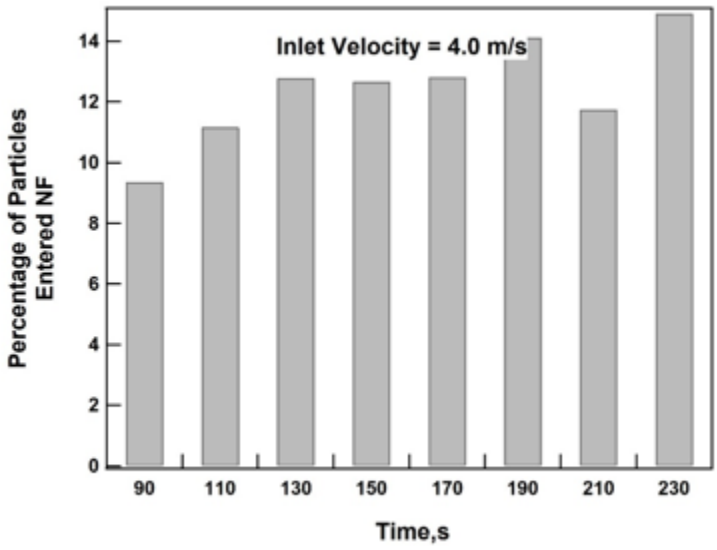

Figure 6.21 Percentage of proppant entered NF sub-domain during 20s interval, with inlet velocity = 4.5m/s

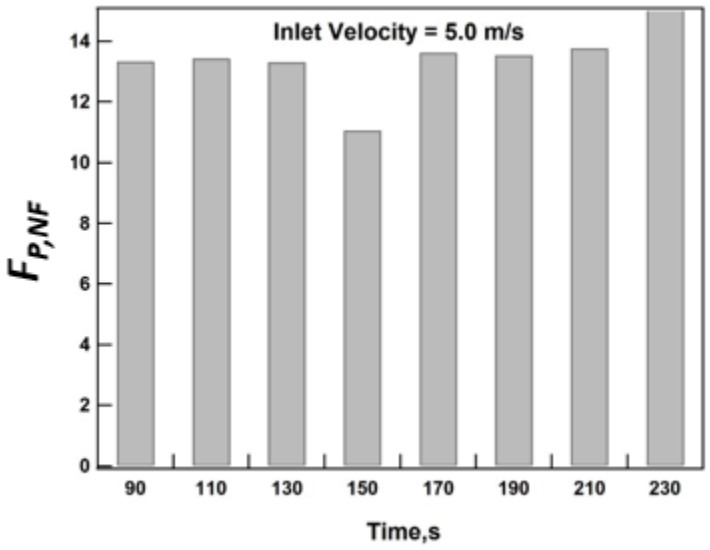

Figure 6.22 Percentage of proppant entered NF sub-domain during 20s interval, with inlet velocity = 5.0m/s

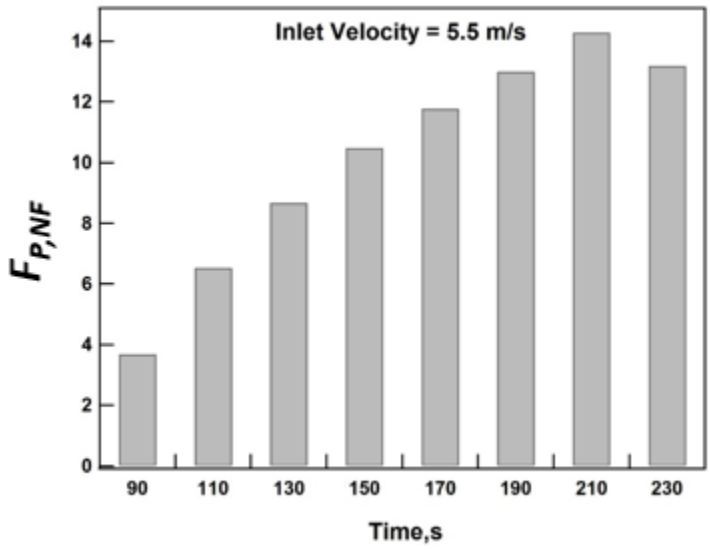

Figure 6.23 Percentage of proppant entered NF sub-domain during 20s interval, with inlet velocity = 5.5m/s

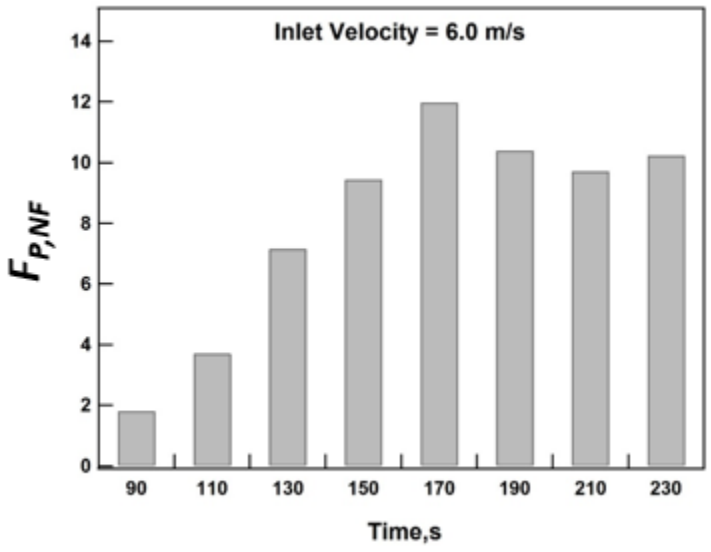

Figure 6.24 Percentage of proppant entered NF sub-domain during 20s interval, with inlet velocity = 6.0m/s

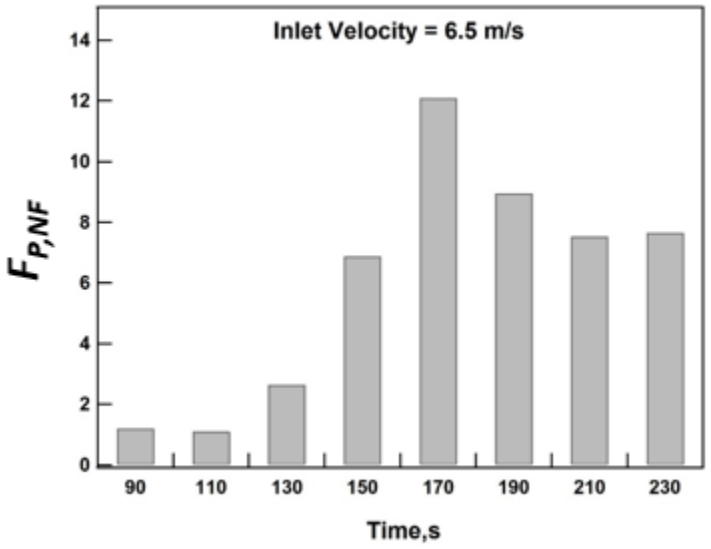

Figure 6.25 Percentage of proppant entered NF sub-domain during 20s interval, with inlet velocity = 6.5m/s

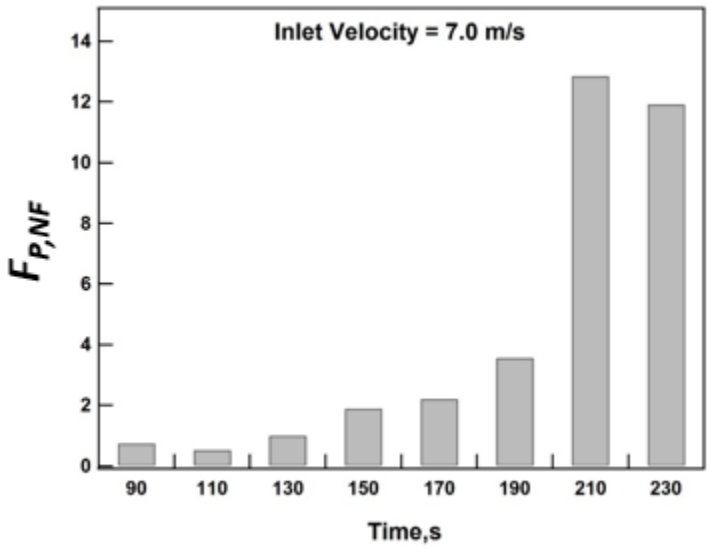

Figure 6.26 Percentage of proppant entered NF sub-domain during 20s interval, with inlet velocity = 7.0m/s

Fig. 6.16 shows a significant contrast between the $F_{P,NF}$ for a V_{inlet} = 2.0 m/s and for all other V_{inlet} cases. The fluid velocity profile plot (**Fig. 5.13**) provides evidence that this difference in the proppant placement efficiency is caused by the very different flow regimes. When V_{inlet} increases to 2.5 m/s, the flow regime begins to transition from bed load transport to suspension transport. When V_{inlet} reaches 5m/s (**Fig 5.6 and 5.12**), there is a strong suspension transport signature in the velocity profile and $F_{P,NF}$ is stable at the 12-14% level for the duration of the study. **Figs. 6.16 to 6.26** show different patterns of $F_{P,NF}$ evolution during the simulation period. $F_{P,NF}$ is practically stable for the duration of the study for V_{inlet} = 5.0 m/s, but shows a strong time dependence for V_{inlet} > 5.0 m/s, with $F_{P,NF}$ increasing with time early in the injection process (the later behavior is inconsistent).

For V_{inlet} < 5.0 m/s, the $F_{P,NF}$ followed a different pattern and appeared generally stable over time, with some osciallations about the mean.

Fig. 6.27 summarizes the average $F_{P,NF}$ results for all of the V_{inlet} cases. As indicated earlier, the most interesting observation is that the maximum proppant placement efficiency in the NF is attained for a V_{inlet} = 5m/s. Larger and lower V_{inlet} values are shown to reduce the average $F_{P,NF}$. For V_{inlet} < 5m/s, this is because because higher fluid velocity helps the proppant particles to stay suspended. Suspended particles are easier to transport into the natural fracture by the fluid. For V_{inlet} > 5m/s, this is because the proppant particles move too fast in the *x*-direction, thus reducing the probability of entering the NF window. This quantitative result is in agreement with the visual (qualitative) observations in **Figs. 6.10** and **6.11**, and suggests that, for a NF with a given aperture, there exists an optimal V_{inlet} that yields a maximum $F_{P,NF}$.

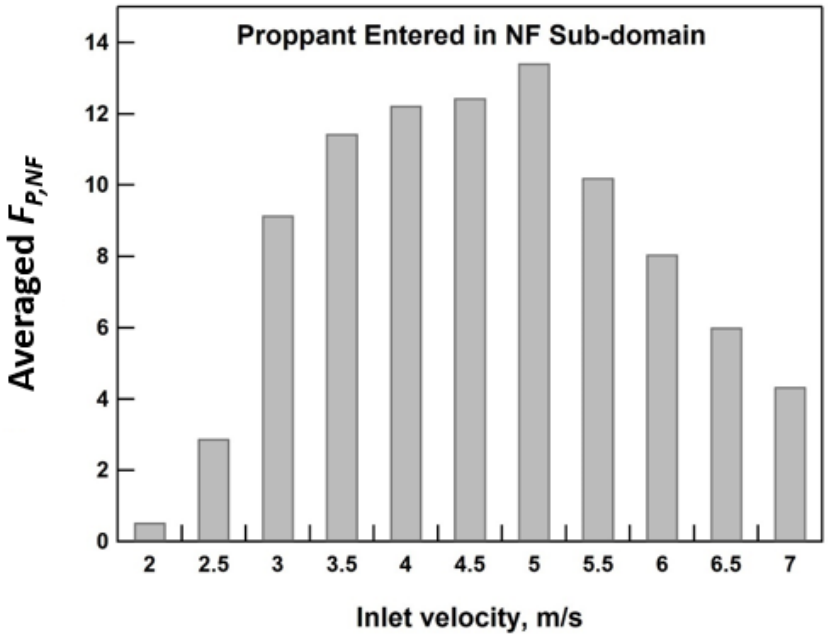

Figure 6.27 Dependence of the average $F_{P,NF}$ (percentage of proppant entered the NF domain) on inlet velocity (ranging from 2m/s to 7m/s)

7. PROPPANT TRANSPORT THROUGH COMPLEX SHARPLY ANGLED INTERSECTING FRACTURES: Z-INTERSECTIONS

7.1. The Z-shaped HF-NF intersection

This section focuses on transport at and through Z-type intersections, *i.e.*, when a NF arrests the propagation of a HF by redirecting flow into a path of least resistance. It is generally assumed that the direction of hydraulic fracture propagation is perpendicular to the direction of the minimum horizontal stress. However, because of a combination of depositional, geodynamic, and tectonic processes, the direction of pre-existing natural fractures does not have to be on the same direction. Thus, during the fracturing operation, NFs can be connected to, and activated by, HFs. The aperture of a NF is usually (but not always) narrower than that of a HF because of the former's non-alignment with the HF direction. The smaller NF aperture creates a narrower flow area that would be available for proppant intrusion at the HF-NF intersection. This can often lead to proppant accumulation and blockage of fluid flow and proppant transport path at this location, in a phenomenon called proppant bridging.

7.2. Simulation Domain and System Conditions in Z-Intersection Studies

To study proppant transport at the HF-NF junction of a Z-intersection and the bridging phenomenon, I constructed the simulation domain shown in **Fig. 7.1**, in which the NF subdomain has a narrower aperture and, consequently, a narrower flow area. The main difference from the domain geometry in the T-intersection study in **Section 6.2** is that the HF in the Z-shape intersection model does not extend past the NF intersection. The

dimensions (length, height) of the HF and NF components of the simulation domain are the same as in **Section 5.2.** *In all of my Z-shaped models, the NF aperture is* 0.7 *times of NF aperture*. Detailed HF and NF aperture values are provided in **Section 7.3.** Fluid and proppant particles enter the HF from an inlet located at the mid-point of the right-hand boundary (**Fig. 7.1**). At the HF-NF interface, the slurry flows through a sharp corner (45 degree) and enters the narrower NF. By varying the NF aperture in the Z-shape intersection model, I analyzed the conditions that can cause proppant bridging (blockage) at the HF-NF interface and developed criteria for avoiding this problem.

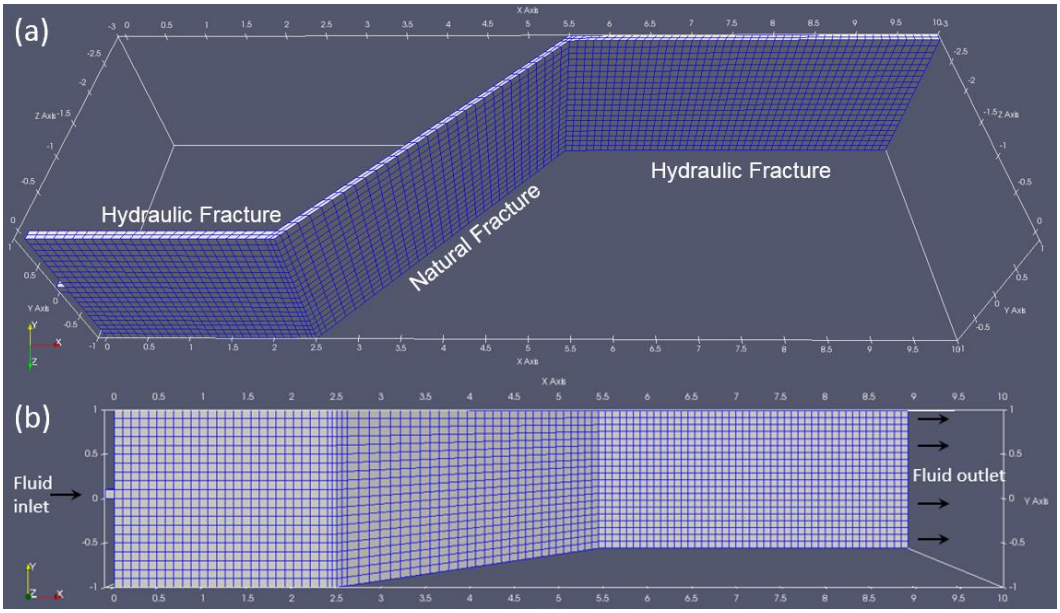

Figure 7.1 The domain used in the HF-NF intersection studies: (a) 3D view , and (b) side view of the Z-shape HF-NF simulation domain with boundary condition

7.3. Cases of Z-Intersection Studies

I constructed multiple Z-Intersection models to study the bridging phenomenon at the junction of the HF with the narrow NF. **Table 7.1** lists the names and specifics of the HF/NF Z-intersection cases that I investigated. As mentioned in **Section 7.2**, the height and length of the all Z-Intersection models are the same (2m height, 10m length), and they only varied in the proppant concentrations and the apertures of the HF and NF sections. The CG particles used in all cases are of the same size, with a proppant diameter d_{pp}= 0.01m. The scaling factor was 10, which means the original particle diameter was 0.001m. The proppant concentration (C_p) is different each Z-case. C_p and the ratio of NF aperture and particle diameter (R_{fp}) the various Z-cases are listed in **Table 7.1**. The inlet velocity V_{inlet} = 5 m/s for all Z-cases. This is the same V_{inlet} used in in my studies of vertical, dipping and T-Intersection fractures (see **Sections 5.3, 5.5** and **6.4**).

Table 7.1 Parameters for the T-intersection fracture simulation domain

Case Number	HF Aperture, m	NF Aperture, m	R_{fp}	C_p, PPA
Z_1	0.04	0.0283	2.82	7.03
Z_2	0.01	0.0141	1.41	7.03
Z_3	0.01	0.0141	1.41	2.49
Z_4	0.01	0.0141	1.41	1.36
Z_5	0.017	0.012	1.2	0.68
Z_6	0.01	0.0141	1.41	0.83
Z_7	0.024	0.017	1.7	1.66
Z_8	0.024	0.017	1.7	2.24
Z_9	0.024	0.017	1.7	5.49
Z_{10}	0.024	0.017	1.7	3.32
Z_{11}	0.03	0.0212	2.12	4.15
Z_{12}	0.03	0.0212	2.12	5.39
Z_{13}	0.03	0.0212	2.12	8.46
Z_{14}	0.034	0.024	2.4	5.99
Z_{15}	0.034	0.024	2.4	7.46
Z_{16}	0.034	0.024	2.4	9.12
Z_{17}	0.04	0.0283	2.82	7.86
Z_{18}	0.04	0.0283	2.82	9.84
Z_{19}	0.017	0.012	1.2	1.04
Z_{20}	0.017	0.012	1.2	2.07
Z_{21}	0.018	0.013	1.3	3.32
Z_{22}	0.018	0.013	1.3	8.46

7.4. Simulation Studies of Fluid Flow and Proppant Transport at Z-Intersections

Fig. 7.2 shows the proppant location and velocity at time t =100 seconds in two Z-type fracture systems (Cases Z_1 and Z_2) with different HF and NF apertures. The inlet proppant concentration C_p in both cases is 7.03 PPA (Pounds Per gallon Added). In Case Z1, $W_{f,NF}$ = 2.82×d_{pp} and the proppant particles were continuously transported past the HF-NF intersection into the NF. By decreasing the NF aperture (or, by increasing the proppant particle diameter), proppant bridging at the HF-NF interface occurred. Thus, in Case Z_2, the smaller NF aperture $W_{f,NF}$ = 1.41×d_{pp} led to proppant bridging at the HF-NF interface. A small amount of proppant managed to flow past the intersection into the NF before bridging occurred. Once bridging occurs, flow and transport into the NF is blocked and proppants begin to accumulate at the HF-NF intersection, packing back toward the inlet and leading to an early screen-out.

Fig. 7.3 shows the fluid velocity plot corresponding to Case Z_1 and Case Z_2 at t=100s. The fluid velocity plot for Case Z_1 (**Fig. 7.3** bottom) shows the suspension transport region (shown in red, delineated by the 0.5 m/s cut-off velocity, as explained in Section 5.3) extending beyond the sharply angled intersection into the NF domain. This helps achieve continuous proppant transport. In Case Z_2, because of bridging at the HF-NF interface (**Fig. 7.2** top), proppant particles are stopped in the HF domain and fluid is re-directed toward the top of the fracture. In this case, filtered fluid flows through a choked proppant pack and proppant id prevented from further transport into the NF. Even through the velocity may appear to reach the “suspension” cut-off value, there is practically no proppant to be suspended in the NF domain.

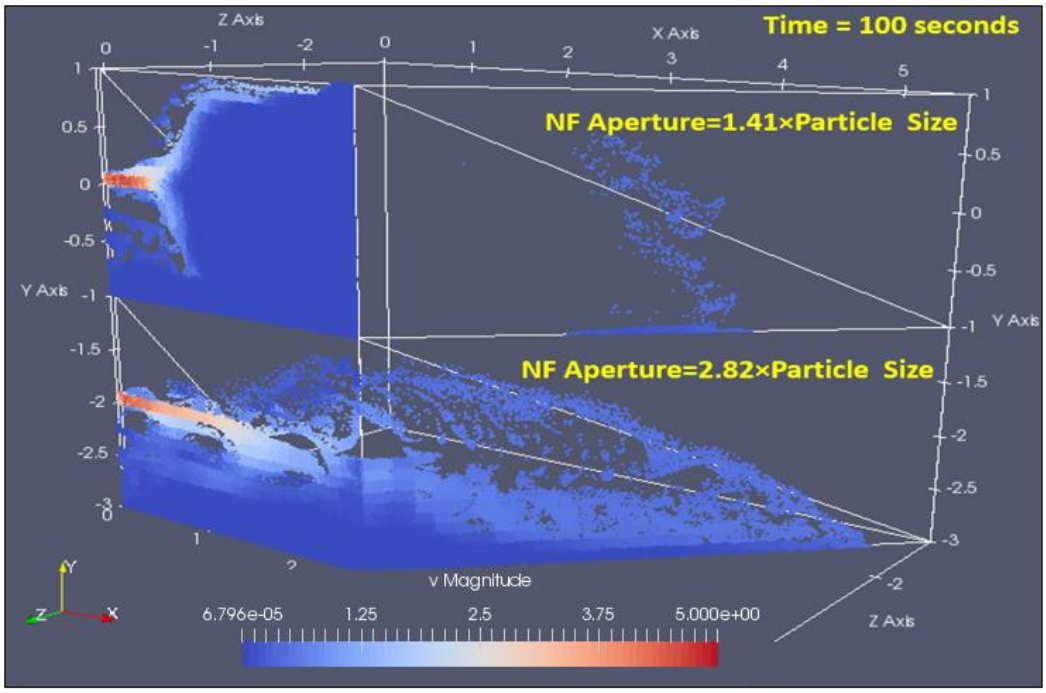

Figure 7.2 Proppant velocity and location in the domain at t = 100 s in Case Z_1 (bottom) where $W_{f,NF}$ = 2.82×dpp, and Case Z_2 (top) where Wf,NF = 2.82×dpp

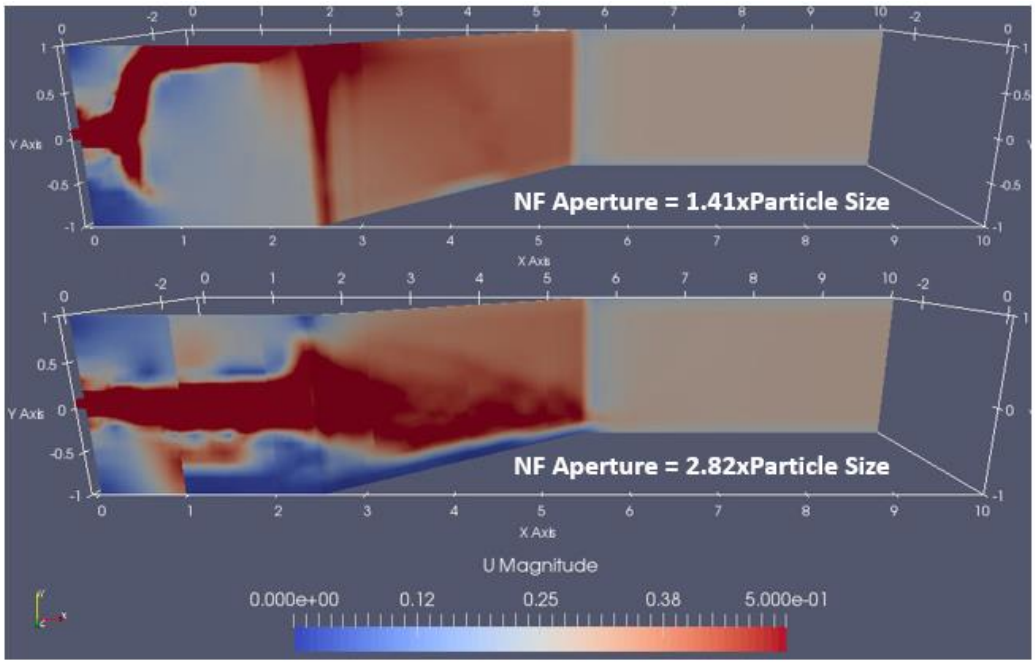

Figure 7.3 Fluid velocity field in the domain at t = 100 s in Case Z1 (bottom) where $W_{f,NF}$ = 2.82×dpp, and Case 2 (top) where $W_{f,NF}$ = 2.82×dpp

These results show that the ratio $R_{fp} = W_{f,NF} / d_{pp}$ is critical in determining the occurrence of proppant bridging. For a proppant particle to be transported continuously into the NF past a Z-intersection, R_{fp} obviously must be larger than 1.0 (for R_{fp} <= 0, the particles are strained at the intersection because of the physical inability of particles to flow through an aperture smaller then d_{pp}). However, the results of this study in Fig. **7.3** show that R_{fp} >1.0 is a necessary but insufficient condition to avoid proppant bridging. Additionally, other factors such as the proppant concentration C_p may play an important role.

To test this theory, I investigated the sensitivity of proppant bridging occurrence to C_p in a set of three numerical experiments (Cases Z2, Z3, and Z_4), the results of which are shown in **Fig. 7.4**. In all three experiments, $W_{f,NF} = 1.41 \times d_{pp}$. From bottom to top in **Fig. 7.4**, C_p = 7.03 PPA, 2.49 PPA and 1.36 PPA in Cases Z_2, Z_3 and Z_4 respectively.

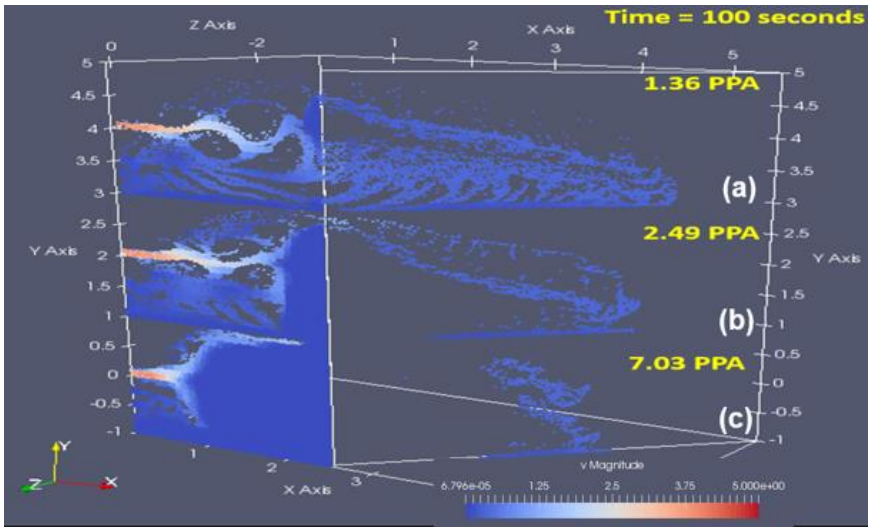

Figure 7.4 Proppant distribution at t = 100 s in three numerical experiments with $W_{f,NF}$ = 1.41×dpp: (a) Case Z4, C_p = 1.36 PPA, (b) Case Z3, C_p = 2.49 PPA and (c) Case Z2, C_p = 7.03 PPA

Fig. 7.4 shows that proppant bridging still occurs for C_p = 2.49 PPA and 7.03 PPA (Cases Z_3 and Z_2, respectively) despite a R_{fp} = 1.41 >1.0. However, there is a difference in the bridging pattern, as the proppant pack builds slower in Case Z_3 in which the proppant concentration C_p is lower than in Case Z_2. When the proppant concentration declines to C_p = 1.36 PPA in Case Z_4 (**Fig. 7.4(c)**), the proppant appears to be continuously transported from the HF into the NF subdomain without blocking the HF-NF intersection. The inevitable conclusion from the analysis of these results is that a lower C_p will mitigate the occurrence of proppant bridging, provided that R_{fp} >1.0. Thus, for R_{fp} = 1.41, continuous placement of proppant in the NF is achievable when C_p is reduced to a sufficiently low level. *i.e.*, about 1 PPA. This observation agrees with current industry practices. To achieve a higher proppant placement efficiency, field experience (without the benefit of numerical simulation analysis such as the one described here) has led to the majority of recent fracture designs being designed to use a low C_p of around 1 PPA.

Fig. 7.5 shows the fluid velocity plot corresponding to Cases Z_2, Z_3 and Z_4. In Case Z_2 (**Fig. 7.5 (c)**), proppant bridging occurs (confirmed in **Fig. 7.4 (c)**). Thus, there exists a large area of low fluid velocity (shown in blue) at the HF-NF interface (at about x = 2.5m). Proppant bridging also occurs in case Z_3. However, in this case there is a small channel near the top of the fracture at t = 100s, which allows fluid flow and particle transport. Therefore, the low velocity zone (in **Fig. 7.4(b)** exists at the lower 2/3rds of the HF-NF interface. In Case Z_4, continuous transport (shown in red) occurs at most of the HF-NF interface, with the exception of a small fraction of the HF-NF interface where velocities are low (denoted by the blue color). I identified this *blue region* as temporary bridging,

which may occur at random locations within the HF-NF interface at medium to low proppant concentration (C_p).

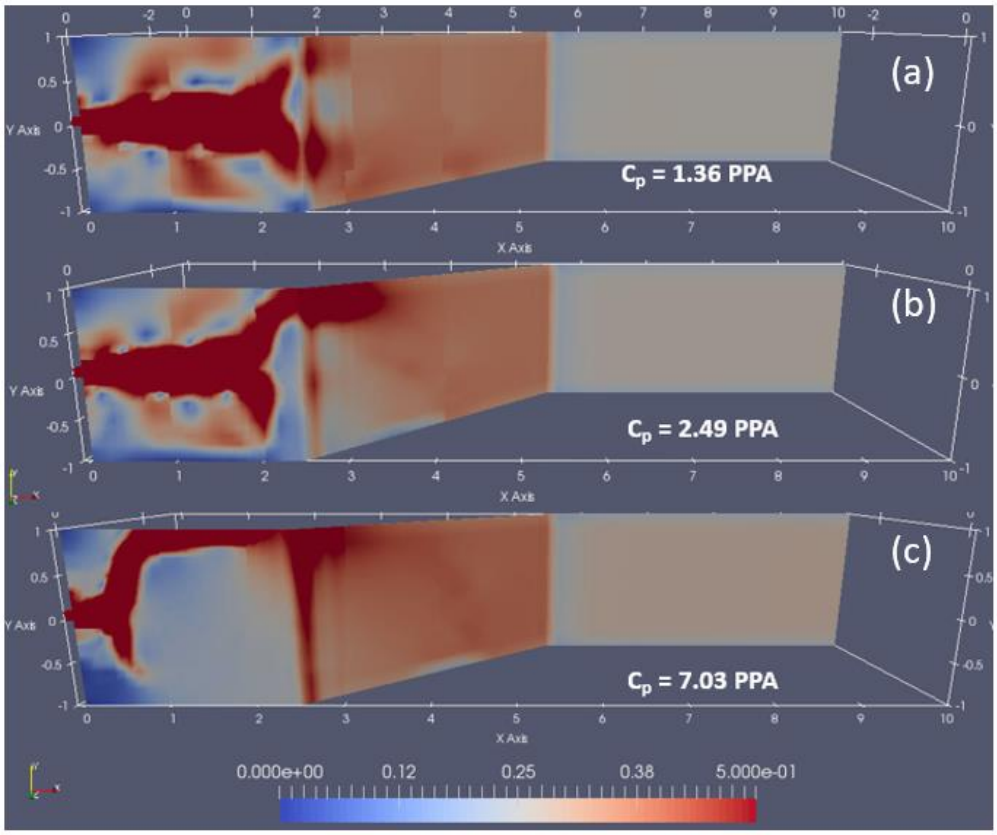

Figure 7.5 Proppant distribution at t = 100 s in three numerical experiments with $W_{f,NF}$ = 1.41×dpp: (a) Case Z_4, C_p = 1.36 PPA, (b) Case Z_3, C_p = 2.49 PPA and (c) Case Z_2, p = 7.03 PPA

To explore the physics of temporary bridging for a low C_p, I investigated the particle behavior at the HF-NF interface in Case Z_4. The results are shown in **Fig. 7.6**. The color of the particles denotes their velocity, with blue representing the zero-velocity particles that cause bridging at the interface. As the particle swarm approaches the interface, there

is a possibility that some particles will partially block the interface. When C_p is low, bridging can be eliminated as the immobilized particles are flushed away by the fluid, as shown in **Fig. 7.6**. On the other hand, if C_p is high, the incoming particle swarm will continue to accumulate at the HF-NF intersection and to expand the bridging, leading eventually to the complete blockage of the entire HF-NF interface.

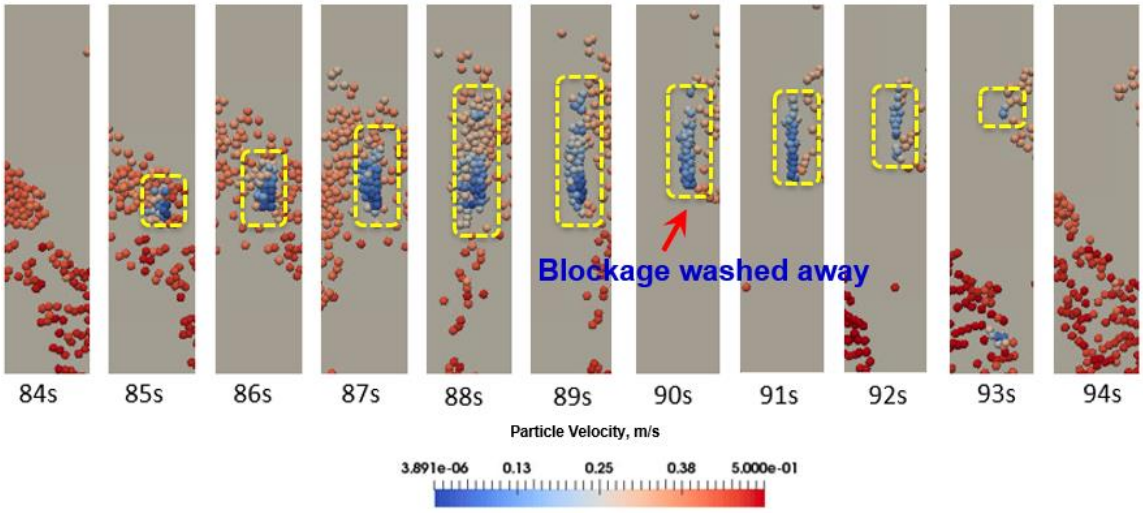

Figure 7.6 Case Z4: Evolution of the proppant distribution and temporary bridging flushing at the HF-NF interface ($W_{f,NF}$ = 1.41×d_{pp} and C_p = 1.36 PPA)

The results of this simulation study provides a robust scientific basis and explains the physics behind the empirical practice of lowering C_p to about 1.0 PPA to enable the continuous (uninterrupted) transport of the proppant particles past the Z-intersection into the (usually) narrow natural fractures ($W_{f,NF}$ = 1.41×d_{pp}), thus reducing or eliminating the risk of proppant bridging and preventing early screen-out.

My numerical experiments showed that C_p and R_{fp} are the two critical parameters that determine the occurrence or avoidance of proppant bridging (blocking). For a fixed value of R_{fp}, continuous transportation of proppant is possible only when C_p is smaller than a threshold value. To develop quantitative bridging criteria that can be used in engineering designs and field applications, I conducted the set of proppant transport simulations (listed in **Table 7.1**) by varying the C_p and R_{fp} values and recording the occurrence or avoidance of proppant blocking at the HF-NF intersection. A detailed record of the results of these simulations is included in **Tables E-1** and **E-2** in Appendix E.

Fig. 7.7 shows the results of all the numerical experiments that were conducted in the effort to develop the quantitative bridging criteria. Each point in this figure represents a proppant transport simulation with a different set of C_p and R_{fp} values. The color of the points indicates the occurrence or avoidance of bridging/blocking: the red points indicate continuous proppant transport and bridging avoidance, and the blue points indicate emergence of bridging and blockage at the HF-NF interface. **Fig. 7.7** shows that an increasing R_{fp} is associated with an increasing $C_{p,max}$ (*i.e.*, the maximum C_p that does not result in bridging, represented by the dashed line in the figure). In essence, the C_p vs. R_{fp} curve defines the boundary of possible bridging, and their relationship is nonlinear.

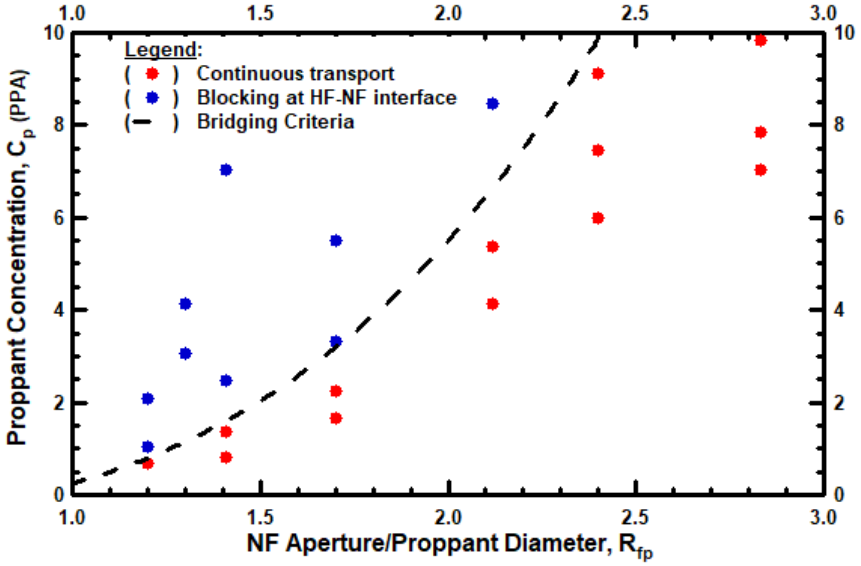

Figure 7.7 Summary of numerical experiment results for the Z-shape intersection model and bridging criteria as a function of R_{fp} and C_p

Based on the results shown in **Fig. 7.7**, I propose the following simple equation that can quantify the bridging criterion by defining the maximum proppant concentration $C_{p,max}$ that can be injected and transported without blocking the HF-NF interface:

$$C_{p,max} = \frac{3}{4} R_{fp}{}^{3} - \frac{1}{2} \quad \text{.....(7.1)}$$

The curve defined by this simple blocking criterion separates the two groups. Using the estimated R_{fp} as an input, the $C_{p,max}$ value can be easily obtained and used for the selection of the appropriately-sized proppant. For field operations, it is suggested that $C_{p,max}$ not be exceeded in order to achieve maximum proppant placement efficiency and avoid proppant bridging. Although **Eq. 7.1** (used for the determination of $C_{p,max}$) describes a simple relationship, it's geometric nature appears to have strong fundamental underpinnings and

may have some relation to the specific physics for this problem. The input parameter R_{fp} is a dimensionless length variable, and raised to the 3rd power it represents a sort of dimensionless volume. Thus, **Eq. 7.1** shows that the maximum allowable proppant concentration for bridging avoidance is determined by the dimensionless volume of the proppant particles. In other words, at unit time, the maximum volume of proppant that can flow uninterrupted through the NF interface determines $C_{p,max}$.

8. MULTI-CLUSTER PROPPANT TRANSPORT

In this section, I present preliminary results of proppant transport for the case of a multi-cluster completion in a horizontal wellbore. This section is divided into two subsections. In subsection 8.1, I discuss the construction of the multi-cluster horizontal wellbore model that involves a 40 m-long horizontal wellbore section with 3 vertical planar hydraulic fractures. This model represents a common multi-cluster fracturing design, in which there are multiple clusters (ranging from as few as 3 to more than 10) within a given stage, with stage lengths ranging from 30m to 150m. In subsection 8.2, I analyze the numerical simulation results, aiming to determine the proppant distribution pattern with regard to the fluid velocity

8.1. Multi-cluster Horizontal Wellbore Model

Current fracturing designs for unconventional wells routinely use multi-cluster "plug-and-perf" completions. **Fig. 8.1** shows an illustration of such a multi-cluster completion. In this type of completion, a fracturing stage is isolated from the previous stages by using a bridge plug. The stage length may vary from 30-170 m (100-500 ft). Usually there are 3-10 perforation clusters per stage, with a perforation density ranging from 2 to 4 shots per foot (SPF). These perforation clusters act as initiation points for the hydraulic fractures.

Many engineers and researchers make the simple assumption that each perforation cluster corresponds to a single planar fracture for that given stage. However, there is evidence from recent field studies that there can be multiple planar fractures parallel to each other in each perforation cluster. Given the complexity of the near-wellbore conditions, it is

extremely difficult to determine the exact number of fractures per cluster. In this study, I assume that a single hydraulic fracture will grow from each cluster.

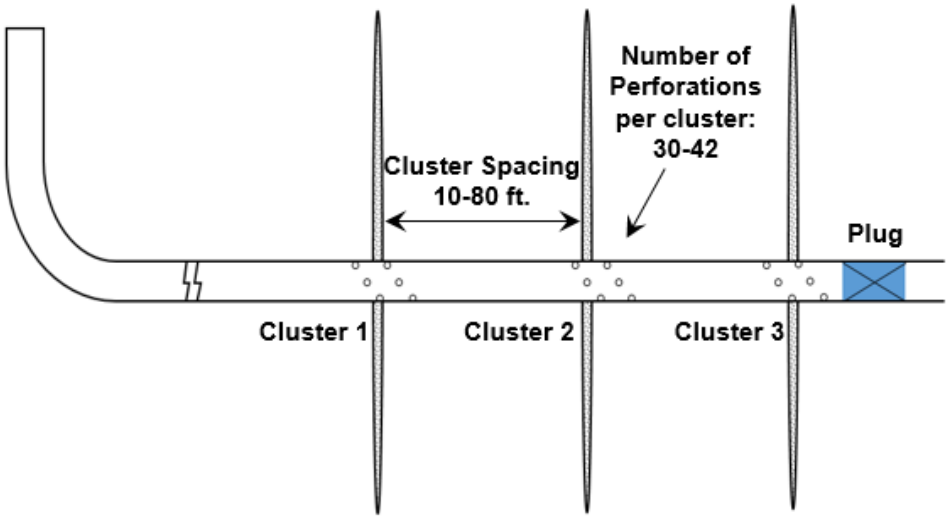

Figure 8.1 Illustration of a multi-cluster plug-and-perf completion design

During the hydraulic fracturing process, the proppant slurry is pumped into the casing and is diverted into a given cluster. However, there is considerable uncertainty as to how proppants are distributed among the clusters. A recent study (Carpenter et. al., 2018) has proposed the limited entry design, in which the perforation density at the heel of the wellbore is reduced to achieve a more even distribution in the toe section. With this topic being an active research area and with many questions still remaining unanswered, I extended my single fracture model to describe the multi-cluster wellbore-fracture model shown in **Fig. 8.2**

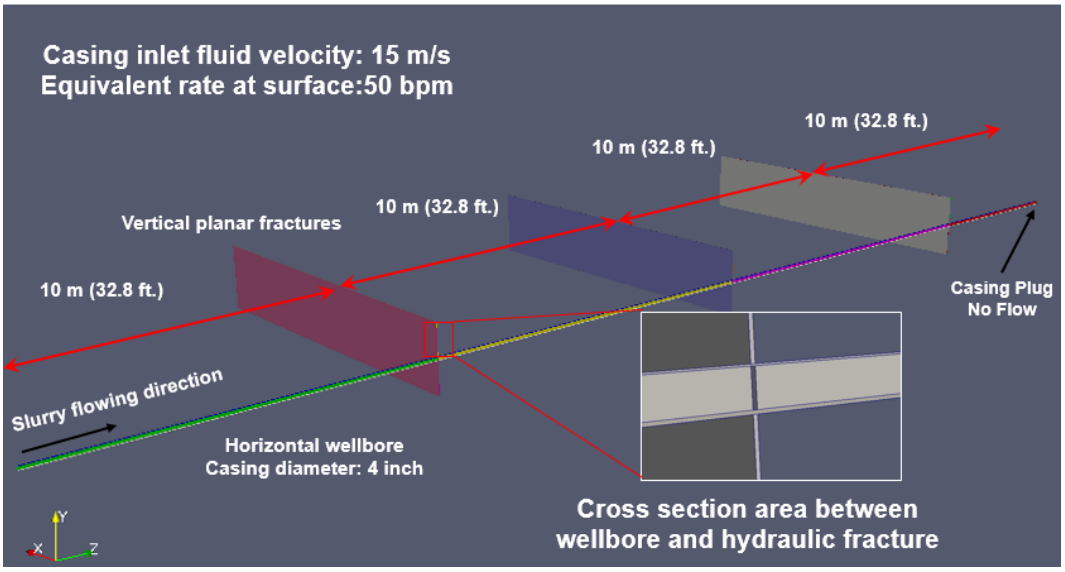

Figure 8.2 Visualization of the multi-cluster horizontal wellbore-fracture model, with the cross-section area illustrated.

The horizontal wellbore in this configuration is 40 m long, and is divided into 4 sections; each wellbore subsection is 10 m long. At the end of each 10 m subsection, the wellbore is connected to a vertical planar HF. The HF is 10 m long and 2 m high. The diameter of the wellbore is 4 inches. Using the cross-sectional area corresponding to a 4-inch casing, I calculated that a 50 bpm surface pumping rate corresponds to a fluid velocity of 15m/s in the casing.

8.2. Proppant and Fluid Distribution in Each of the Cluster

I conducted the CFD-DEM simulation of the multi-cluster model discussed in the previous subsection, and I analyzed the numerical results of the fluid and particle velocity profiles along the wellbore, as well as the percentage of proppant particles that entered each cluster. **Fig. 8.3** shows the fluid and particle velocities along the wellbore.

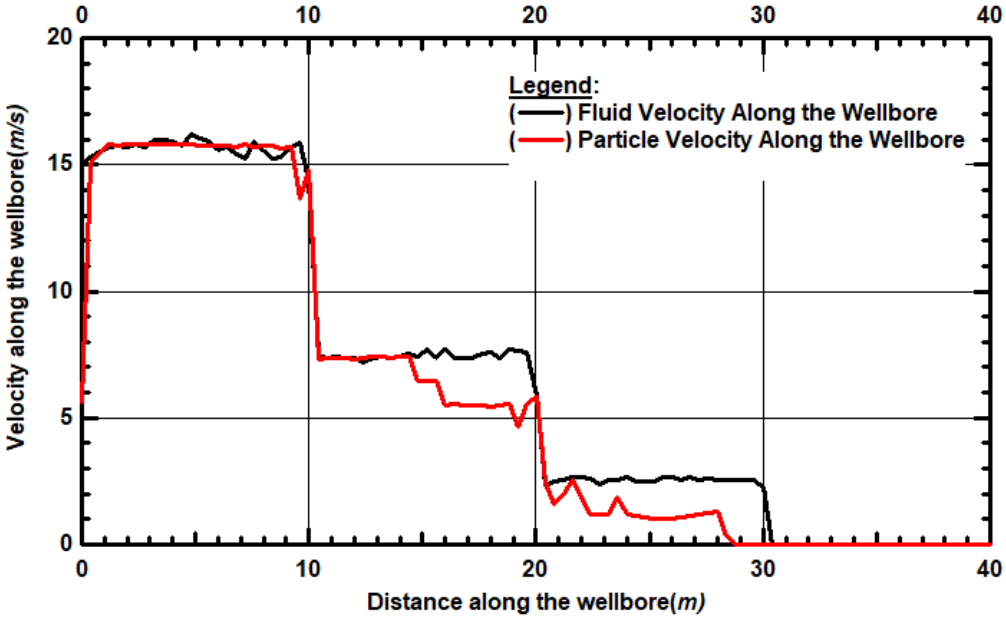

Figure 8.3 Fluid and particle velocity profiles along the horizontal wellbore when the slurry injection velocity V_{inlet} = 15 m/s

The stepwise pattern of the velocity profiles provides a clear indication of the fluid and particle entrance into the HF at each cluster. Integration of the volume under the fluid velocity curve leads to estimates of (a) 56.6% of the fluid entering the first cluster, (b) 27.2% of the fluid entering the second cluster and (c) 16.2% of the fluid entering the third cluster. *These results show a strong heal-toe effect*, in which the first cluster receives the largest amounts of fluid enter because of the larger initial pressure gradient at that location.

To determine the effect of the pumping rate on the fluid distribution, I plot the fluid and particle velocities for a V_{inlet} = 19 m/s (corresponding to a surface injection rate of 65 bpm) of slurry in the casing. **Fig. 8.4** shows the fluid and particle velocity profiles for this higher injection rate case. In this case, the integration calculations indicated that, moving from

heel to toe, the fractions of the fluid mass entering the 3 clusters are 49.3%, 32.4% and 18.3%, respectively.

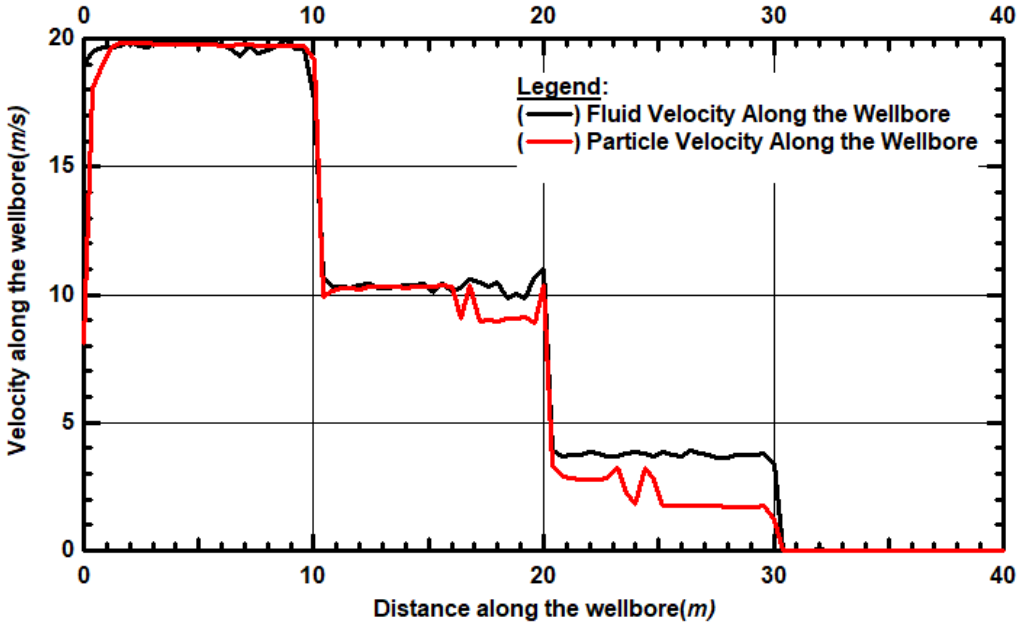

Figure 8.4 Fluid and particle velocity profiles along the horizontal wellbore when the slurry injection velocity V_{inlet} = 19 m/s

Compared to the slower injection rate case, the larger injection rate forces more fluid into the 2nd and 3rd clusters, but the 1st cluster takes slightly less fluid. The fraction of the injected fluid that enters the 1st cluster decreases from 56.6% to 49.3%, but this cluster one still takes about half of the fluid.

Fig. 8.5 shows the percentage of proppant particles entering the HF domains at the three clusters for three different injection rates. At Q_1 = 35 bpm (**Fig. 8.5a**), the proppant

distribution shows a significant heel bias: the majority of the proppant (43% of total in the clusters) entered the 1st cluster, and the least amount of proppant (18%) entered the 3rd cluster. At Q_2 = 50 bpm (**Fig. 8.5b**), less proppant (than that in Case Q_1) entered the 1st cluster, more proppant entered the 3rd cluster, and the 2nd cluster received the most proppant. At Q_3 = 65 bpm (**Fig. 8.5c**), the amount of the proppant that entered the first cluster decreased even more than those for the Q_1 and Q_2 injection rates, the proppant amount that entered the 3rd cluster increased even more, and the 2nd cluster received the most proppant, with the proppant distribution among 3 clusters becoming more even.

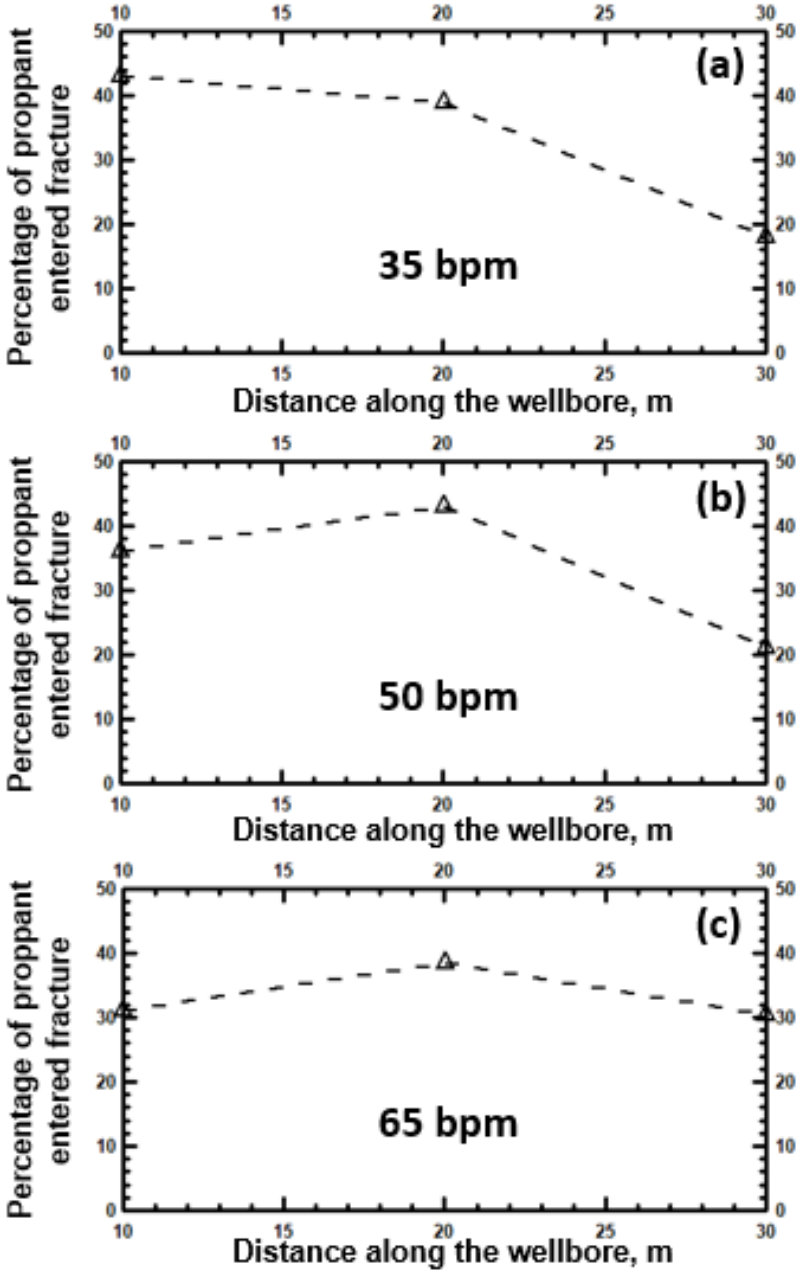

Figure 8.5 Particle distribution at three clusters located at 10m, 20m, 30m from the injection inlet: (a) Q1 = 35 bpm (b) Q2 = 50 bpm and (c) Q3 = 65 bpm

To better illustrate the changes in the proppant particle distribution when the pumping rate increases (from Q_1 = 35 bpm to Q_3 = 65 bpm), **Fig. 8.6** shows the percentage of the proppant in the 1st and 3rd clusters at the 3 different pumping rates.

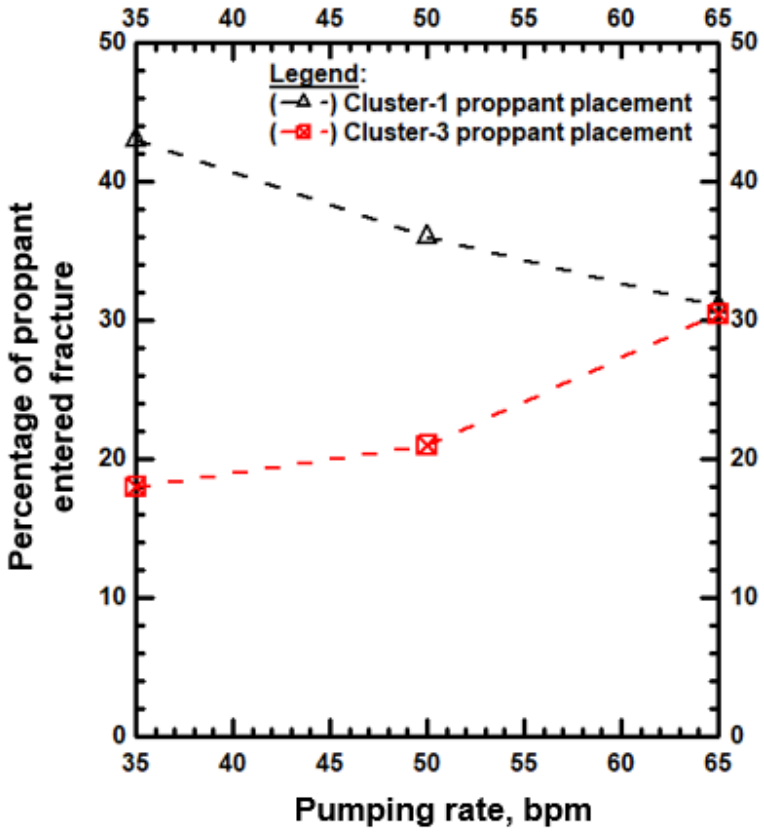

Figure 8.6 Particle distribution at the 1st and 3rd cluster at three pumping rates (Q_1 = 35 bpm, Q_2 = 50 bpm and Q_3 = 65 bpm)

Fig. 8.6 shows clearly that when the pumping rate increases, the percentage of proppant entering the 1st cluster decreases, while the proppant entering the 3rd cluster increases. This

is attributed to the higher particle velocity when the pumping rate increases, which reduces the time available to the particles to enter the window of the first cluster, thus leaving more proppant for the remaining clusters. In fact, I observed similar behavior in the study described in **Section 6.4**, in which proppant with a velocity above a certain threshold value will "skip" the window to enter a NF. In both cases, the simulation results show that there exists an optimal velocity for proppant particles to enter a subdomain, which could be from a horizontal wellbore to a HF subdomain, or from a HF to a NF subdomain. Of the three pumping rate that were considered, the Q_3 = 65 bpm injection rate case shows the most even distribution of the proppant among the three clusters. This observation agrees with current industry practices, in which the desirable pumping rate during multi-cluster fracturing is recommended to be larger than 70 bpm. High pumping rates reduce the settling of proppant particles, in addition to helping place more proppant into the far clusters in the toe of horizontal wells.

9. CONCLUSIONS

In this research, I conducted simulations of multiple cases of proppant transport using the coupled CFD-DEM method. Compared to other methods, the CFD-DEM method is more scientifically robust because it considers both particle-particle interactions and particle-boundary interactions. This enables the study of proppant transport in the following three challenging (and previously intractable) scenarios: (1) dipping fractures (2) the HF-NF intersections at sharp angles, and (3) multi-cluster fractures.

I believe that my numerical simulation studies of these three scenarios provide new insights into the subject of proppant transport and lead to the following conclusions:

1. Compared to vertical fractures, proppant transport in fractures with dipping angles is more efficient because of easier particle mobilization, resulting in a longer reach (deeper advance) into the HF. For the same inlet velocity, the suspension transport region in the dipping fractures extended further from the wellbore. Thus, when dipping angle decreases, the reach and placement efficiency of proppant particles increases. Our numerical experiments showed up to 40 percent improvement in placement efficiency in the dipping fractures.
2. The efficiency of proppant placement in a natural fracture(s) largely depends on the flow regime. When in the suspension regime (associated with high inlet velocities), the fluid drag force distributes proppant particles into the natural fractures. This can lead to a relatively high proppant placement efficiency in the natural fractures.
3. When in a bed-load transport regime (associated with low inlet velocities, or at

regions far away from the wellbore), the proppant placement efficiency in the natural fractures is much lower than that in a suspension regime. Because of the inter-particle collisions and large friction forces, the number of proppant particles entering secondary fractures and the distances that such particles can travel are limited compared to the case of suspension transport.

4. High inlet velocities are desired to achieve high proppant placement efficiency in the natural fracture. However, if the inlet velocity is larger than a threshold value (5 m/s for our simulated scenario), the placement efficiency in natural fracture starts to decrease. This is because proppant particles move too fast in the x-direction (*i.e.*, the main flow direction in the HF), thus reducing the probability of entering the NF window.

5. We proposed a bridging criterion based on a simple relationship of C_p and R_{fp}. This enables the estimation of the maximum C_p allowed for continuous proppant transport for a given R_{fp}. value. This criterion can be incorporated into a continuous proppant transport model for field-scale proppant transport simulations. The bridging criterion can also be used for engineering design calculation, and our criterion is consistent with empirical field practices, where around 1.0 PPA is the desired proppant concentration to avoid early screen out (*i.e.*, proppant bridging).

6. In a multi-cluster proppant transport scenario, a larger injection rate (faster fluid and particle velocity) helps achieve better (more uniform) proppant placement in the far clusters. Increasing the injection rate appears to lead to a more even proppant distribution among the clusters. This is due to the larger momentum of the proppant

particles, which helps carry proppant particles to the toe cluster and reduce the bias to the heel clusters.

REFERENCES

Ayachit, Utkarsh. The paraview guide: a parallel visualization application. Kitware, Inc., 2015.

Beugelsdijk, L. J. L., de Pater, C. J., & Sato, K. (2000, January 1). Experimental Hydraulic Fracture Propagation in a Multi-Fractured Medium. Society of Petroleum Engineers. doi:10.2118/59419-MS.

Bierwisch, Claas, et al. "Three-dimensional discrete element models for the granular statics and dynamics of powders in cavity filling." Journal of the Mechanics and Physics of Solids 57.1 (2009): 10-31.

Brannon, H. D., Wood, W. D., & Wheeler, R. S. (2006, January 1). Large Scale Laboratory Investigation of the Effects of Proppant and Fracturing Fluid Properties on Transport. Society of Petroleum Engineers. doi:10.2118/98005-MS

Carpenter, C. (2018, September 1). Extreme Limited-Entry Perforating Enhances Bakken Completions. Society of Petroleum Engineers. doi:10.2118/0918-0094-JPT

Chanson, Hubert.2004. Hydraulics of open channel flow. Elsevier.p-194

Chen, Xizhong, and Junwu Wang. 2014. "A comparison of two-fluid model, dense discrete particle model and CFD-DEM method for modeling impinging gas–solid flows." Powder Technology254 (2014): 94-102.

Christoph Kloss, Christoph Goniva, Alice Hager, Stefan Amberger, Stefan Pirker, "Models, algorithms and validation for opensource DEM and CFD-DEM", - Progress in Computational Fluid Dynamics, An Int. J. 2012 - Vol. 12, No.2/3 pp. 140 – 152

Chu, Kaiwei, Jiang Chen, and Aibing Yu. "Applicability of a coarse-grained CFD–DEM model on dense medium cyclone." Minerals Engineering 90 (2016): 43-54.

Duan, Zhipeng, Boshu He, and Yuanyuan Duan. "Sphere drag and heat transfer." Scientific reports 5 (2015): 12304.

Di Felice, Rosa. "The voidage function for fluid-particle interaction systems." International Journal of Multiphase Flow 20.1 (1994): 153-159.

Dinh, Anh V., and Djebbar Tiab. "Transient-pressure analysis of a well with an inclined hydraulic fracture using Tiab's Direct Synthesis Technique." SPE Production and Operations Symposium. Society of Petroleum Engineers, 2009.

Dontsov, E. V., and A. P. Peirce. 2014. "Slurry flow, gravitational settling and a proppant transport model for hydraulic fractures." Journal of Fluid Mechanics 760: 567-590.

Gu, Hongren, et al. "Hydraulic fracture crossing natural fracture at nonorthogonal angles: a criterion and its validation." SPE Production & Operations 27.01 (2012): 20-26.

Goniva, C., Kloss, C., Deen, N.G., Kuipers, J.A.M. and Pirker, S. (2012): “Influence of Rolling Friction Modelling on Single Spout Fluidized Bed Simulations”, Particuology, DOI 10.1016/j.partic.2012.05.002

Issa, Raad I. "Solution of the implicitly discretised fluid flow equations by operator-splitting." Journal of computational physics 62.1 (1986): 40-65.

Kafui, K. D., C. Thornton, and M. J. Adams. "Discrete particle-continuum fluid modelling of gas–solid fluidised beds." Chemical Engineering Science 57.13 (2002): 2395-2410.

King, G. E. (2010, January 1). Thirty Years of Gas Shale Fracturing: What Have We Learned? Society of Petroleum Engineers. doi:10.2118/133456-MS

King, R. Peter. Introduction to practical fluid flow. Elsevier, 2002.

Kou, R., G. J. Moridis, and T. A. Blasingame. 2018. "Analysis and Modeling of Proppant Transport in Inclined Hydraulic Fractures." SPE Hydraulic Fracturing Technology Conference and Exhibition. Society of Petroleum Engineers.

Kou, Rui, George J. Moridis, and Tom Blasingame. 2018. "Field Scale Proppant Transport Simulation and Its Application to Optimize Stimulation Strategy." Unconventional Resources Technology Conference (URTEC).

Kou, Rui, George Moridis, and Thomas Blasingame. "Bridging criteria and distribution correlation for proppant transport in primary and secondary fracture." SPE Hydraulic Fracturing Technology Conference and Exhibition. Society of Petroleum Engineers, 2019.

Lu, Liqiang, Aaron Morris, Tingwen Li, and Sofiane Benyahia. "Extension of a coarse grained particle method to simulate heat transfer in fluidized beds." International Journal of Heat and Mass Transfer 111 (2017): 723-735.

Mao*, Shaowen, et al. "An efficient three-dimensional multiphase particle-in-cell model for proppant transport in the field scale." Unconventional Resources Technology Conference, Denver, Colorado, 22-24 July 2019. Unconventional Resources Technology Conference (URTeC); Society of Exploration Geophysicists, 2019.

McClure, Mark. "Bed load proppant transport during slickwater hydraulic fracturing: Insights from comparisons between published laboratory data and correlations for sediment and pipeline slurry transport." Journal of Petroleum Science and Engineering 161 (2018): 599-610.

Medlin W.L., Sexton J.H., Zumwalt G.L., Sand transport experiments in thin fluids, The SPE Annual Technical Conference and Exhibition, Las Vegas, NV (1985)

Norouzi, Hamid Reza, et al. Coupled CFD-DEM modeling: formulation, implementation and application to multiphase flows. John Wiley & Sons, 2016.

Patankar, N. A., et al. "Power law correlations for sediment transport in pressure driven channel flows." International Journal of Multiphase Flow 28.8 (2002): 1269-1292.

Pye, Kenneth. 1994. Sediment transport and Depositional Processes. Oxford, UK, Blackwell Scientific Publications.

Raterman, Kevin T., et al. "Sampling a stimulated rock volume: an eagle ford example." Unconventional Resources Technology Conference, Austin, Texas, 24-26 July 2017. Society of Exploration Geophysicists, American Association of Petroleum Geologists, Society of Petroleum Engineers, 2017.

Sahai, Rakshit, Jennifer L. Miskimins, and Karen E. Olson. "Laboratory results of proppant transport in complex fracture systems." SPE Hydraulic Fracturing Technology Conference. Society of Petroleum Engineers, 2014.

Sakai, Mikio, et al. "Verification and validation of a coarse grain model of the DEM in a bubbling fluidized bed." Chemical Engineering Journal 244 (2014): 33-43.

Schiller, Links. "A drag coefficient correlation." Zeit. Ver. Deutsch. Ing. 77 (1933): 318-320.

Schmeeckle, Mark W., and Jonathan M. Nelson. 2003. "Direct numerical simulation of bedload transport using a local, dynamic boundary condition." Sedimentology 50.2: 279-301.

Shiozawa, S., & McClure, M. 2016. Comparison of Pseudo-3D and Fully-3D Simulations of Proppant Transport in Hydraulic Fractures, Including Gravitational Settling, Formation of Proppant Banks, Tip-Screen Out, and Fracture Closure. Society of Petr

Stevens, A. B., and C. M. Hrenya. "Comparison of soft-sphere models to measurements of collision properties during normal impacts." Powder Technology 154.2-3 (2005): 99-109.

Sun, Zhuang, D. Nicolas Espinoza, and Matthew T. Balhoff. "Discrete element modeling of indentation tests to investigate mechanisms of CO2 ‐ related chemomechanical rock alteration." Journal of Geophysical Research: Solid Earth 121.11 (2016): 7867-7881.

Sun, Zhuang, et al. "Discrete Element Modeling of Micro-scratch Tests: Investigation of Mechanisms of CO 2 Alteration in Reservoir Rocks." Rock Mechanics and Rock Engineering 50.12 (2017): 3337-3348.

Sun, Zhuang, Matthew T. Balhoff, and D. Nicolas Espinoza. "Fluid Injection Induced Fracture Initiation Based on a Resolved CFD-DEM Approach." 52nd US Rock

Mechanics/Geomechanics Symposium. American Rock Mechanics Association, 2018.

Sun, Zhuang, et al. "Discrete element modeling of grain crushing and implications on reservoir compaction." Journal of Petroleum Science and Engineering 171 (2018): 431-439.

Tang, Jizhou, et al. "Investigate effects of weak bedding interfaces on fracture geometry in unconventional reservoirs." Journal of Petroleum Science and Engineering 165 (2018): 992-1009.

Tang, Jizhou, et al. "Investigation of rupture and slip mechanisms of hydraulic fractures in multiple-layered formations." SPE Journal (2019).

Tran, T., Kim, J. Y., Morita, N., & Yoshimura, K. (2017, August 28). Application of PGA Fiber and Fluid-Loss Materials to Slick Water Fracturing. American Rock Mechanics Association.oleum Engineers. doi:10.2118/179132-MS

Tong, Songyang, Robin Singh, and Kishore K. Mohanty. "Proppant transport in fractures with foam-based fracturing fluids." SPE Annual Technical Conference and Exhibition. Society of Petroleum Engineers, 2017.

Velikanov, Ivan, et al. "New fracture hydrodynamics and in-situ kinetics model supports comprehensive hydraulic fracture simulation." SPE Europec featured at 80th EAGE Conference and Exhibition. Society of Petroleum Engineers, 2018.

Warpinski, N., Kramm, R. C., Heinze, J. R., & Waltman, C. K. 2005. Comparison of Single-and Dual-Array Microseismic Mapping Techniques in the Barnett Shale. Society of Petroleum Engineers. doi:10.2118/95568-MS

Wasp, Edward J., John P. Kenny, Ramesh L. Gandhi. 1977. Solid-Liquid Flow Slurry Pipeline Transportation. Clausthal, Germany, Trans Tech Publications.

Weinhart, Thomas, et al. "Influence of coarse-graining parameters on the analysis of DEM simulations of silo flow." Powder technology 293 (2016): 138-148.

Weller, H. G., Tabor G., Jasak H., Fureby C., A tensorial approach to computational continuum mechanics using object-oriented techniques, COMPUTERS IN PHYSICS, VOL. 12, NO. 6, NOV/DEC 1998.

Weng, Xiaowei, et al. 2011. "Modeling of hydraulic fracture network propagation in a naturally fractured formation." SPE Hydraulic Fracturing Technology Conference. Society of Petroleum Engineers.

Wright, C. A., et al. "Surface Tiltmeter Fracture Mapping Reaches New Depths-10,000 Feet and Beyond?." SPE Rocky Mountain Regional/Low-Permeability Reservoirs Symposium. Society of Petroleum Engineers, 1998.

Wu, K., & Olson, J. E. (2016, June 1). Mechanisms of Simultaneous Hydraulic-Fracture Propagation From Multiple Perforation Clusters in Horizontal Wells. Society of Petroleum Engineers. doi:10.2118/178925-PA

Zhang, Fan, et al. "Upscaling Laboratory Result of Surfactant-Assisted Spontaneous Imbibition to the Field Scale through Scaling Group Analysis, Numerical Simulation,

and Discrete Fracture Network Model." SPE Improved Oil Recovery Conference. Society of Petroleum Engineers, 2018.

Zhang, Fan, et al. "Numerical Investigation of EOR Applications in Unconventional Liquid Reservoirs through Surfactant-Assisted Spontaneous Imbibition SASI and Gas Injection Following Primary Depletion." SPE Annual Technical Conference and Exhibition. Society of Petroleum Engineers, 2019.

APPENDIX A

Derivation of Model A Formulation Of CFD-DEM Model

The mass and momentum conservation for the fluid phase are described by:

$$\frac{\partial(\rho\varepsilon_f)}{\partial t} + \nabla \cdot \left(\rho\overrightarrow{u_f}\right) = 0 \quad \text{..... (A.1)}$$

$$\rho\frac{\partial(\varepsilon_f\overrightarrow{u_f})}{\partial t} + \rho[\overrightarrow{u_f} \cdot \nabla\left(\varepsilon_f\overrightarrow{u_f}\right)] = \nabla \cdot \overleftrightarrow{\sigma} - \frac{1}{V_{cell}}\sum_{i=1}^{kv}\vec{f}_i^{f-p} + \rho\varepsilon_f\vec{g} \quad \text{..... (A.2)}$$

where $\boldsymbol{\rho}$ is the fluid density in kg/m^3; $\overrightarrow{\mathbf{u_f}}$ is the fluid velocity in m/s; $\boldsymbol{\mu_f}$is the fluid viscosity in poise; $\boldsymbol{\varepsilon_f}$ is the volume fraction of fluid; $\vec{\boldsymbol{f}}_{\boldsymbol{i}}^{\boldsymbol{f-p}}$is the fluid-to-particle force for particle i, in N; $\boldsymbol{kv}$ is the number of particles in the corresponding fluid cell; and $\boldsymbol{V_{cell}}$ is the volume of the fluid cell, in m^3.

The fluid-to-particle force ($\vec{\boldsymbol{f}}_{\boldsymbol{i}}^{\boldsymbol{f-p}}$) is the coupling term between the particle phase and the fluid phase. It contains (but is not limited to) the pressure gradient force, the fluid drag force and the fluid shear force. Instead of computing each of the component forces listed above, one can use the following derivation to simplify the coupling term ($\vec{\boldsymbol{f}}_{\boldsymbol{i}}^{\boldsymbol{f-p}}$). First, we expand the Cauchy stress tensor in Eq. 4 as follows:

$$\rho\frac{\partial(\varepsilon_f u_x)}{\partial t} + \rho[\overrightarrow{u_f} \cdot \nabla\left(\varepsilon_f\overrightarrow{u_f}\right)] = [\nabla \cdot \left(-p\overleftrightarrow{I} + \overleftrightarrow{\tau}\right)] - \frac{1}{V_{cell}}\sum_{i=1}^{kv}\vec{f}_i^{f-p} + \varepsilon_f\vec{g} \quad \text{..... (A.3)}$$

The summation of the force terms on the right-hand side can be expanded as (Crowe, et. al., 2011):

$$\frac{1}{\mathbf{V_{cell}}}\sum_{\mathbf{i=1}}^{\mathbf{kv}}\vec{\mathbf{f}}_{\mathbf{i}}^{\mathbf{f-p}} = \frac{1}{\mathbf{V_{cell}}}\sum_{\mathbf{i=1}}^{\mathbf{kv}}(-\mathbf{V_i}\nabla\mathbf{p} + \mathbf{V_i}\overleftrightarrow{\boldsymbol{\tau}} + \vec{\mathbf{f}}_{\mathbf{i}}^{\mathbf{d}}) = -\boldsymbol{\varepsilon}_{\mathbf{p}}\nabla\mathbf{p} + \boldsymbol{\varepsilon}_{\mathbf{p}}\nabla\cdot\overleftrightarrow{\boldsymbol{\tau}} + \frac{1}{\mathbf{V_{cell}}}\sum_{\mathbf{i=1}}^{\mathbf{kv}}\left(\vec{\mathbf{f}}_{\mathbf{i}}^{\mathbf{d}}\right) \quad \text{..... (A.4)}$$

where $\boldsymbol{\varepsilon_p}$ is the volume fraction of all particles in the fluid cell; $\boldsymbol{V_i}$ is the volume (in m^3) of particle i; $\overleftrightarrow{\boldsymbol{\tau}}$ is the shear stress of the fluid (in N/m^2); and $\boldsymbol{\varepsilon_p}$=1-$\boldsymbol{\varepsilon_f}$ is the volume fraction of the particles in the fluid cell.

Combining Eq. A.3 and A.4, we obtain the final momentum conservation equation for the fluid phase:

$$\rho\frac{\partial(\varepsilon_f\overrightarrow{u_f})}{\partial t}+\rho[\overrightarrow{u_f}\cdot\nabla(\varepsilon_f\overrightarrow{u_f})]=-\varepsilon_f\nabla p+\varepsilon_f\nabla\cdot\overleftrightarrow{\tau}+\rho\varepsilon_f\vec{g}-\frac{1}{V_{cell}}\sum_{i=1}^{kv}(\vec{f}_i^{\,d}) \quad \text{..... (A.5)}$$

The advantage of using Eq. A.5 is that, by canceling the pressure gradient and the shear stress components of $\vec{\boldsymbol{f}}_{\boldsymbol{i}}^{\boldsymbol{f-p}}$, the fluid and the particle momentum conservation equations (Eq. 1 and 4) are coupled through the drag force term ($\vec{\boldsymbol{f}}_{\boldsymbol{i}}^{\boldsymbol{d}}$) only. This reduces the computational effort, as well as the memory required for coupling the CFD and the *DEM* simulations. Eq. A.5 is often referred to as the "Model A" formulation of the coupled CFD-DEM simulation. To implement the Model A formulation in a 3-dimensional simulation, one can further derive Eq. A.5 in the rectangular Cartesian coordinate system. Taking the x-component as an example:

$$\frac{\partial(\varepsilon_f u_x)}{\partial t}+\nabla\cdot\left(\varepsilon_f u_x\overrightarrow{u_f}\right)-\varepsilon_f u_x(\nabla\cdot\overrightarrow{u_f})=-\frac{1}{\rho}\varepsilon_f[\nabla p]_x+\frac{1}{\rho}\left[\nabla\cdot\left(\varepsilon_f\overleftrightarrow{\tau}\right)\right]_x+\varepsilon_f g_x-\frac{1}{V_{cell}}\sum_{i=1}^{kv}([\vec{f}_i^{\,d}]_x) \quad \text{(A.6)}$$

From the equation of mass conservation of an incompressible fluid, for which $(\nabla\cdot\overrightarrow{\mathbf{u_f}})=\mathbf{0}$, we have:

$$\frac{\partial(\varepsilon_f u_x)}{\partial t}+\nabla\cdot\left(\varepsilon_f u_x\overrightarrow{u_f}\right)=-\frac{1}{\rho}\frac{\partial p}{\partial x}+\frac{1}{\rho}\left[\nabla\cdot\left(\varepsilon_f\overleftrightarrow{\tau}\right)\right]_x+\varepsilon_f g_x-\frac{1}{V_{cell}}\sum_{i=1}^{kv}([\vec{f}_i^{\,d}]_x) \quad \text{..... (A.7)}$$

where

$$\nabla \cdot \left(\varepsilon_f \mathbf{u_x} \overrightarrow{\mathbf{u_f}}\right) = \left[\frac{\partial}{\partial x}, \frac{\partial}{\partial y}, \frac{\partial}{\partial z}\right] \begin{bmatrix} \varepsilon_f \mathbf{u_x u_x} \\ \varepsilon_f \mathbf{u_x u_y} \\ \varepsilon_f \mathbf{u_x u_z} \end{bmatrix} = \frac{\partial \varepsilon_f \mathbf{u_x u_x}}{\partial x} + \frac{\partial \varepsilon_f \mathbf{u_x u_y}}{\partial y} + \frac{\partial \varepsilon_f \mathbf{u_x u_z}}{\partial z}$$

$$\frac{1}{\rho}\left[\nabla \cdot \left(\varepsilon_f \overleftrightarrow{\tau}\right)\right]_x = \frac{1}{\rho}\left[\left[\frac{\partial}{\partial x}, \frac{\partial}{\partial y}, \frac{\partial}{\partial z}\right] \varepsilon_f \begin{bmatrix} \tau_{xx} & \tau_{xy} & \tau_{xz} \\ \tau_{yx} & \tau_{yy} & \tau_{yz} \\ \tau_{zx} & \tau_{zy} & \tau_{zz} \end{bmatrix}\right]_x = \frac{1}{\rho}\begin{bmatrix} \frac{\partial \varepsilon_f \tau_{xx}}{\partial x} + \frac{\partial \varepsilon_f \tau_{xy}}{\partial y} + \frac{\partial \varepsilon_f \tau_{xz}}{\partial z} \\ \frac{\partial \varepsilon_f \tau_{yx}}{\partial x} + \frac{\partial \varepsilon_f \tau_{yy}}{\partial y} + \frac{\partial \varepsilon_f \tau_{yz}}{\partial z} \\ \frac{\partial \varepsilon_f \tau_{zx}}{\partial x} + \frac{\partial \varepsilon_f \tau_{zy}}{\partial y} + \frac{\partial \varepsilon_f \tau_{zz}}{\partial z} \end{bmatrix}_x = \frac{1}{\rho}\left(\frac{\partial \varepsilon_f \tau_{xx}}{\partial x} + \frac{\partial \varepsilon_f \tau_{xy}}{\partial y} + \frac{\partial \varepsilon_f \tau_{xz}}{\partial z}\right)$$

After multiplying the operator, the final form of the momentum balance equation (on the X direction) becomes:

$$\frac{\partial\left(\varepsilon_f \mathbf{u_x}\right)}{\partial t} + \frac{\partial \varepsilon_f \mathbf{u_x u_x}}{\partial x} + \frac{\partial \varepsilon_f \mathbf{u_x u_y}}{\partial y} + \frac{\partial \varepsilon_f \mathbf{u_x u_z}}{\partial z} =$$

$$-\frac{1}{\rho}\frac{\partial p}{\partial x} + \frac{1}{\rho}\left(\frac{\partial \varepsilon_f \tau_{xx}}{\partial x} + \frac{\partial \varepsilon_f \tau_{xy}}{\partial y} + \frac{\partial \varepsilon_f \tau_{xz}}{\partial z}\right) - \frac{1}{V_{cell}}\sum_{i=1}^{kv}([\vec{f}_i^d]_x) + \varepsilon_f \mathbf{g_x} \quad \text{(A.8)}$$

To obtain the momentum balance equation on other directions, simply replace the index of the primary variable (u_x) in by y and z.

$$\frac{\partial\left(\varepsilon_f \mathbf{u_y}\right)}{\partial t} + \frac{\partial \varepsilon_f \mathbf{u_y u_x}}{\partial x} + \frac{\partial \varepsilon_f \mathbf{u_y u_y}}{\partial y} + \frac{\partial \varepsilon_f \mathbf{u_y u_z}}{\partial z} =$$

$$-\frac{1}{\rho}\frac{\partial p}{\partial y} + \frac{1}{\rho}\left(\frac{\partial \varepsilon_f \tau_{yx}}{\partial x} + \frac{\partial \varepsilon_f \tau_{yy}}{\partial y} + \frac{\partial \varepsilon_f \tau_{yz}}{\partial z}\right) - \frac{1}{V_{cell}}\sum_{i=1}^{kv}([\vec{f}_i^d]_y) + \varepsilon_f \mathbf{g_y} \quad \text{(A.9)}$$

$$\frac{\partial\left(\varepsilon_f \mathbf{u_z}\right)}{\partial t} + \frac{\partial \varepsilon_f \mathbf{u_z u_x}}{\partial x} + \frac{\partial \varepsilon_f \mathbf{u_z u_y}}{\partial y} + \frac{\partial \varepsilon_f \mathbf{u_z u_z}}{\partial z} =$$

$$-\frac{1}{\rho}\frac{\partial p}{\partial z} + \frac{1}{\rho}\left(\frac{\partial \varepsilon_f \tau_{zx}}{\partial x} + \frac{\partial \varepsilon_f \tau_{zy}}{\partial y} + \frac{\partial \varepsilon_f \tau_{zz}}{\partial z}\right) - \frac{1}{V_{cell}}\sum_{i=1}^{kv}([\vec{f}_i^d]_z) + \varepsilon_f \mathbf{g_z} \quad \text{(A.10)}$$

APPENDIX B

INPUT,MESHING AND COMPILATION CODE

B.1. Input Code for DEM Simulator LIGGGHTS

```
echo            both
log             ../DEM/log.liggghts
thermo_log      ../DEM/post/thermo.txt

atom_style      granular
atom_modify     map array sort 0 0
communicate     single vel yes

boundary        f
newton          off

units           si

region          reg block 0 10 -1 1 0 0.1 units box
create_box      1 reg

neighbor        0.003 bin
neigh_modify    delay 0 binsize 0.01


# Material properties required for granular pair styles
fix         m1 all property/global youngsModulus peratomtype 5.e6
fix         m2 all property/global poissonsRatio peratomtype 0.45
fix         m3 all property/global coefficientRestitution
peratomtypepair 1 0.3
fix         m4 all property/global coefficientFriction
peratomtypepair 1 0.5
#fix         m5 all property/global characteristicVelocity scalar
2.0

# pair style
pair_style  gran model hertz tangential history # hertz without
cohesion
pair_coeff  * *

# timestep, gravity
timestep    0.00001
fix         gravi all gravity 9.8 vector 0.0 -1.0 0.0
```

```
# walls
fix     xwalls1 all wall/gran model hertz tangential history
primitive type 1 xplane 0
fix     xwalls2 all wall/gran model hertz tangential history
primitive type 1 xplane 10
fix     ywalls1 all wall/gran model hertz tangential history
primitive type 1 yplane -1.0
fix     ywalls2 all wall/gran model hertz tangential history
primitive type 1 yplane 1.0
fix     zwalls1 all wall/gran model hertz tangential history
primitive type 1 zplane 0.05
fix     zwalls2 all wall/gran model hertz tangential history
primitive type 1 zplane 0.06

# create single partciles
region      bc block 0 0.5 0 0.1 0.05 0.06 units box
fix                 pts1 all particletemplate/sphere 15485863
atom_type 1 density constant 2650 radius constant 0.005
fix                 pdd1 all particledistribution/discrete
15485867  1 pts1 1.0

fix             ins all insert/rate/region seed 32452843
distributiontemplate pdd1 vel constant 1 0 0 nparticles 1500000
particlerate 15000 insert_every 100 overlapcheck yes region bc

# cfd coupling
fix     cfd all couple/cfd couple_every 100 mpi
fix     cfd2 all couple/cfd/force

# apply nve integration to all particles that are inserted as
single particles
fix         integr all nve/sphere

# screen output
compute         rke all erotate/sphere
thermo_style    custom step atoms ke c_rke vol
thermo          1000
thermo_modify   lost ignore norm no
compute_modify  thermo_temp dynamic yes

# insert the first particles so that dump is not empty
run     0
dump    dmp all custom 10000 ../DEM/post/dump.liggghts_run id type
x y z ix iy iz vx vy vz fx fy fz omegax omegay omegaz radius

run     0 upto
```

B.2. Meshing Code for CFD Simulator OpenFOAM

```
FoamFile
{
    version     2.0;
    format      ascii;
    class       dictionary;
    object      blockMeshDict;
}
// * * * * * * * * * * * * * * * * * * * * * * * * * * * * * * * * * * * * *
* * * * * //

convertToMeters 1;

vertices
(
    (0 0 0)
    (10 0 0)
    (10 0.1 0)
    (0 0.1 0)
    (0 0 0.1)
    (10 0 0.1)
    (10 0.1 0.1)
    (0 0.1 0.1)
    (10 1 0)
    (0 1 0)
    (10 1 0.1) //10
    (0 1 0.1)
    (0 -1 0)
    (10 -1 0)
    (0 -1 0.1)
    (10 -1 0.1)
    (-0.1 0 0)
    (-0.1 0.1 0)
    (-0.1 0 0.1)
    (-0.1 0.1 0.1)

);
blocks
(
    hex (0 1 2 3 4 5 6 7) (100 1 1) simpleGrading (1 1 1)
    hex (3 2 8 9 7 6 10 11) (100 9 1) simpleGrading (1 1 1)
    hex (12 13 1 0 14 15 5 4) (100 10 1) simpleGrading (1 1 1)
    hex (16 0 3 17 18 4 7 19) (1 1 1) simpleGrading (1 1 1)
);
```

```
boundary
(
    inlet
    {
        type patch;
        faces
        (
            (17 16 18 19)
        );
    }
    outlet
    {
        type patch;
        faces
        (
            (2 8 10 6)
            (1 2 6 5)
            (13 1 5 15)
        );
    }
    walls
    {
        type wall;
        faces
        (
            (3 7 11 9)
            (12 14 4 0)
            (9 11 10 8)
            (12 13 15 14)
            (17 19 7 3)
            (16 0 4 18)
            (19 18 4 7)
            (17 3 0 16)
            (9 8 2 3 )
            (3 2 1 0)
            (0 1 13 12)
            (10 11 7 6)
            (4 5 6 7)
            (14 15 5 4)
         );
    }
);

mergePatchPairs
(
);
```

B.3. Compilation Bash Script for compiling CFDEM on Ada cluster

```
#!/bin/bash

module purge
export LD_LIBRARY_PATH=/software/lsf/9.1/linux2.6-glibc2.3-
x86_64/lib
module load Boost/1.61.0-intel-2016a
_PWD=$(pwd)

_FOAM_DIST=OpenFOAM-v3.0+
_THIRD_DIST=ThirdParty-v3.0+
export FOAM_INST_DIR=/software/tamuhprc/OpenFOAM


export MPI_ROOT=$I_MPI_ROOT  # must appear before source the
following file for it to be correctly sourced
source $FOAM_INST_DIR/${_FOAM_DIST}/etc/bashrc
export CC=mpiicc    # the following four variables must be set
after source foam_basrc
export CXX=mpiicpc
export WM_CXX=mpiicpc
export WM_CC=mpiicc
export BOOST_ARCH_PATH=$EBROOTBOOST          #needed by CGAL. Must
be built on login7 to have neccessary system libraries
export
ParaView_DIR=$FOAM_INST_DIR/${_THIRD_DIST}/platforms/linux64Icc/Pa
raView-4.4.0
export PATH=$ParaView_DIR/bin:$PATH
export PV_PLUGIN_PATH=$FOAM_LIBBIN/paraview-4.4

_CFDEM_VER=3.5.1
_LIGGGHTS_VER=3.5.0
_CFDEM_DIST=CFDEMcoupling-PUBLIC-${_CFDEM_VER}
CFDEM_ROOT=${_PWD}/${_CFDEM_DIST}
_LIGGGHTS_DIST=LIGGGHTS-PUBLIC-${_LIGGGHTS_VER}
LIGGGHTS_ROOT=${CFDEM_ROOT}/${_LIGGGHTS_DIST}
_LPP_DIST=LPP
LPP_ROOT=${CFDEM_ROOT}/${_LPP_DIST}

export LD_LIBRARY_PATH=$LIGGGHTS_ROOT/src:$LD_LIBRARY_PATH
export
LD_LIBRARY_PATH=$WM_PROJECT_USER_DIR/platforms/linux64IccDPInt32Op
t/lib:$LD_LIBRARY_PATH
```

```
if [ ! -d $CFDEM_ROOT ]; then
    git clone git://github.com/CFDEMproject/CFDEMcoupling-
PUBLIC.git ${_CFDEM_DIST}
    cd $CFDEM_ROOT
    git checkout tags/${_CFDEM_VER}
fi

cd $CFDEM_ROOT
if [ ! -d $LIGGGHTS_ROOT ]; then
    git clone git://github.com/CFDEMproject/LIGGGHTS-PUBLIC.git
${_LIGGGHTS_DIST}
    cd $LIGGGHTS_ROOT
    git checkout tags/${_LIGGGHTS_VER}
fi

CD $CFDEM_ROOT
if [ ! -d $LPP_ROOT ]; then
    git clone git://github.com/CFDEMproject/LPP
fi
cd $LIGGGHTS_ROOT/src
# patch MAKE/Makefile.mkl
LIBGGGHTS_MAKEMKL=$LIGGGHTS_ROOT/src/MAKE/Makefile.mkl
if [ ! -f ${LIBGGGHTS_MAKEMKL}.orig ]; then
    cp $LIBGGGHTS_MAKEMKL ${LIBGGGHTS_MAKEMKL}.orig
fi
cp ${LIBGGGHTS_MAKEMKL}.orig $LIBGGGHTS_MAKEMKL
sed -i 's/LINKFLAGS =.*/LINKFLAGS =   -mkl=sequential/'
$LIBGGGHTS_MAKEMKL
sed -i 's/LIB =.*/LIB = /'
$LIBGGGHTS_MAKEMKL
sed -i 's/FFT_INC =.*/FFT_INC = -DFFT_MKL/'
$LIBGGGHTS_MAKEMKL
sed -i 's/FFT_PATH =.*/#FFT_PATH = /'
$LIBGGGHTS_MAKEMKL
sed -i 's/FFT_LIB =.*/#FFT_LIB = /'
$LIBGGGHTS_MAKEMKL
make -j 8 mkl        # build the executable lmp_mkl and static
library liblmp_mkl.a
make makeshlib       # make shared library makefile
make -j 8 -f Makefile.shlib mkl     # build shared libary
liblammps_mkl.so

# make a symbolic link of the shared library
ln -sf liblammps_mkl.so liblmp_mkl.so
export PATH=$LIGGGHTS_ROOT/src:$PATH
```

```
cd $CFDEM_ROOT
cp $(dirname $0)/cfdem_setup.bashrc .
# make a symbolic link for mpic++
ln -s $(which mpiicpc) mpic++
export PATH=$(pwd):$PATH            # path for mpic++


export CFDEM_PROJECT_DIR=$CFDEM_ROOT
export CFDEM_SRC_DIR=$CFDEM_PROJECT_DIR/src
export CFDEM_SOLVER_DIR=$CFDEM_PROJECT_DIR/applications/solvers
export CFDEM_DOC_DIR=$CFDEM_PROJECT_DIR/doc
export CFDEM_UT_DIR=$CFDEM_PROJECT_DIR/applications/utilities
export CFDEM_TUT_DIR=$CFDEM_PROJECT_DIR/tutorials
export CFDEM_PROJECT_USER_DIR=$CFDEM_ROOT/user
export
CFDEM_bashrc=$CFDEM_SRC_DIR/lagrangian/cfdemParticle/etc/bashrc
export
CFDEM_LIGGGHTS_SRC_DIR=$CFDEM_PROJECT_DIR/$_LIGGGHTS_DIST/src
export CFDEM_LIGGGHTS_MAKEFILE_NAME=mkl
export CFDEM_LPP_DIR=$LPP_ROOT/src
export CFDEM_PIZZA_DIR=$LPP_ROOT/src
if [ ! -d $CFDEM_PROJECT_USER_DIR ]; then
    mkdir $CFDEM_PROJECT_USER_DIR
fi

# patch files
#sed -i 's/WM_PROJECT_VERSION == 3\.0\.\*/WM_PROJECT_VERSION ==
v3\.0\+/' $CFDEM_bashrc
if [ ! -f ${CFDEM_bashrc}.orig ]; then
    cp $CFDEM_bashrc ${CFDEM_bashrc}.orig
fi
cp ${CFDEM_bashrc}.orig $CFDEM_bashrc
sed -i "s/WM_PROJECT_VERSION == 3\.0\.\*/WM_PROJECT_VERSION ==
$WM_PROJECT_VERSION/" $CFDEM_bashrc
ETCDIR=$(dirname $CFDEM_bashrc)
cp -f $ETCDIR/additionalLibs_3.0.x
$ETCDIR/additionalLibs_$WM_PROJECT_VERSION
sed -i 's/-lmpi_cxx/#-lmpi_cxx/'
$ETCDIR/additionalLibs_$WM_PROJECT_VERSION
sed -i 's/$logpath\/grep \*\.tempXYZ/grep $logpath\/\*\.tempXYZ/'
$ETCDIR/compileCFDEMcoupling_sol.sh
sed -i 's/$logpath\/grep \*\.tempXYZ/grep $logpath\/\*\.tempXYZ/'
$ETCDIR/compileCFDEMcoupling_uti.sh
. $CFDEM_bashrc

$ETCDIR/compileCFDEMcoupling.sh
```

APPENDIX C

PARTICLE VELOCITY PLOT FOR VARIOUS INLET VELOCITY CASES

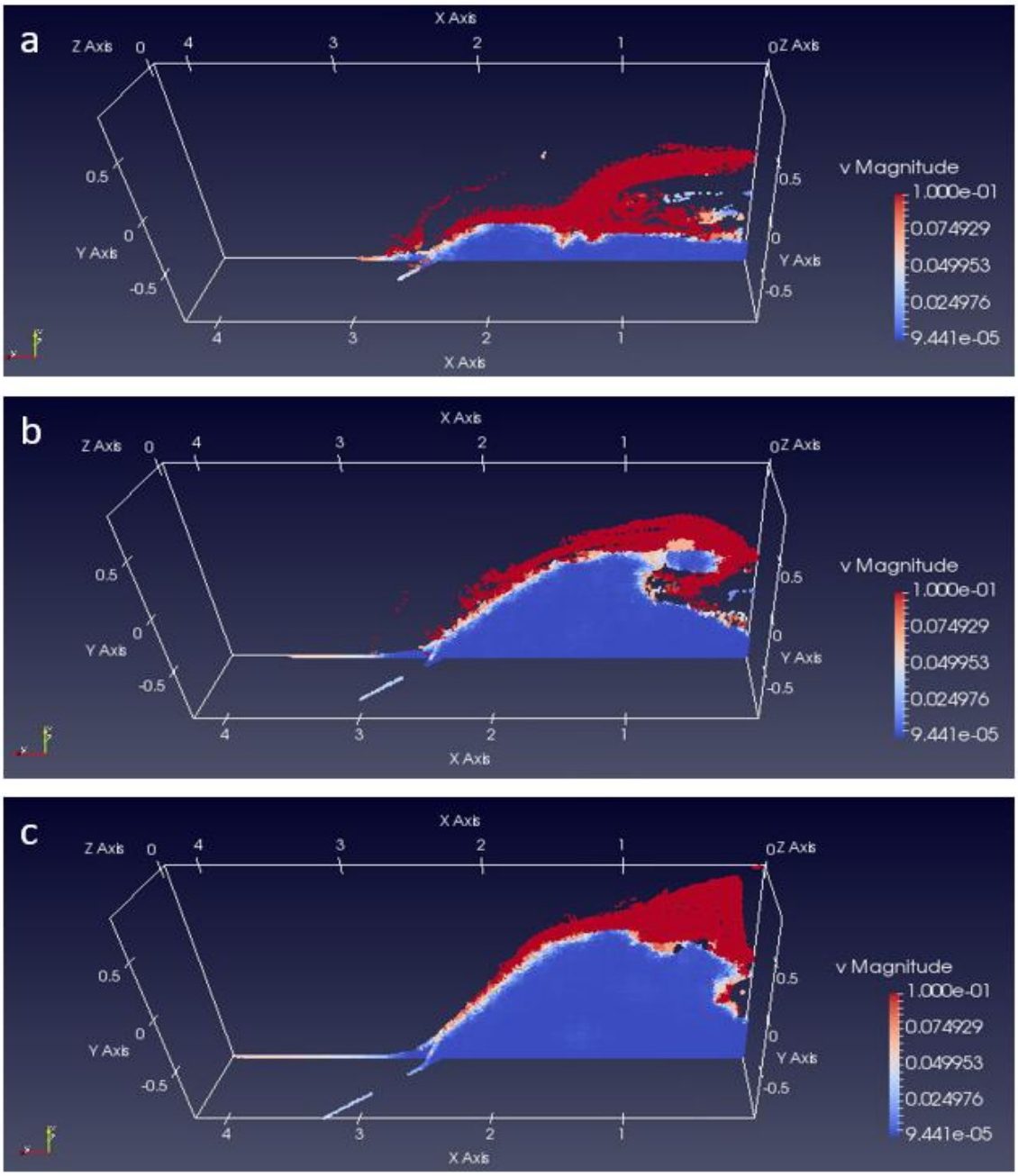

Figure C.1 Visualization of particle distribution for the case of inlet velocity of 2.0m/s at (a) t=100s, (b) t=200s and (c) t=300s

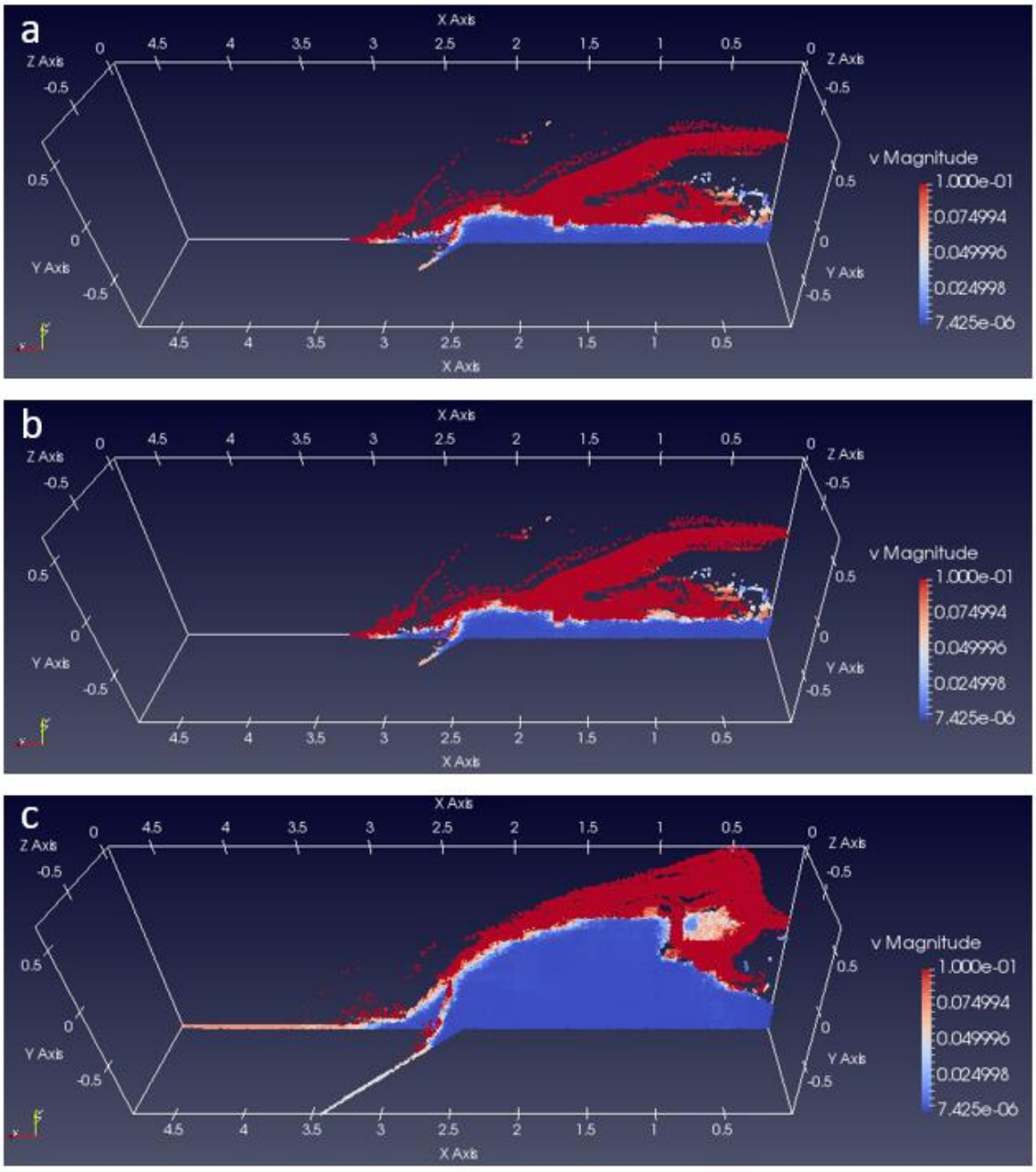

Figure Error! No text of specified style in document**..2 Visualization of particle distribution for the case of inlet velocity of 2.5m/s at (a) t=100s, (b) t=200s and (c) t=270s**

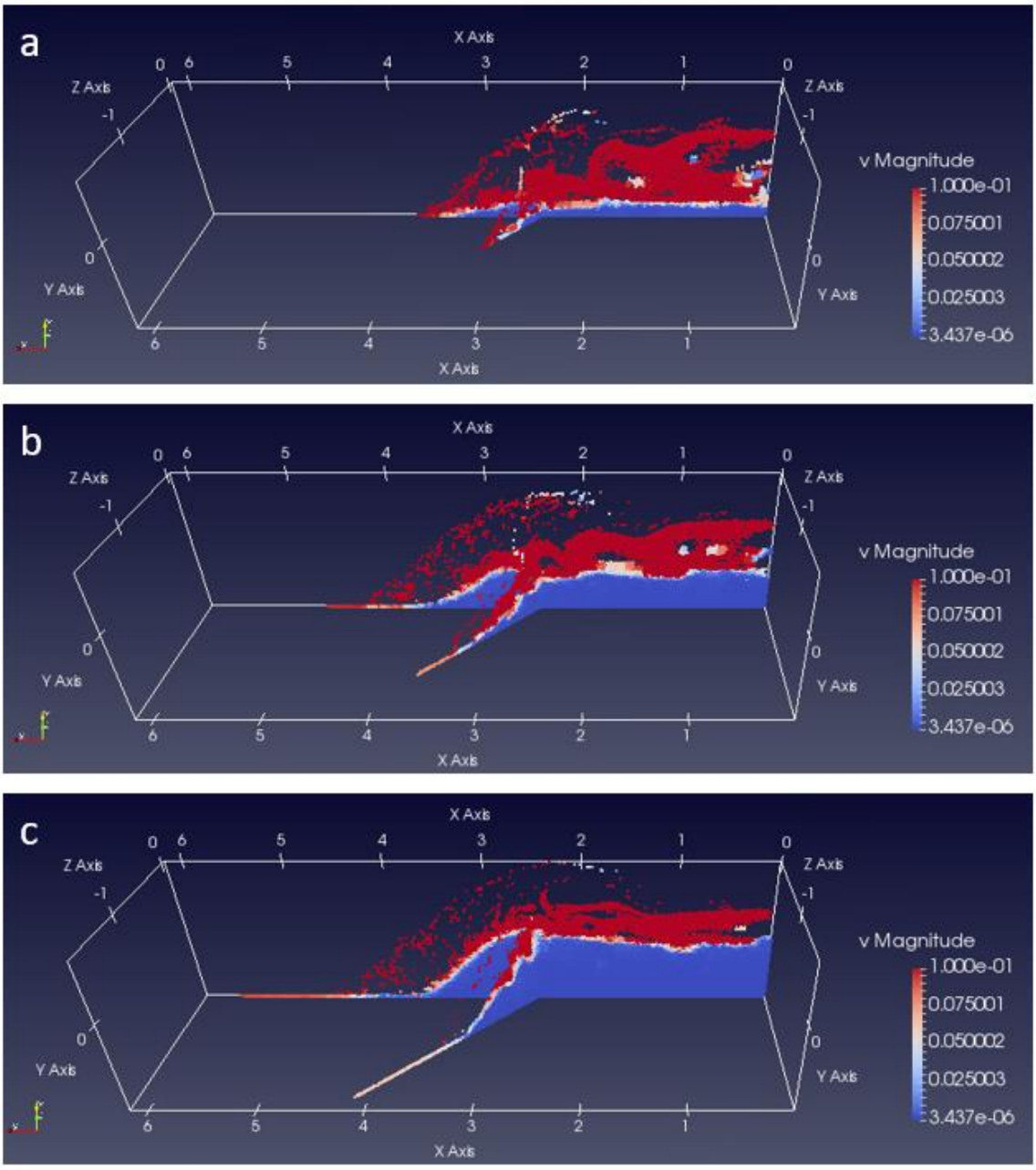

Figure C.3 Visualization of particle distribution for the case of inlet velocity of 3.0m/s at (a) t=100s, (b) t=200s and (c) t=300s

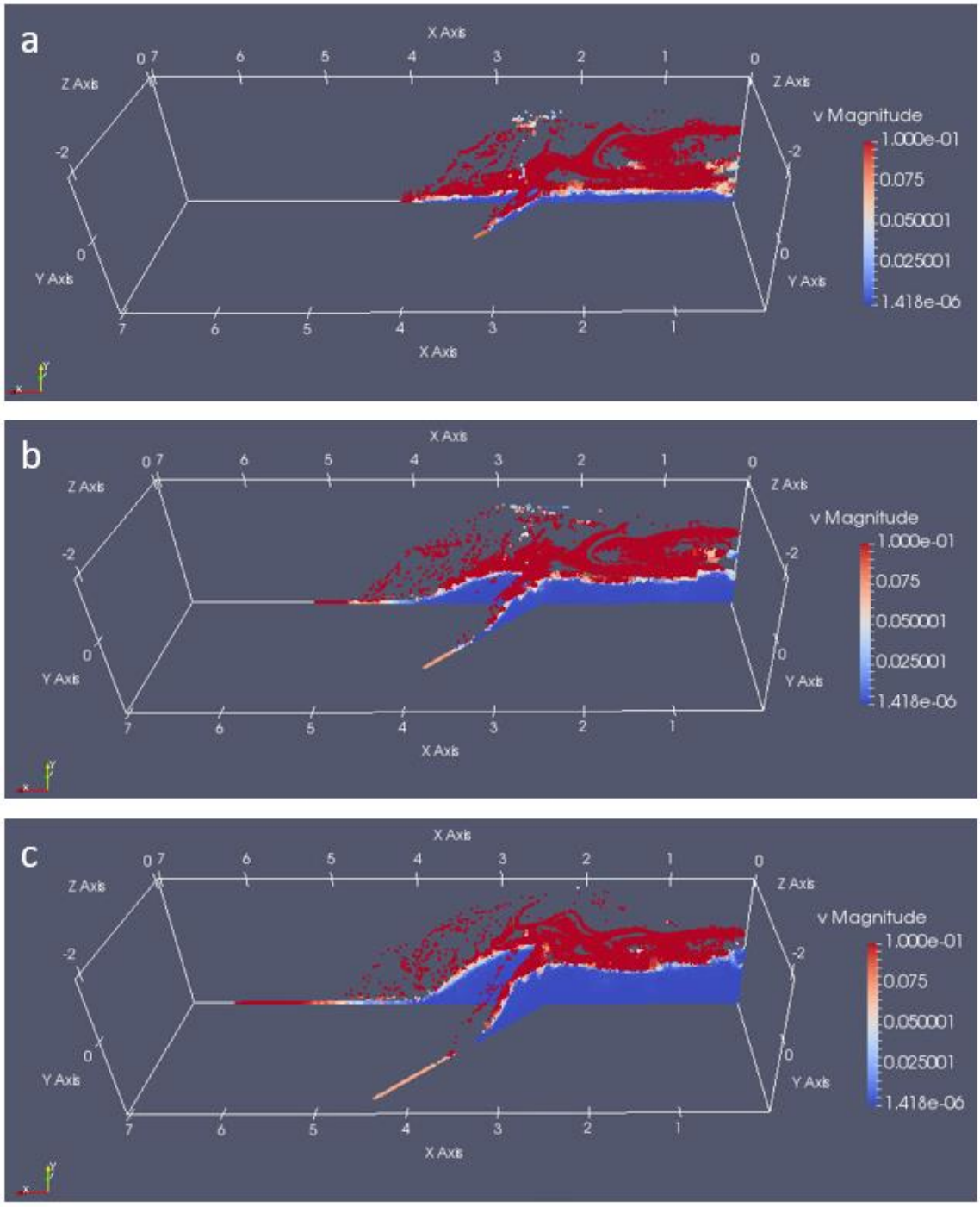

Figure C.4 Visualization of particle distribution for the case of inlet velocity of 3.5m/s at (a) t=100s, (b) t=200s and (c) t=300s

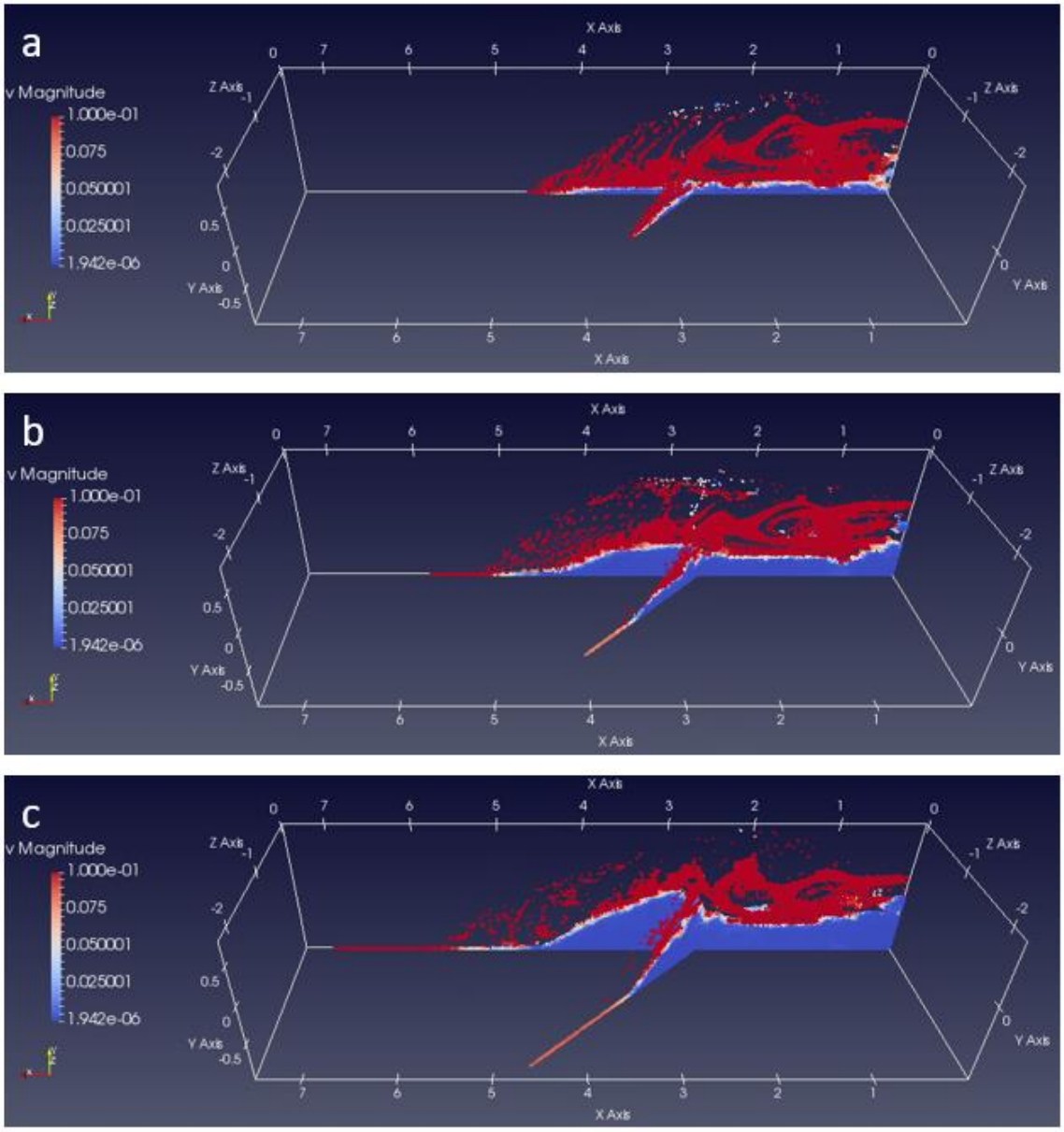

Figure C.5 Visualization of particle distribution for the case of inlet velocity of 4.0m/s at (a) t=100s, (b) t=200s and (c) t=300s

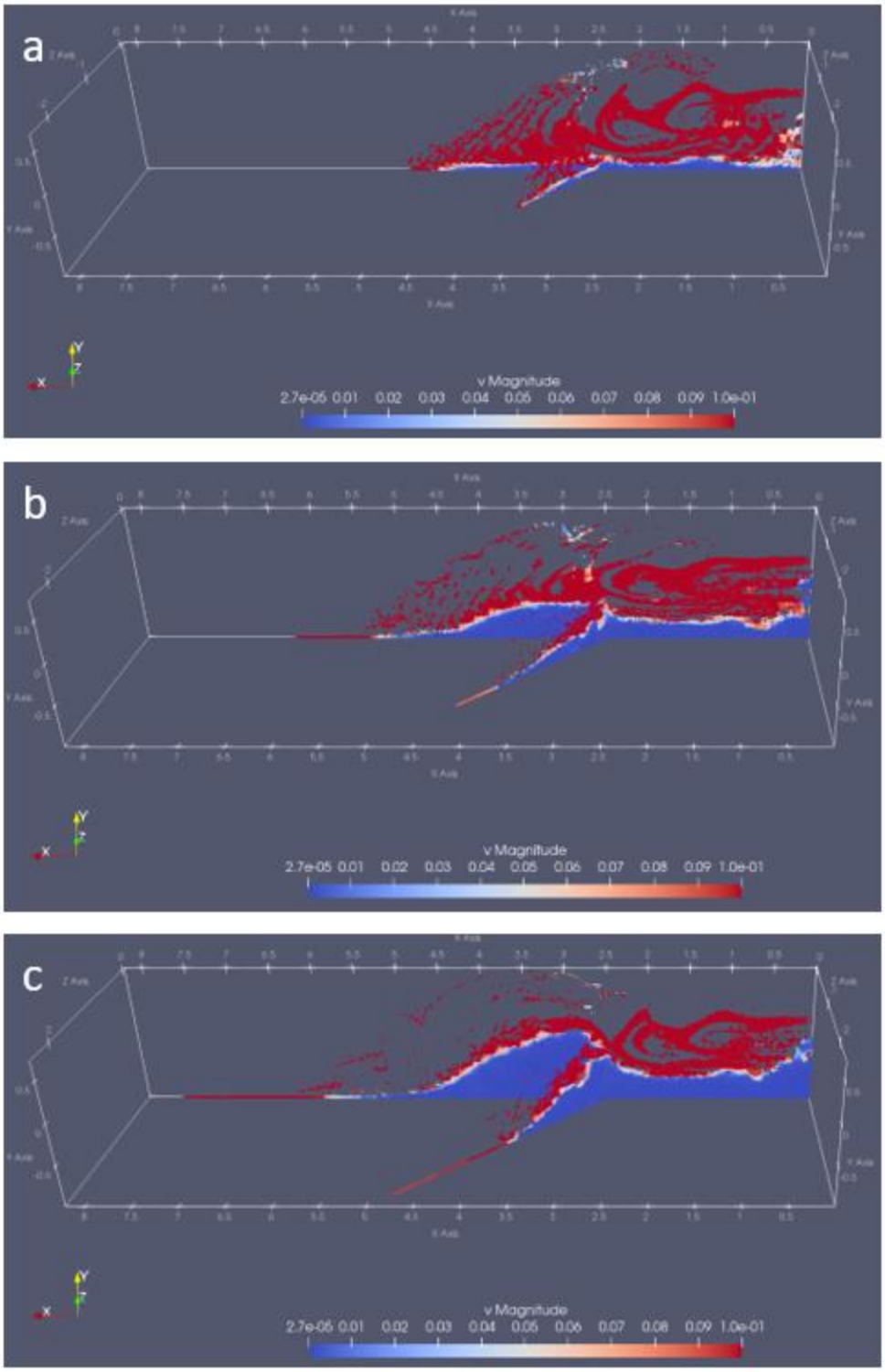

Figure C.6 Visualization of particle distribution for the case of inlet velocity of 4.5m/s at (a) t=100s, (b) t=200s and (c) t=300s

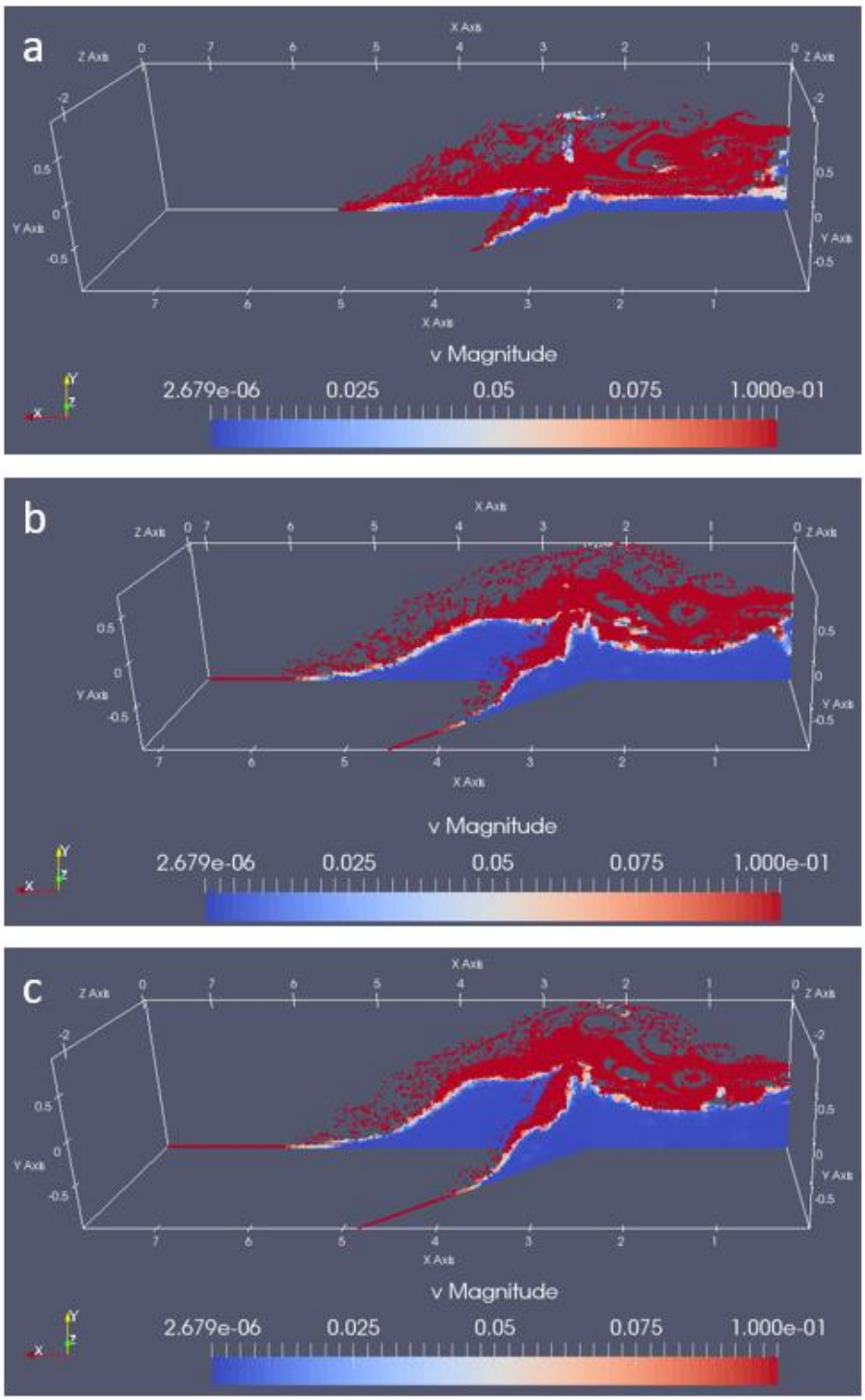

Figure C.7 Visualization of particle distribution for the case of inlet velocity of 5.0m/s at (a) t=100s, (b) t=200s and (c) t=240s

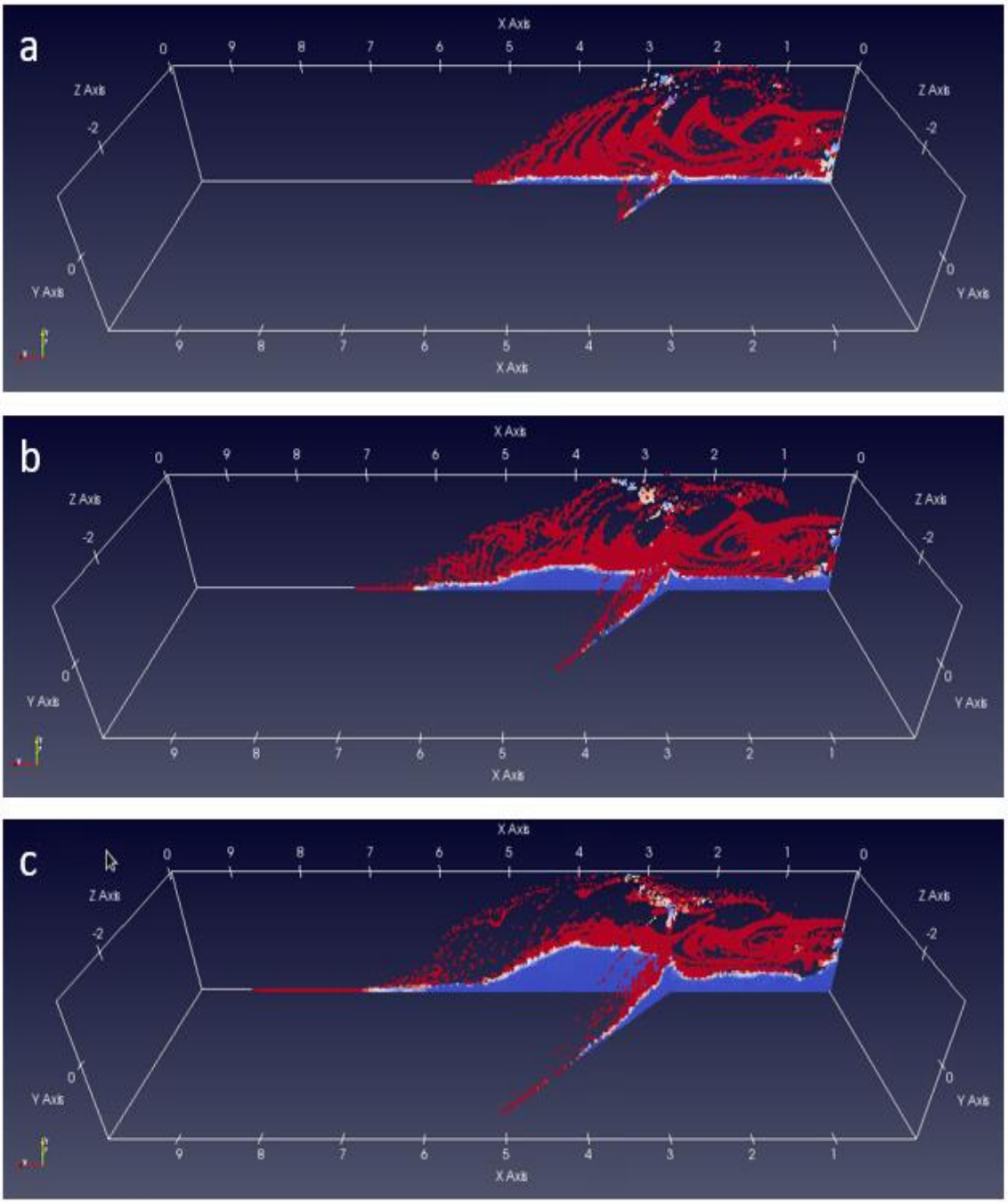

Figure C.8 Visualization of particle distribution for the case of inlet velocity of 5.5m/s at (a) t=100s, (b) t=200s and (c) t=300s

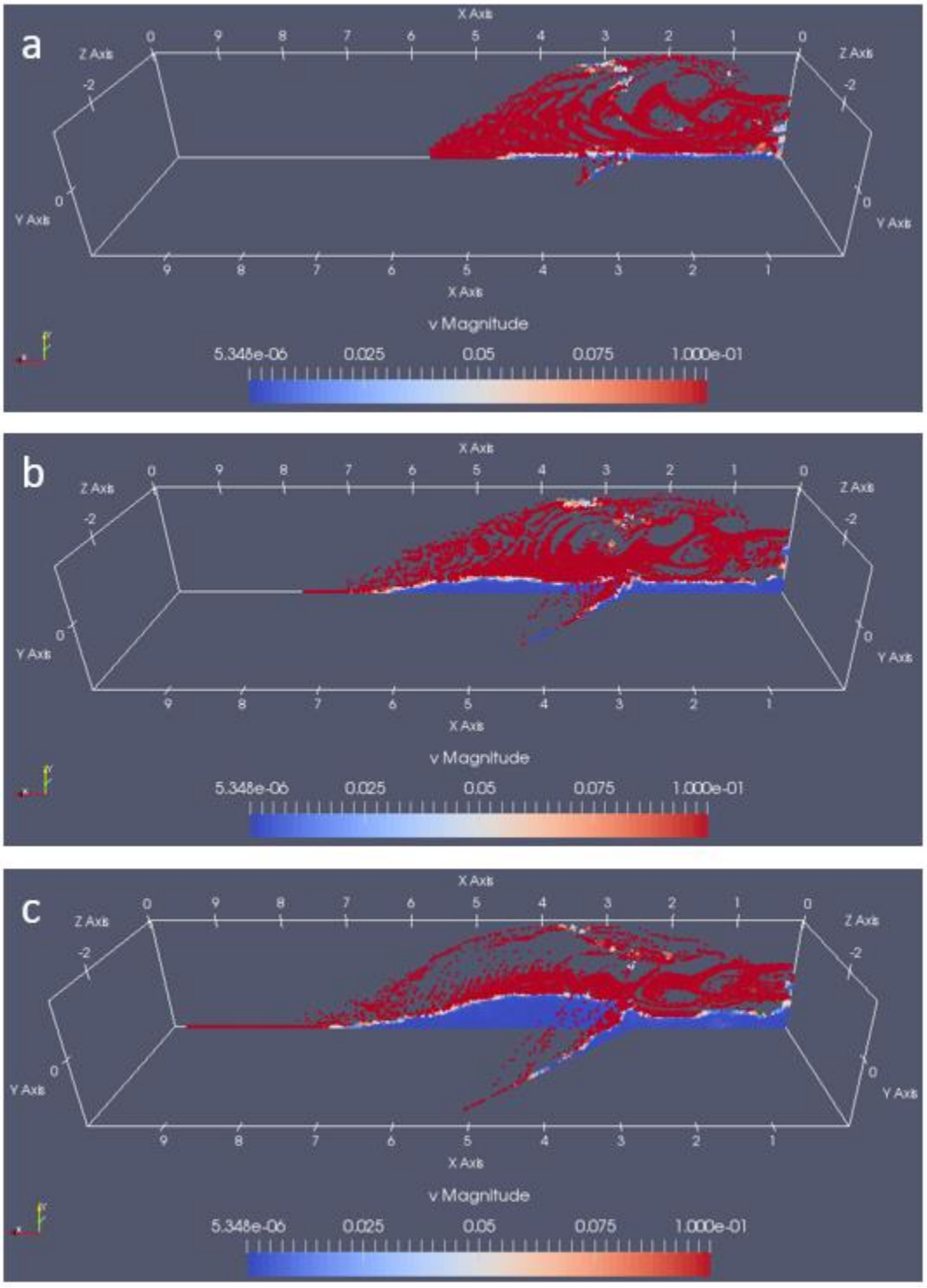
a
X Axis
Z Axis
Y Axis
v Magnitude
5.348e-06
0.025
0.05
0.075
1.000e-01
b
X Axis
Z Axis
Y Axis
v Magnitude
5.348e-06
0.025
0.05
0.075
1.000e-01
c
X Axis
Z Axis
Y Axis
v Magnitude
5.348e-06
0.025
0.05
0.075
1.000e-01

Figure C Error! No text of specified style in document.**.9 Visualization of particle distribution for the case of inlet velocity of 6.0m/s at (a) t=100s, (b) t=200s and (c) t=300s**

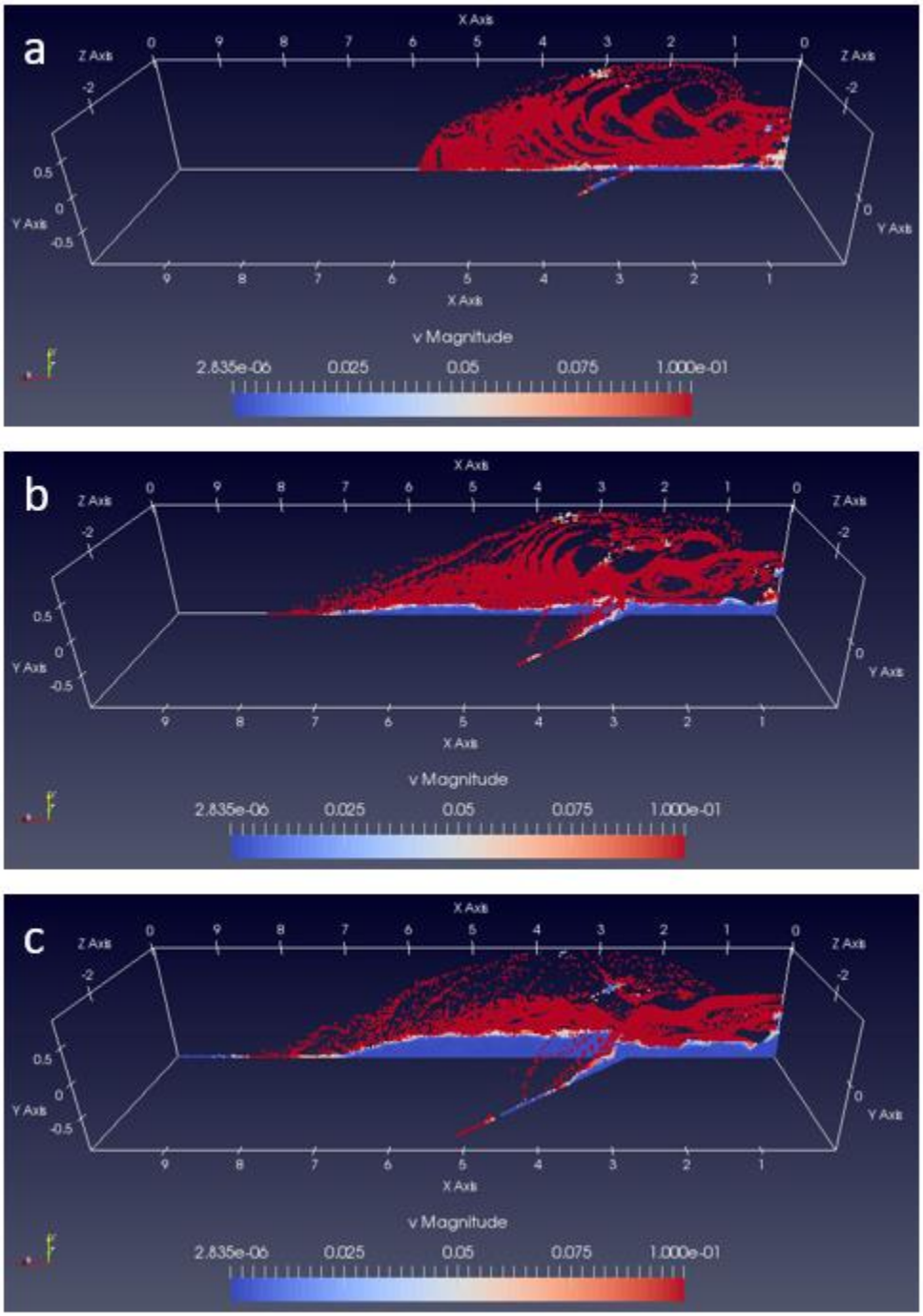

Figure C.10 Visualization of particle distribution for the case of inlet velocity of 6.5m/s at (a) t=100s, (b) t=200s and (c) t=300s

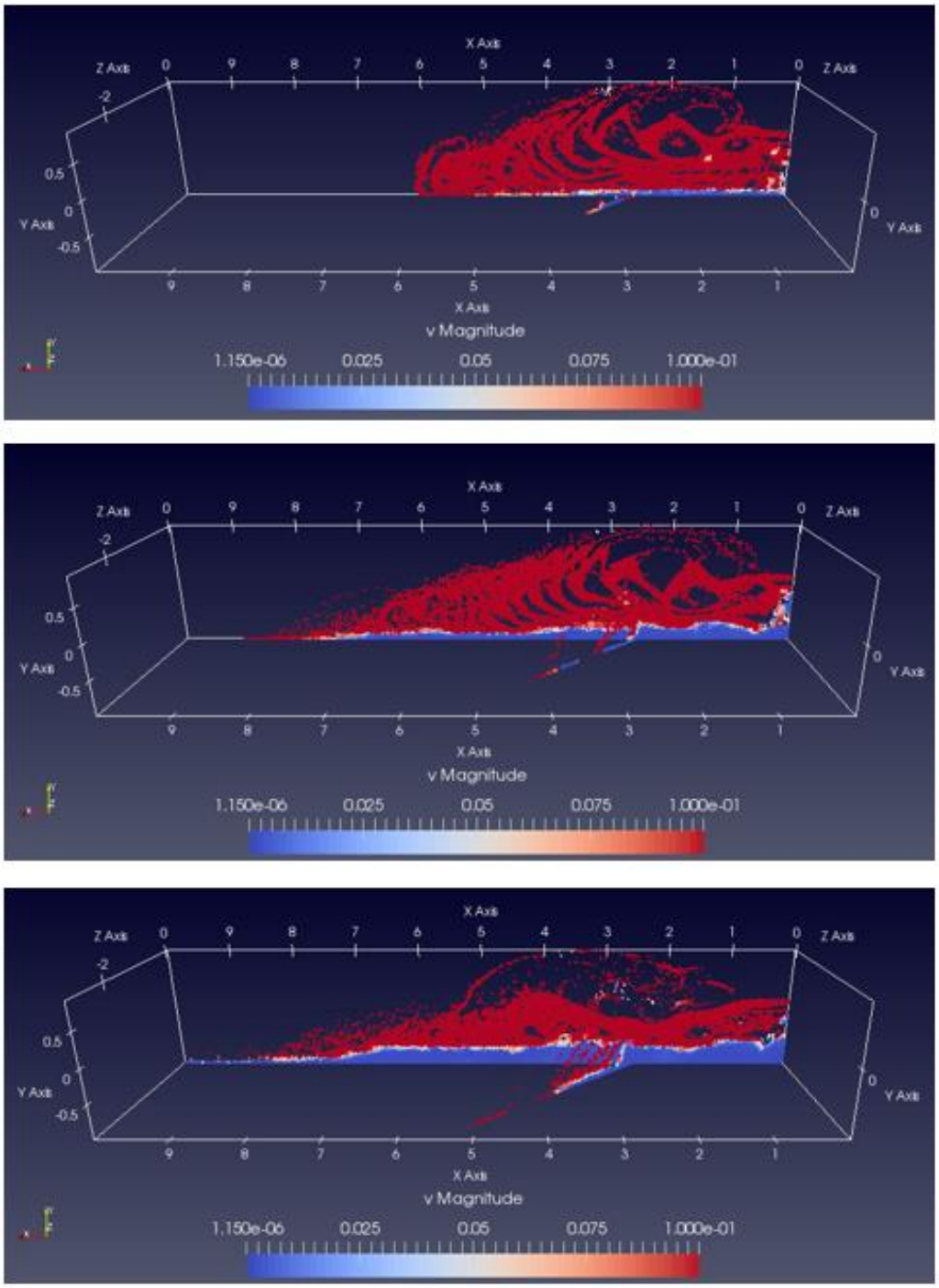

Figure C.11 Visualization of particle distribution for the case of inlet velocity of 7.0m/s at (a) t=100s, (b) t=200s and (c) t=300s

APPENDIX D

PERCENTAGE OF PROPPANT ENTERED NF SUBDOAMIN

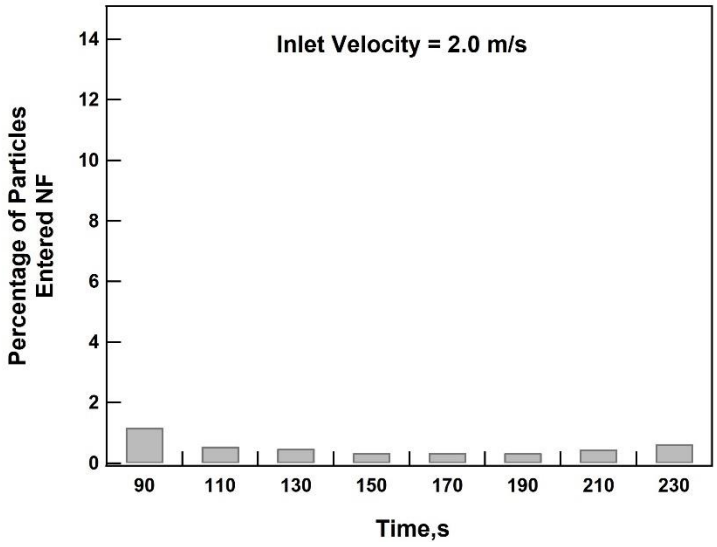

Figure D.1 Percentage of proppant entered NF sub-domain during 20s interval, with inlet velocity = 2.0m/s

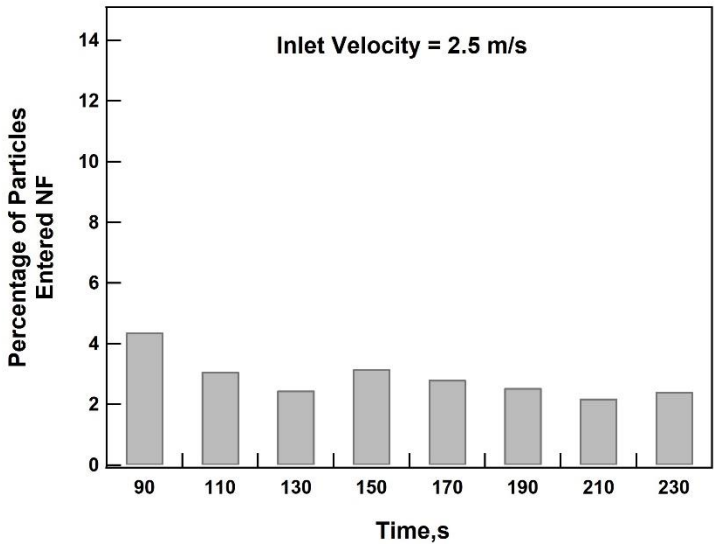

Figure D.2 Percentage of proppant entered NF sub-domain during 20s interval, with inlet velocity = 2.5m/s

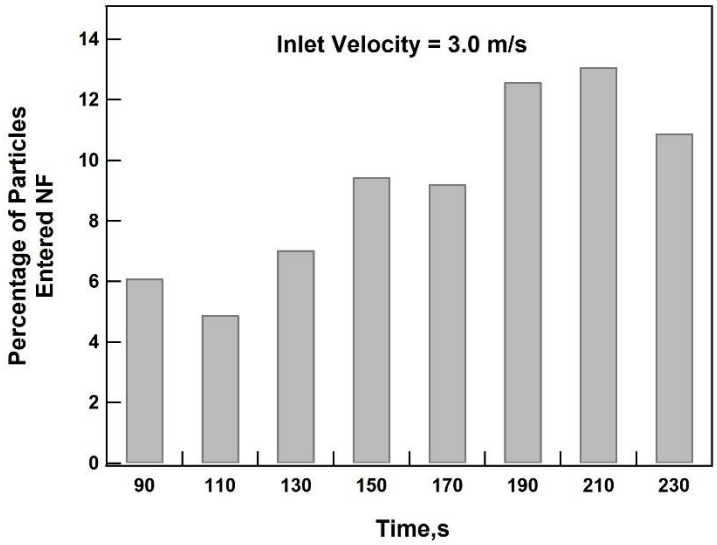

Figure D.3 Percentage of proppant entered NF sub-domain during 20s interval, with inlet velocity = 3.0m/s

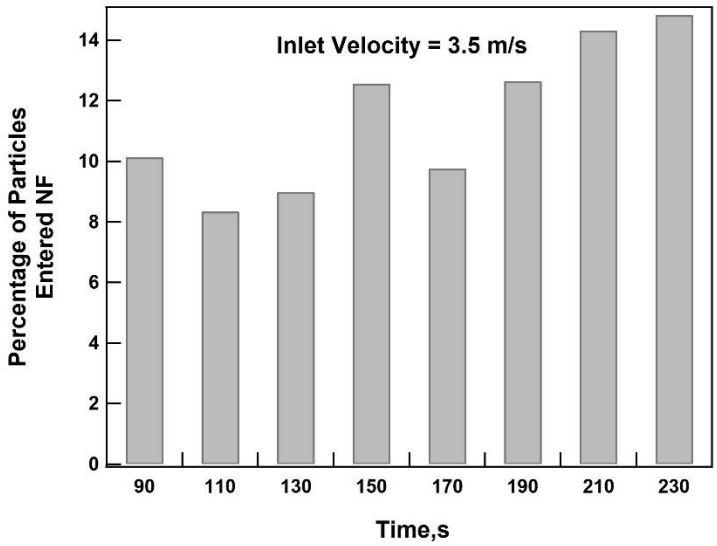

Figure D.4 Percentage of proppant entered NF sub-domain during 20s interval, with inlet velocity = 3.5m/s

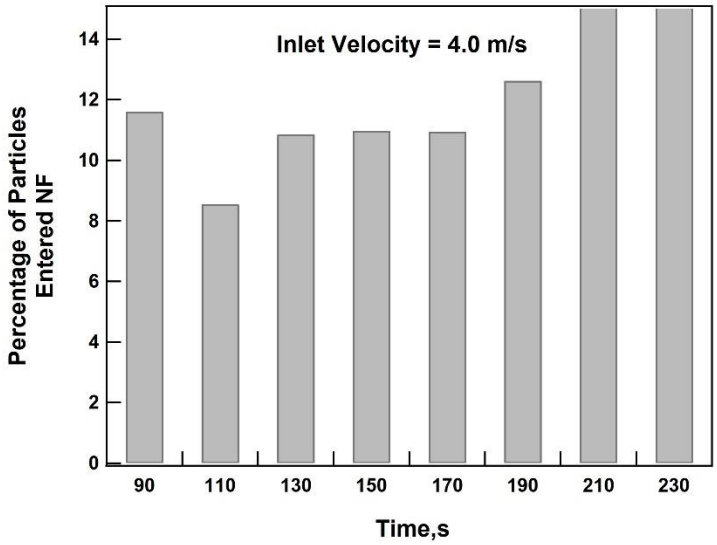

Figure D.5 Percentage of proppant entered NF sub-domain during 20s interval, with inlet velocity = 4.0m/s

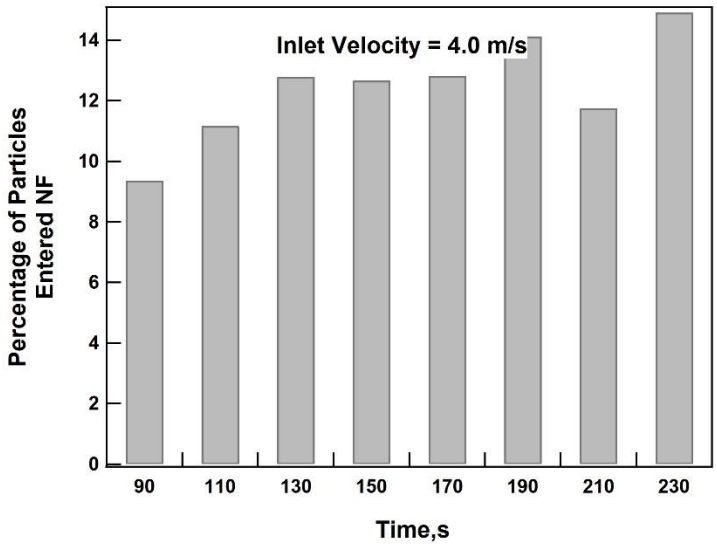

Figure D.6 Percentage of proppant entered NF sub-domain during 20s interval, with inlet velocity = 4.5 m/s

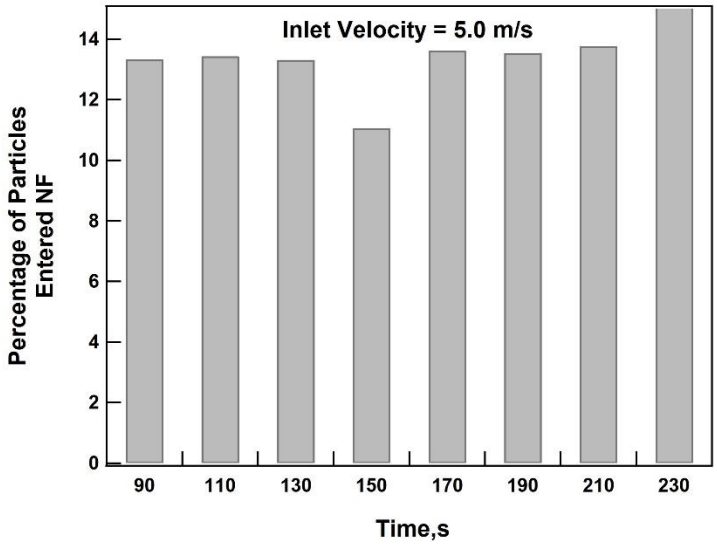

Figure D.7 Percentage of proppant entered NF sub-domain during 20s interval, with inlet velocity = 5.0m/s

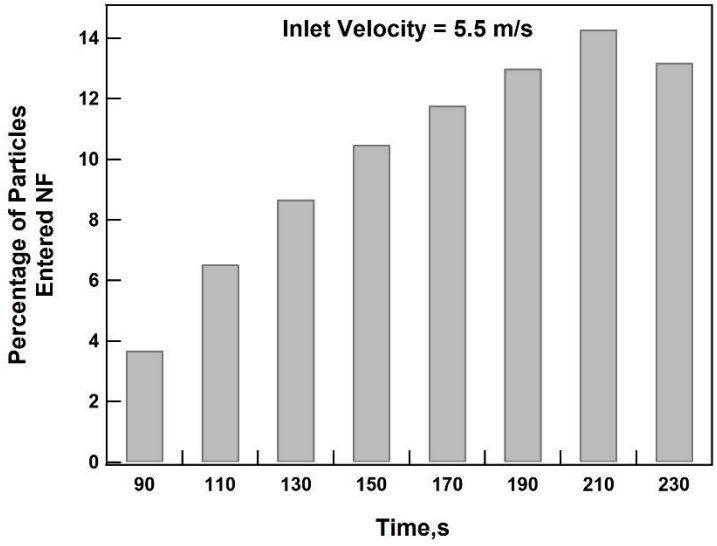

Figure D.8 Percentage of proppant entered NF sub-domain during 20s interval, with inlet velocity = 5.5m/s

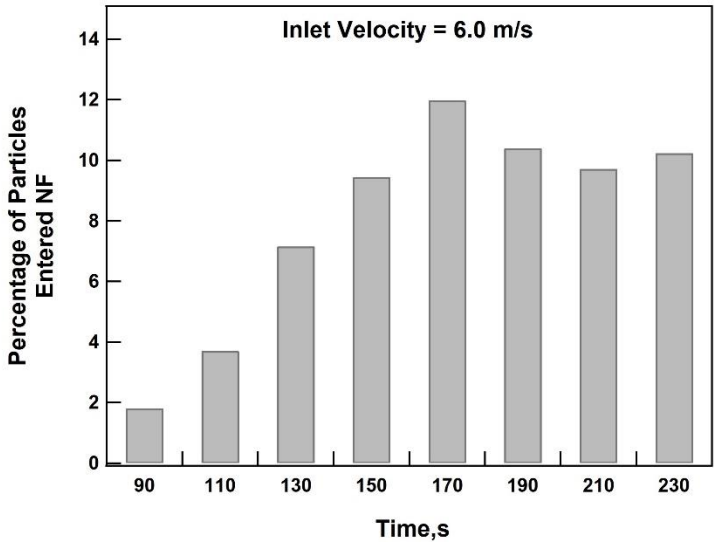

Figure D.9 Percentage of proppant entered NF sub-domain during 20s interval, with inlet velocity = 6.0m/s

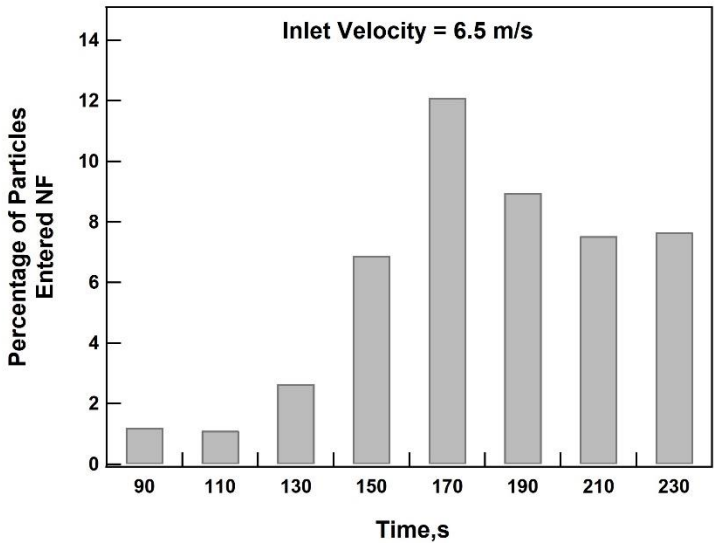

Figure D.10 Percentage of proppant entered NF sub-domain during 20s interval, with inlet velocity = 6.5m/s

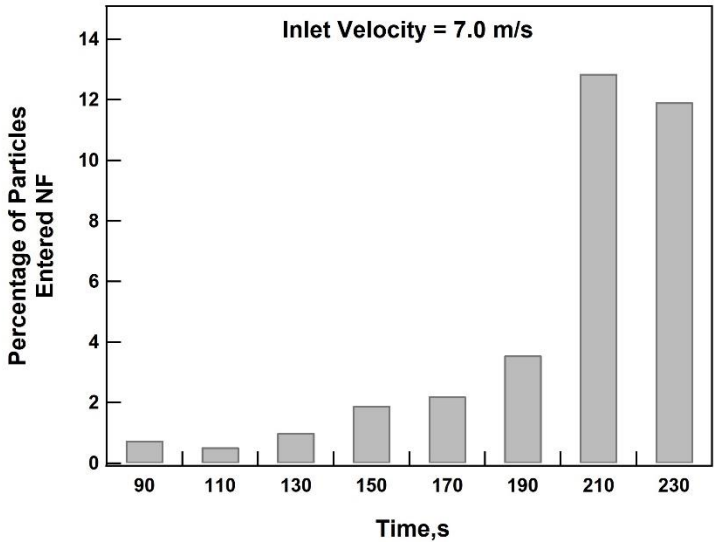

Figure D.11 Percentage of proppant entered NF sub-domain during 20s interval, with inlet velocity = 7.0m/s

APPENDIX E

NUMERICAL EXPERIMENTS OF PROPPANT BRIDGING

Table E.1 Cases when the particles do not block the HF-NF interface

Aperture Radius Ratio, C_p	Proppant Concentration, R_{fp} (PPA)
1.2	0.68
1.41	0.83
1.41	1.36
1.7	1.66
1.7	2.24
2.12	4.15
2.12	5.39
2.4	5.99
2.4	7.46
2.4	9.12
2.83	7.03
2.83	7.86
2.83	9.84

Table E.2 Cases when the particles block the HF-NF interface

Aperture Radius Ratio, C_p	Proppant Concentration, R_{fp} (PPA)
1.2	1.04
1.2	2.07
1.3	3.07
1.3	4.15
1.41	2.49
1.41	7.03
1.7	5.49
1.7	3.32
2.12	8.46